Stony Brook University

First Principles Study of Water: From Fundamental Properties to Photocatalytic Reaction

A Dissertation Presented

by

Jue Wang

to

The Graduate School

in Partial Fulfillment of the Requirements

for the Degree of

Doctor of Philosophy

in

Physics

Stony Brook University

May 2011

Stony Brook University

The Graduate School

Jue Wang

We, the dissertation committee for the above candidate for the Doctor of Philosophy degree, hereby recommend acceptance of this dissertation.

Maria V. Fernandez-Serra – Dissertation Advisor
Assistant Professor, Department of Physics and Astronomy

Philip B. Allen – Chairperson of Defense
Professor, Department of Physics and Astronomy

Thomas C. Weinacht
Associate Professor, Department of Physics and Astronomy

Michael G. White
Professor
Department of Chemistry, Stony Brook University

This dissertation is accepted by the Graduate School.

Lawrence B. Martin
Dean of the Graduate School

Abstract of the Dissertation

First Principles Study of Water: From Fundamental Properties to Photocatalytic Reaction

by

Jue Wang

Doctor of Philosophy

in

Physics

Stony Brook University

2011

Ab initio molecular dynamics (AIMD) simulations of liquid water, based on density functional theory (DFT), yield structural and diffusive properties in reasonable agreement with experiment when artificially high temperatures are used in the simulations for gradient-corrected (GGA) functionals, with NVT ensemble. A series of simulations with GGA functionals are performed and the underestimation of equilibrium density, at ambient conditions, is found. Electronic densities of water molecules with several GGA functionals are examined and used to explain structural and dynamical property differences.

Dispersive non-local electron-electron correlations are studied in this thesis with DFT-AIMD using van der Waals density functional

(vdW-DF) of Dion et al[50]. As expected, the density of water is shown to be grossly underestimated by GGA functionals. When the vdW-DF is used, the density improves drastically and the experimental diffusivity is reproduced without the need of thermal corrections. The origin of the density differences between all the GGA functionals is analyzed. It has been shown that the vdW-DF increases the population of non-H-bonded interstitial sites, at distances between the first and second coordination shells. However, it excessively weakens the H-bond network, collapsing the second coordination shell. This structural problem is partially associated to the choice of GGA exchange in the vdW-DF. It also shows that a different choice for the exchange functional is enough to achieve an overall improvement both in structure and diffusivity.[1]

GaN/ZnO alloy semiconductors have been shown to be promising materials to serve as photo-anode in photocatalytical fuel cells. In recent study by Shen et al[2], the non polar GaN(10$\underline{1}$0) surface has been studied with atomistic modeling and a sequence of intermediate steps for the water oxidation process at the interface are proposed. A thorough AIMD study of the GaN(10$\underline{1}$0) aqueous interface is carried out. This thesis proves that water dissociation happens very fast, within 1.5 ps. OH^- dimers, bound to surface Ga atoms and interacting through hydrogen bonds, are found to account for around 80% of the dissociated water molecules through hydrogen bonds. A detailed study of the OH^- dimers shows their distinguishable structural, dynamical and electronic properties. Solvent water molecules interacting with a dissociating wet surface are also studied in detail, especially the hydrogen bond network. Proton diffusion is found, starting from non-dissociated surface water molecules. Free energy barrier for proton transfer

[1] Jue Wang, G. Roman-Perez, Jose M. Soler, Emilio Artacho, and M. V. Fernandez-Serra *J. Chem. Phys.***134**, 024516 (2011)

[2] X. Shen, Y.A. Small, J. Wang, P.B. Allen, M.V. Fernandez-Serra, M.S. Hybertsen and J.T. Muckerman *J. Phys. Chem. C* **114(32)**, 13695 (2010)

processes at the surface is found to be larger than Grotthuss proton transfer mechanism in liquid water. PKa calculation shows that once water molecules are adsorbed to surface without dissociation, solution near the GaN($10\underline{1}0$) surface becomes acidic.

To my parents and Jingjing

Contents

List of Figures

List of Tables

Acknowledgements

This part is usually the most read one of everyone's thesis. And here I would like to express my greatest gratitudes to everyone who has supported and helped me along the way to complete this thesis. Particularly, I would like to thank the following important people.

My adviser, Prof. Marivi Fernandez-Serra. I am so proud of having the chance to do this interesting research with you and graduating as the first PhD under your supervision. I have so much to thank you in many ways. I can still recall the day I first met you three years ago when you suggested interesting research topics in our first meeting. Along the development of this work, you provided me persistent guidance and numerous care. Without you, this thesis would not come into being. From you, I have learned a lot, from the ways of being a great person to the persistence of hard-working. Of course I should also thank Matt. The gathering family party you and Marivi held in your house gave me great impression and made my time at Stony Brook more joyful. Tag and Sky, you two are the most unique members in our group. I will always remember the special contributions you two made to our group.

Prof. Philip B. Allen. You are both a great theorist and a great educator. Your series of exceptional lectures on various topics in theoretical solid state physics is one of the most precious treasures I have found at Stony Brook. Also, a lot of useful guides and discussions with you also lead me to complete this thesis. I will never forget your kind support and patient help.

Prof. Mark Hybertsen and Prof. James Muckerman. You have organized and participated numerous wonderful seminars and SWaSSiT meetings from which I benefited a lot. During the discussion, you (together with Marivi and Phil) gave me many important suggestions and guidance for my work on water

photocatalytic reaction on GaN surface, which accounts for almost half of my thesis.

My fellow graduate students, Adrien, Betul, Sriram, and so on. It has been such a great fun to discuss with you guys about topics in theoretical condensed matter physics as well as everything else.

My good friends, Li Li, Yuan Sun, Jiayin Sun, Liusuo Wu, Huan Dong, Ning Chen, Wenbin Yan and so on. You made my days at Stony Brook feeling at home. My life becomes more colorful and interesting with you.

My parents, Junshan Wang and Qiaoyu Li. Thank you for teaching me how to overcome obstacles with patience and face challenges with great courage. Without your enduring support, I would not be able to finish this thesis. Let me express my deepest gratitude for what you did for me. Jingjing, you are the most delightful gift I have ever had. I appreciate all the pleasures and supports you give me every day. This thesis is dedicated for my parents and you.

Chapter 1

Introduction

1.1 Motivation

Water is the most abundant compound on the surface of the Earth which is believed to be the most crucial element and constituent of all lives. The oceans are the biggest containers for water which accounts for 1.4×10^{24} grams or 320000000 cubic miles of water. The next big container for water is the rocks of the Earth's crust which hold about 0.8×10^{24} grams. It is well known that without water, there will be no life. Water accounts for almost 65% of human body and over 80% within the brains.

In a special collection of articles published beginning 1 July 2005, Science Magazine and its online companion sites celebrate the journal's 125th anniversary with a look forward – at the most compelling puzzles and questions facing scientists today. A special, free news feature in *Science* explores 125 big questions that face scientific inquiry over the next quarter-century. Among them there is an interesting topic about water: *What is the structure of water?* This topic raises the question about its nearly tetrahedral hydrogen bond structure at room temperature. Also, there are many other properties such as thermal conductivity, optical absorbing, compressibility in many phases which need to be studied in detail.

In another way, water is so important in biology since it is the natural solvent for many metabolic reactions. Chemists, material scientists, geochemists,

environmental and mineral scientists, work together on the study of the effects of interfacial and confined water in different materials, from metals [2, 3], polymers [4] to minerals [5]. In physics, the study of the extremely rich phase diagram of water [6], the understanding of its anomalous properties [6], the characterization of the structure of the different ice phases [7], amorphous ice [7] and supercooled water [6] has engaged scientists for the last fifty years. There exist excellent introductory reviews [7–9], that, starting from a very basic level, summarize the achievements, and open questions that are most relevant to anomalous properties of water.

Water might be the most multidisciplinary research area that can be found within the natural sciences. It is so widely studied that almost every day a new publication related to water will appear. There are large number of both theorists and experimentalists working together on the properties of liquid water. Infra-red, Raman spectra and neutron diffraction experiments are extremely useful to derive structures of ice and water. However, a lot of important properties such as radial distribution function and self-diffusivity of liquid are derived from direct experimental data using theoretical simulations.

Large scale of simulations of liquid water are available since decades ago using many kinds of empirical potential models. However, it is extremely important to have a working description of liquid water from first principles, not for the study of water itself, but for that of systems/environments interacting with water. Scientific fields ranging from biology, biochemistry, geochemistry, to environmental sciences need information about electronic and molecular properties of water interacting with environments. Relying on the empirical potentials would be a tedious and impossible process to deal with a large variety of systems with demands for the accuracy, flexibility and transferability of empirical potentials. All these factors demand a first principles approach to atomic-scale understanding of liquid water.

A first principles description of water is extremely useful to analyze chemical reactions involving solvent because it captures the electronic properties of the system. A recent interesting topic was raised by an experimental group that has found overall water splitting reaction under visible light with semiconductor catalysts.[97] To simulate the system, it requires large cell including

many atoms to represent both semiconductor bulk and surfaces. The lack of periodicity in liquid water poses the main difficulty therefore a gigantic supercell with hundreds of atoms is needed, making the simulations reach nanometer level.

Thanks to the rapid development of technology, the atomistic simulation of many problems related to natural matter systems and water can reach up to nanometer level from first principle with powerful computing clusters such as Bluegene. Although pure liquid water properties can be achieved from first principles simulations using only 32 or 64 water molecules, large supercells are generally required to study these systems due to the size of the molecular clusters or surfaces (metallic or semiconductor). Aside from the improvement of computing power itself, improvements from theoretical level to find a faster but still accurate method are also very important. A numerical atomic orbital(NAO) basis can replace the plane wave basis within the DFT scheme in many systems. The required number of basis elements to achieve convergence is far less than in the plane wave basis for most of the systems studied in this thesis work, which makes it feasible for large scale of simulations of semiconductor surfaces and liquid water interface.

The problem of studying molecules/surfaces in solution is not only computationally expensive, but also a field where ab initio simulations have suffered an important drawback due to the recently discovered problems associated with ab initio molecular dynamics simulations of systems with dispersion interactions. A comprehensive study with pure liquid water with van der Waals dispersion interactions is provided in this thesis. The origin of the crisis and improvements with van der Waals interaction density functionals built into DFT theory will be presented, and new improvements for describing liquid water will be proposed.

Many surfaces have been studied with water as solvent. Semiconductor surfaces are very popular in recent years since they are candidates for photocatalytic water splitting catalysts. GaN has been shown by experiments to be a good catalyst for water oxidation reaction under ultra-violet light. In order to fully understand the solvent environment at the catalyst surface and the full reaction path, a detailed study of GaN/aqueous interface using ab initio

molecular dynamics will be presented. The most interesting discoveries of this very expensive computer simulation are the spontaneous dissociation of water molecules and the proton diffusion process at the surface. The detailed analysis of structural, dynamical and electronic properties of this system will be presented in chapter 5.

1.2 Outline

The outline of the thesis is as follows: (i) In chapter 2 an overview of the DFT method employed in the all the calculations presented in this thesis will be given. Also in this chapter a new theory for describing dispersive van der Waals interaction will be introduced and a new implementation method with a numerical atomic basis will be presented.

(ii) Chapter 3 will be devoted to the study of general DFT water. A work on the study of different pressures and a series of simulations with different GGA functionals, will be presented. The pressure-density phase diagram will be shown for each functional, and a summary of physical properties obtained from AIMD simulations with all GGA density functionals will be shown. It will also raise the question of the needs for van der Waals interactions for a better description of equilibrium density at ambient condition.

(iii) Chapter 4 will be centered on the analysis of ab initio molecular dynamics simulations of liquid water including van der Waals interaction. It will analyze the recently introduced van der Waals(VdW) density functional and will propose a deep discussion on the structure of the HB networks in liquid water. It will show how ab initio molecular dynamics simulations of liquid water have an equilibrium density problem with GGA functional, which can be solved by the vdW functional. More importantly, it will analyze the deep nature of VdW interactions between water molecules and the corresponding significant structural and dynamical changes of the liquid water system.

(iv) The following chapter will present ab initio molecular dynamic simulations of GaN $10\underline{1}0$ non-polar surfaces with liquid water as solvent. This work will show how and when water molecules are dissociated on top of the GaN non-polar surface. It will show a detailed analysis of the structure of disso-

ciated and non-dissociated water molecules on the surfaces. Hydrogen bond networks near the surface are extremely important to study because they are crucial to represent the solvent environment of the catalyst surface. Electronic structures of specific interesting species are also analyzed. A full-path chemical reaction model starting with feasible initial configurations suggested by the results from our AIMD simulation will also be summarized. Last, a proton diffusion process starting from molecularly adsorbed water molecules on the surface will also be shown in this chapter.

(v) Finally, a short chapter of general conclusions and remarks will be included. Future research topics extending the work of this thesis will also be presented here.

Chapter 2

Methodology

This chapter will focus on the theory, methods and implementations of electronic structure theory that are thoroughly used in the whole thesis. Density functional theory(DFT) is often recognized as the cornerstone for studying electronic structure of many systems. It is also often called "a first principles theory" because it solves the approximate Schrödinger-like equations for the electrons and derives all physical properties from the ground state electronic density, with no adjustable parameters. Ab initio molecular dynamics(AIMD) simulation method is another spine of the whole work of this thesis since many systems are studied at room temperature. Physical properties of the system are expressed snapshot by snapshot with the time resolution equal to 0.5 fs.

Although DFT theory is often denoted as "a first principles theory", there are still crucial approximations to be made to achieve quality simulation results. Having a deep understanding of the theory and methods of each individual approximation will not only help improve simulation quality but also help us recognize how much of the obtained result is representative of real "nature" instead of artifacts.

Computational power has been the concern for "electronic structure" theories for decades. Thanks to the rapid development of supercomputers it is now possible to study "matter" at atomic resolution up to nanometer scales. However, efficient implementation of DFT theory is still one of the most difficult and challenging problems and there are many people actively working on

it today. In this thesis, a localized numerical atomic(LNAO) implementation code known as SIESTA program is used throughout. Understanding the theory from the implementation level will also help us to identify the "success" level of the simulation results.

2.1 Density Functional Theory

Condensed matter systems can be seen as an ensemble of interactive nuclei and electrons. Although many systems are studied by empirical potentials between species, obtaining the fitting parameters needed to specify empirical potential models is not only tedious but also somehow artificial. Starting from fundamental equations from quantum mechanics can be a standard procedure and most importantly it provides information about electrons wave functions that much information of the system can be derived from.

The wave function of a system is uniquely determined by a solution of the Schrödinger equation:

$$\hat{H}\left(\boldsymbol{r},\boldsymbol{R}\right)\Phi\left(\boldsymbol{r},\boldsymbol{R}\right)=E\Phi\left(\boldsymbol{r},\boldsymbol{R}\right) \tag{2.1}$$

where $\boldsymbol{r}$ and $\boldsymbol{R}$ represent the positions of the N_e electrons and N_i ions that form the system, and $\hat{H}\left(\boldsymbol{r},\boldsymbol{R}\right)$ is the complete Hamiltonian that can be as :

$$\begin{aligned}\hat{H}\left(\boldsymbol{r},\boldsymbol{R}\right) &= \sum_{\kappa}\frac{\boldsymbol{P}_{\kappa}^{2}}{2M_{\kappa}}+\frac{1}{2}\sum_{\kappa\kappa'}\frac{Z_{\kappa}Z_{\kappa'}}{|\boldsymbol{R}_{\kappa}-\boldsymbol{R}_{\kappa'}|}+\sum_{i}\frac{\boldsymbol{P}_{i}^{2}}{2}\\ &+ \frac{1}{2}\sum_{ij}\frac{1}{|\boldsymbol{r}_{i}-\boldsymbol{r}_{j}|}-\sum_{\kappa i}\frac{Z_{\kappa}}{|\boldsymbol{R}_{\kappa}-\boldsymbol{r}_{i}|}=\\ &= T_{i}\left(\boldsymbol{R}\right)+V_{ii}\left(\boldsymbol{R}\right)+T_{e}\left(\boldsymbol{r}\right)+V_{ee}\left(\boldsymbol{r}\right)+V_{ie}\left(\boldsymbol{r},\boldsymbol{R}\right)\end{aligned} \tag{2.2}$$

where:

- $T_{i}\left(\boldsymbol{R}\right)$ is the ionic kinetic energy operator.
- $V_{ii}\left(\boldsymbol{R}\right)$ is the ion-ion repulsive potential energy operator.

- $T_e(\boldsymbol{r})$ is the electronic kinetic energy operator.
- $V_{ee}(\boldsymbol{r})$ is the electron-electron repulsive potential energy operator
- $V_{ie}(\boldsymbol{r}, \boldsymbol{R})$ is the electron-ion potential energy operator, and the only attractive term in the Hamiltonian.

Greek character indices range over the ionic degrees of freedom and Latin indices over the electronic degrees of freedom. M_k is the mass of the nucleus, and $\boldsymbol{P}_\kappa$ and $\boldsymbol{P}_i$ are the ionic and electronic momentum operators. Throughout this thesis atomic units will be used and therefore $m_{e^-} = |e^-| = 1, \hbar = 1$.

It is almost impossible to exactly solve this equation because of many body effect of electrons. However, the system can be separated into easier problems to solve by using appropriate approximations which are listed as belows:

1. *Born-Oppenheimer approximation*, in order to decouple the ionic and electronic degrees of freedom. Nuclei will be described following the laws of classical physics.
2. *Density functional theory (DFT)*, to calculate the ground state energy and forces of the system. It allows equation 2.1 to be solved for an alternative (fictitious) system of non-interacting particles.
3. *Pseudopotentials*. Only the valence electrons will be considered.
4. *Basis functions*, to expand the electronic wavefunctions in a finite-dimensional, rather than infinite-dimensional Hilbert space.

The Born-Oppenheimer approximation is based on the fact that nucleus masses are much larger than the electron's. This implies that in general electronic velocities are much larger than the ionic ones, and therefore, the dynamical evolution can be decoupled. This approximation is not only useful in a 0K calculation, but also appropriate for a finite temperature molecular dynamics simulation in which the electrons are always considered in their instantaneous ground state.

The total wavefunction is thus separated into the nuclear and electronic parts:

$$\Phi(\boldsymbol{r},\boldsymbol{R}) = \Psi(\boldsymbol{r};\boldsymbol{R})\,\phi(\boldsymbol{R}) \tag{2.3}$$

where the electronic wavefunction $\Psi(\boldsymbol{r};\boldsymbol{R})$ parametrically depends on the ionic position variables.

Substitution of this wave function into equation 2.1 gives:

$$\begin{aligned}
\hat{H}_{e+i}\Psi(\boldsymbol{r};\boldsymbol{R}) &= \left[V_{ii}(\boldsymbol{R}) + T_e(\boldsymbol{r}) + V_{ee}(\boldsymbol{r}) + V_{ie}(\boldsymbol{r},\boldsymbol{R})\right]\Psi(\boldsymbol{r};\boldsymbol{R}) \\
&= E_{e+i}(\boldsymbol{R})\,\Psi(\boldsymbol{r};\boldsymbol{R}) \\
\left[\sum_{\kappa}\frac{\boldsymbol{P}_{\kappa}^2}{2M_{\kappa}} + E_{e+i}(\boldsymbol{R})\right]\phi(\boldsymbol{R}) &= E\phi(\boldsymbol{R})
\end{aligned} \tag{2.4}$$

where E_{e+i} is the Born-Oppenheimer energy of the system and represents the potential seen by the nuclei. They will be treated classically and therefore the second equation in 2.4 will be solved using classical integration of Newton's equations.

Now the total energy of the system can be decomposed as:

$$\begin{aligned}
E &= E_{e+i}(\boldsymbol{R}) + T_i(\boldsymbol{P}) \\
&= E_{elec}(\boldsymbol{R}) + E_{ii}(\boldsymbol{R}) + T_i(\boldsymbol{P}) \\
&= T_e(\boldsymbol{R}) + E_{ee}(\boldsymbol{R}) + E_{ie}(\boldsymbol{R}) + E_{ii}(\boldsymbol{R}) + T_i(\boldsymbol{P})
\end{aligned} \tag{2.5}$$

where T stands for kinetic energy, E for interaction energy.

A classical treatment for heavy nuclei becomes less accurate when mass of the nuclei becomes smaller. In case of a hydrogen atom, which is part of liquid water that is widely studied in this thesis, the nuclear quantum effect becomes crucial. This can be partially solved using path integral method[39], a semi-quantum approximation. Another approach could be adopted by replacing hydrogen atoms with deuterium. In this thesis, the latter method is used, but a source of error needs to be taken into account.

The Born-Oppenheimer approximation decouples nucleus and electrons. Now electrons can be viewed as N interacting electrons, interacting with nuclei

via an external potential $V = v(\mathbf{r})$. The total Hamiltonian for electrons can be expressed as $H = T + U + V$. T and U are the electronic kinetic energy and the electron-electron interaction potential energy and will depend only on the electronic properties; whereas V depends on the atomic species and their positions.

The DFT scheme is based on the ground state electronic density $\rho(\mathbf{r})$ instead of the wavefunction $\Psi(\{\mathbf{r}\})$ is supported by two theorems by Hohenberg and Kohn[10, 11].

Theorem 1 *For any system of interacting particles in an external potential $v(\mathbf{r})$, this potential $v(\mathbf{r})$ is determined uniquely, except for a constant, by the ground state particle density $\rho(\mathbf{r})$.*

As a consequence, many body wave functions for all the states (ground and excited) will be fully determined by the complete Hamiltonian of the system which is determined by $\rho(\mathbf{r})$.

Theorem 2 *A universal functional for the energy $E[\rho(\mathbf{r})]$ in terms of the density $\rho(\mathbf{r})$ can be defined for any external potential $v(\mathbf{r})$. The exact ground state energy of the system is the global minimum of this functional and the density $\rho(\mathbf{r})$ that minimizes the functional is the exact ground state density $\rho_0(\mathbf{r})$.*

The Hohenberg-Kohn theorem suggests that, if we minimize the electronic energy functional as a function of electronic density with the constraint that total particle number equals N, both ground state energy and ground state electronic density can be found at the same time.

$$\delta\left\{E^{ele}[\rho] - \mu\left[\int \rho(\mathbf{r})\, d\mathbf{r} - N_e\right]\right\} = 0 \tag{2.6}$$

$$\left.\frac{\delta E^{ele}[\rho]}{\delta \rho(\mathbf{r})}\right|_{\rho=\rho_0} = \mu \tag{2.7}$$

The Lagrange multiplier, μ, is the chemical potential of the system.

Kohn and Sham[51] developed a scheme for condensed matter system using the previous theorem. Instead of the many body interacting electron system, they suggested that a different *auxiliary system* can be used to solve the minimization of the total energy. The crucial part is to replace many body terms with exchange-correlation interactions as a functional of the electronic density with appropriate approximation. Thus the ground state density of the original many body interacting system is assumed to be the same as an independent N electrons system. This gives the well known Kohn-Sham equations:

$$\begin{aligned}\left\{-\frac{1}{2}\nabla^2 + v_{ext}(\mathbf{r}) + \int \frac{\rho(\mathbf{r}')}{|\mathbf{r}-\mathbf{r}'|}d\mathbf{r}' + \frac{\delta E_{xc}[\rho]}{\delta\rho(\mathbf{r})}\right\}\psi_i &= \\ \{-\frac{1}{2}\nabla^2 + \underbrace{v_{ext}(\mathbf{r}) + v_H(\mathbf{r}) + v_{xc}([\rho];\mathbf{r})}_{v_{eff}(\mathbf{r})}\}\psi_i &= \varepsilon_i\psi_i \end{aligned} \tag{2.8}$$

where δ is the functional derivative of E_{xc}[1] and the density of the system is:

$$\rho(\mathbf{r}) = \sum_{i=1}^{N} |\psi_i(\mathbf{r})|^2. \tag{2.9}$$

These equations correspond to the Schrödinger equation of a particle that "sees" an effective potential result of the external potential, the Hartree electronic interaction and the exchange and correlation potential:

$$v_{eff}(\mathbf{r}) = v_{ext}(\mathbf{r}) + v_H(\mathbf{r}) + v_{xc}(\mathbf{r}) \tag{2.10}$$

The procedure to obtain the final total energy of the system is completely self consistent. The solution of equation (2.8) produces the wave functions ψ_i to obtain the electronic density from equation (2.9), which is used to define the effective potential in equation (2.8). This process is repeated until the

[1]Defined as

$$\frac{\delta F[\rho]}{\delta\rho(\mathbf{r})} = \lim_{\varepsilon\to 0^+}\{F[\rho(\mathbf{r}\,') + \varepsilon\delta(\mathbf{r}-\mathbf{r}\,')] - F[\rho(\mathbf{r}\,')]\}/\varepsilon$$

tolerance imposed on the difference between the input and output density is reached.

The Kohn-Sham scheme replaces many-body problems with independent-electron equations. However, the explicit formula of the exchange and correlation functional $E_{xc}[\rho]$ as a function of electronic density is not known.

A widely used approximation for solid state system is called local density approximation (LDA), in which

$$E_{xc}^{LDA} = \int \rho(\mathbf{r}) \varepsilon_{xc}^{LDA} \left[\rho(\mathbf{r})\right] d\mathbf{r} \tag{2.11}$$

where $\varepsilon_{xc}^{LDA}(\rho)$ is the exchange-correlation energy of an homogeneous electron gas with density ρ.

This approximation is appropriate for smooth $\rho(\mathbf{r})$, i.e, for solids close to the homogeneous electron gas. However, for inhomogeneous systems such as molecules, clusters or layers, LDA is not accurate. Instead, a generalized-gradient approximation GGA is often used.

The generic formulation of the GGA approximation to $E_{xc}[\rho]$ is:

$$E_{xc}^{GGA} = \int \rho(\mathbf{r}) \varepsilon_{xc}^{GGA} \left[\rho\left[\mathbf{r}\right], |\nabla \rho(\mathbf{r})|\right] d\mathbf{r} \tag{2.12}$$

The exchange-correlation energy not only depends on the local density but also on gradients of the density, allowing to take into account the variations of the electronic density in very inhomogeneous systems.

The general procedure for constructing GGA functionals is to express the correlation energy as:

$$E_{xc}^{GGA} = \int \rho(\mathbf{r}) \varepsilon_{xc} \left[\rho(\mathbf{r})\right] d\mathbf{r} + \int F_{xc} \left[\rho(\mathbf{r}), |\nabla \rho(\mathbf{r})|\right] d\mathbf{r} \tag{2.13}$$

where the function F_{xc} called exchange and correlation enhancement factor is often selected to satisfy a series of formal conditions related to the exchange and correlation hole.

In this thesis, four GGA functionals are chosen to study liquid water: BLYP[46, 47], PBE[48], RPBE[53] and revPBE[54].

- BLYP is a functional from the quantum chemistry community. The exchange part of this functional is from Becke[46]. It has been fitted to reproduce the exact exchange for a number of elements of the periodic table. The correlation energy is from the work of Lee-Yang-Parr[47]. This functional is very successful for molecular systems.

- PBE by Perdew-Burke-Ernzerhof[48] is a functional produced by the physics community, and generated without fitting to any database of molecules. The exchange is not only dependent on the local density but also the gradient of the density in a way that Lieb-Oxford bound is satisfied.

- RPBE[53] is a simple modification of PBE that proposes a different functional form for F_x.

- revPBE[54] is a modified version of PBE that satisfies integrated Lieb-Oxford bound instead of local Lieb-Oxford bound proposed in [48].

In chapter 3, I will show some results and conclusions about the performance of the different GGA functionals on the description of liquid water.

A van der Waals density functional is also studied in detail in chapter 4. Dion et al.[50] have proposed a way of including dispersive non local interactions for sparse systems such as soft matter, large molecular clusters. They developed a van der Waals density functional (vdW-DF) for general geometries, in which the exchange and correlation energy can be expressed as:

$$E_{xc}^{VdW}(n) = E_x^{GGA}(n) + E_c^{LDA}(n) + E_c^{nl}(n) \tag{2.14}$$

where

$$E_c^{nl}(n) = \frac{1}{2}\int d^3r d^3r' n(\overrightarrow{r})\phi(\overrightarrow{r},\overrightarrow{r}')n(\overrightarrow{r}') \tag{2.15}$$

$\phi(\overrightarrow{r},\overrightarrow{r}')$ is a given kernel depending on $\overrightarrow{r} - \overrightarrow{r}'$ and density n in the vicinity of $\overrightarrow{r}$ and $\overrightarrow{r}'$.

2.2 The SIESTA method

The DFT code employed throughout this thesis is the implementation of SIESTA, an LCAO method based on the use of numerical atomic orbitals of finite support to expand the electron wavefunctions. The orbitals are similar to wavefunctions of hydrogen-like atoms. They are composed as the product of a spherical harmonic times a radial function. They are localized, i. e. defined to be zero beyond a specified radius.

2.2.1 Solution of the KS equations: Basis Set Expansion

The KS equations must be solved by expanding the wavefunction in terms of finite number of basis functions in Hilbert space: $\psi_i(\mathbf{r}) = \sum_\mu \phi_\mu(\mathbf{r}) c_{\mu i}$.

There are two commonly used expansion basis set: plane waves and localized orbitals.

Plane waves are a simple and natural representation of wave functions. They are the eigenstates of the Schrödinger equation with constant potential and thus should be natural basis for the description of bands in nearly free electron approximation. The Bloch theorem can be employed to solve the Schrödinger equation with periodic boundary potentials in the crystal structure.

Localized orbital methods (linear combination of atomic orbitals), on the other hand, are commonly used in the tight binding approximation that can be employed in solids and molecules. In this thesis, numerical atomic orbitals are used as the expansion basis to solve the KS equations.

They are generated by solving, for each angular momentum, the radial Schrödinger equation for the corresponding nonlocal pseudopotential within a hard confining potential. The confinement is to ensure "locality" of the orbitals. In the SIESTA method, a soft confining potential that rapidly diverges at r_c is used to generate localized orbitals that are continuous at r_c in terms of both wavefunctions and the first order derivatives of wavefunctions. [13]

$$V(r) = V_o \frac{e^{-\frac{r_c - r_i}{r - r_i}}}{r_c - r} \tag{2.16}$$

where r_i is the radius where the potential starts, it diverges at r_c and V_o is a prefactor.

Double-ζ basis sets in SIESTA are generated by splitting the calculated NAOs into two parts, a short range smooth part and the remaining part, that are treated as independent basis orbitals. This procedure can be repeated to generate multiple-ζ bases for each valence orbital.

Optimal atomic basis orbitals have been optimized variationally to minimize the total energy within an environment similar to where they will be used. For example, small water systems with 32 water molecules are studied to generate an optimal atomic basis for the study of a much larger system. The optimized parameters, that control the quality of the basis set for a fixed number of orbitals (size of the basis) are given by the equation of the confining potential 2.16.

2.2.2 Pseudopotentials

Core electrons are in general strongly bound to the nuclei and chemically inert. In the pseudopotential approximation, the core electrons density is assumed to be of the same form as for isolated atoms. Core electrons screen the nuclear potentials seen by the valence electrons. At the same time, core electrons are much lower in energy than valence electrons. Thus due to the requirement of orthogonal wave functions, valence electrons wave functions have a strong oscillatory part in the internal regions. This requires many more basis functions to accurately describe the valence electrons wave functions.

Pseudopotentials are fictitious potentials that act in the internal regions of the atom, reproducing the screening effect of the core electrons within core region which is determined by cutoff radius. Both the potentials and wave functions outside of the core region are fitted to reproduce the real ones. The quality of a pseudopotential is measured by its transferability, i.e, the capacity of accurately reproducing results for all-electron calculations.

In this thesis, norm conserving pseudopotentials[16] will be used, in their completely non local representation[15]. They are built from a smooth and local part. The long range part is identical for all the angular momentum

channels and the non-local part is described by Kleinman-Bylander projectors:

$$\hat{V}_{PS} = \int d^3\mathbf{r}\ |\mathbf{r}\rangle V_{local}(r)\langle\mathbf{r}| + \sum_{l,m}^{l_{\max}^{PS}} |\chi_{lm}\rangle V_l \langle\chi_{lm}|, \tag{2.17}$$

where $V_{local}(r)$ decays as $-Z_{val}/r$ when $r \to \infty$.

2.2.3 Hamiltonian and Overlap Matrices

In the pseudopotential approximation, the KS Hamiltonian defined in 2.8 can be expressed as:

$$\left[T + \sum_{at} \left(V_{at}^{local}\left(\mathrm{r}\right) + V_{at}^{nl}\left(\mathrm{r}\right)\right) + V_H\left(\mathrm{r}\right) + V_{xc}\left(\mathrm{r};\rho\right)\right] \tag{2.18}$$

where V_H is the Hartree potential generated by $\rho\left(\mathrm{r}\right)$ and T is the kinetic energy operator.

The Hamiltonian is separated in such a way that some terms are expressed in real space grids and others in the Fourier space.

Overlap matrix elements such as $S_{\mu\nu} = \langle\phi_\mu|\phi_\nu\rangle$, the integrals $\langle\chi_{lm}|\phi_\mu\rangle$ involved in the second term of Eq. (2.17), and the kinetic matrix elements $T_{\mu\nu} = \langle\phi_\mu| - \frac{1}{2}\nabla^2|\phi_\nu\rangle$ are calculated in Fourier space, using convolution techniques, and stored as a product of spherical harmonics times numerical radial functions, interpolated in a fine radial grid ([14]).

To compute the matrix elements of the local potentials, the electron density $\rho(\mathbf{r})$ is calculated, in a regular three-dimensional grid of points $\mathbf{r}$, from the density matrix:

$$\rho(\mathbf{r}) = \sum_{\mu\nu} \phi_\mu(\mathbf{r})\rho_{\mu\nu}\phi_\nu(\mathbf{r}). \tag{2.19}$$

From $\rho(\mathbf{r})$ the Hartree potential $V_H(\mathbf{r})$ (the electrostatic potential created by $\rho(\mathbf{r})$) is calculated using fast Fourier transforms (FFT). The exchange and correlation potential $V_{xc}(\mathbf{r})$ is computed in the local density (LDA) or generalized gradient (GGA) approximations, the latter using finite difference derivatives.

The total effective potential $V_{eff}(\mathbf{r})$ is calculated by adding the local pseudopotentials of all the atoms to $V_H(\mathbf{r}) + V_{xc}(\mathbf{r})$. Since both V_{local} and V_H have long range parts with opposite signs, the electrostatic potential created by a reference density (the sum of the electron densities of the free atoms) is subtracted from each of them. Finally the matrix elements $\langle\phi_\mu|V_{eff}|\phi_\nu\rangle$ are calculated by direct integration over the grid points.

The evaluation of the total energy, atomic forces, and stress tensor, proceeds simultaneously to that of the Hamiltonian matrix elements, using the last density matrix available during the self consistency process.

2.2.4 Van der Waals Implementation

Dion et al. introduce dispersive non local van der Waals interaction as a density n followed by: [50]

$$E_c^{nl}(n) = \frac{1}{2}\int d^3r d^3r' n(\mathbf{r})\mathbf{n}'(\mathbf{r}'))\phi(\mathbf{q_1}, \mathbf{q_2}, \mathbf{r_{12}}) \tag{2.20}$$

van der Waals interactions are most familiar as a r^{-6} relation, attraction between distant localized objects, in addition to whatever classical electrostatic interactions are implied by their static charge distributions. From the DFT point of view, as shown in 2.15, the non local correlation is determined by kernel $\phi(q_1, q_2, r_{12})$, which is only dependent on $r_{12} = |\mathbf{r_1} - \mathbf{r_2}|$ and q_1, q_2 are values of universal functions $q_0(n(\mathbf{r}), |\nabla\mathbf{n}(\mathbf{r})|)$ evaluated at $\mathbf{r_1}$ and $\mathbf{r_2}$.

The shape of ϕ obeys that: (i) E^{nl} is strictly zero for any system with constant density; and (ii) the interaction between any two molecules has the correct r^{-6} dependence for large separations r. However, the double spatial integrals are computationally too expensive for the very large scale simulations required in soft-matter and biomolecular problems. Thus G. Roman-Perez et al. proposed an efficient implementation method. [55]

The key step for the implementation is to expand the kernel ϕ as:

$$\phi(q_1, q_2, r_{12}) = \sum_{\alpha\beta}\phi(q_\alpha, q_\beta, r_{12})P_\alpha(q_1)P_\beta(q_2) \tag{2.21}$$

where q_α are fixed values, chosen to ensure a good interpolation of ϕ.

The functions $P_\alpha(x)$ are chosen to be a succession of cubic polynomials in the interval $[x_\alpha, x_{\alpha+1}]$. Notice that $P_\alpha(x)$ is dependent on which interpolation scheme is chosen and what the value is for x_α. As an example, two dimensional interpolation can be done in the form:

$$f(x,y) = \sum_\beta f(x,y_\beta)P_\beta(y) = \sum_\beta \left(\sum_\alpha f(x_\alpha, y_\beta)P_\alpha(x) \right) P_\beta(y) \tag{2.22}$$

Substituting 2.22 into 2.20:

$$E_c^{nl} = \frac{1}{2}\sum_{\alpha\beta} \int\int d^3\mathbf{r_1} \mathbf{d^3 r_2} \theta_\alpha(\mathbf{r_1})\theta_\beta(\mathbf{r_2})\phi_{\alpha\beta}(\mathbf{r_{12}}) = \mathbf{\frac{1}{2}} \sum_{\alpha\beta} \int \mathbf{d^3 k} \theta^*_\alpha(\mathbf{k})\theta_\beta(\mathbf{k})\phi_{\alpha\beta}(\mathbf{k}) \tag{2.23}$$

where $\theta_\alpha(\mathbf{r}) = \mathbf{n(r)P}_\alpha\left[\mathbf{q_0}(\mathbf{n(r)}, \nabla\mathbf{n(r)})\right]$ and $\theta_\alpha(\mathbf{k})$ is the Fourier transform. $\phi_{\alpha\beta}(k)$ is the Fourier transform of $\phi_{\alpha\beta}(r)$

Thus the double integral has been reduced to only one integral and the heavy part is the Fourier transform which can be done with the fast Fourier Transform Algorithm.

Chapter 3

Ab Initio Simulations of Liquid Water

The purpose of this work is to assess the situation regarding the equilibrium description of DFT water. Motivated by the low diffusivity and low density at ambient conditions recently found in ab initio simulations of liquid water with several GGA density functionals, its structural and dynamical properties, dependence on temperature, system size, and density functionals are studied. Ab initio molecular dynamics (AIMD), following the Born-Oppenheimer forces obtained from density-functional theory (DFT) as described in chapter 2, is the method employed throughout this study. Due to the large number of simulations with different densities and different GGA functionals studied in this chapter, we use 64 water molecules in all of the AIMD water simulations. The system size effect and corresponding converging errors are also studied and estimated. The structure of liquid water from AIMD simulations shows large dependence on the choice of exchange and correlation functionals. This is because different GGAs describe water molecules in various ways; for example PBE[48] results in more ionic characteristics than revPBE[54], which on the other hand is more covalent.

3.1 Introduction

Many people over the past sixteen years have studied liquid water with density functional theory (DFT)-based *ab initio* molecular dynamics (AIMD) simulations[25–31]. All studies show serious differences from experimental results both in diffusive and structural properties. This is true even though most studies have been performed at the experimental density, which implies theoretical pressures as high as 1 GPa.[32] The origin of the discrepancy with experiments[33–35] is still unclear. One of the main conclusions of these studies[28] was that the AIMD results for radial distribution functions (RDF) and self-diffusivity at a given temperature compare well with the experimental results at a temperature 10% to 20% lower. Therefore, a practical solution to the problem is to perform simulations at temperatures 20% higher than the desired reference temperature,[36] as proposed in Ref[28]. However, although this *ad hoc* solutions may be convenient to study other properties of liquid water,[37] of molecules in solution,[36] and of wet interfaces,[38] they do not help explain the origin of the differences between experiments and AIMD simulations.

Even if a wide range of empirical potentials exist for pure liquid water that offer a better description than that attainable nowadays by DFT, it is extremely important to have a working description of liquid water at the DFT level, not for the study of water itself, but for that of systems interacting with water. This is important in scientific fields as wide as wet chemistry, biochemistry, geochemistry and environmental sciences. Empirical potentials do not have enough flexibility and transferability to describe the large variety of processes happening in wet systems.

Computational studies of liquid water differ widely in their methodology: e.g. they might employ either Born-Oppenheimer or Car-Parrinello[42] dynamics, they can use different types of basis sets,[25, 28, 30, 43] and nuclear quantum effects may or may not be accounted for. Nonetheless, most are performed at a fixed volume, set approximately to the experimental density of water at room temperature, $\simeq$1.0 g/cm^3. This approach would be correct if the calculated pressure also reproduced the experimental pressure at ambient

conditions (1 atm). However, as pointed out in Refs.[28, 44], even though pressure fluctuations are very large due to the small size of the simulated system, the observed average pressure is much larger than the experimental one. Therefore, both structural and diffusive features correspond to a region of the temperature-pressure phase diagram which differs form the experimental values they are compared to.[44] In Ref.[44], the discrepancy between theory and experiment of the pressure-density phase diagram was addressed using Monte Carlo simulations. In a word, the simulations are performed at too high temperatures and pressures.

There are some obvious limitations in the AIMD description of liquid water that could account for these differences, including the inability of present generalized-gradient approximation (GGA) density functionals to describe dispersion (van der Waals) interactions, or the complete neglect of quantum fluctuations in the classical treatment of nuclear dynamics.

The former question will be answered in my thesis in the next chapter: the van der Waals Effect on Liquid Water. The latter question has already been addressed: Morrone and Car [39] have found that when nuclear quantum effects are accounted for, the simulated liquid becomes less structured and more diffusive, and the agreement between AIMD simulations and experiments considerably improves. On the other hand, this result is at odds with a previous similar study in which Chen *et al*[40] found that the quantum vibrations of the hydrogen atoms would indeed increase the strength of the hydrogen bonds in liquid water.

In this chapter, it will show that diffusivity coefficients that are substantially lower than the experimental values are obtained, in agreement with previous and recent findings using similar method. However, different functionals give very different behavior of diffusivity due to the different description of the O-H covalent bond and the hydrogen bond network. This link does not appear to be an artifact of the simulations, but a genuine property of liquid water. The diffusivity is observed to be very directly linked to network imperfection, which is sensitive to the choice of density functional. Including the quantum nuclear effect has been shown by R. Car group to improve the diffusivity by softening the OH bond including zero point energy. However, it is clear that

improvement from this effect is still far from the difference from simulations to experiments. Actually, in a recent study, Habershon *et al*[41] identified the competing contributions from intermolecular and intramolecular quantum fluctuations to cancel out and thus to have a small net effect on the diffusion coefficient.

A thorough study of pressure-induced structural and dynamical effects in liquid water is required. A group of authors(Schwegler *et al*[45]) have already presented a study of DFT water under pressure, but the equilibrium density of GGA water was not explored. In this chapter, I partly confirm and extend their results by using AIMD. More importantly, a full comparison of structural and dynamical properties of liquid water using four different GGA functionals is addressed by studying the intrinsic nature of OH covalent bond, which causes the description of H-bonds to differ.

3.2 Methodology

The simulations are performed using the self-consistent Kohn-Sham approach [51, 52], using the generalized-gradient approximation to exchange and correlation (XC). We choose four commonly used GGA functionals: PBE [48], BLYP[46, 47], RPBE[53] and revPBE[54]. The choice of these functionals is motivated by our interest in studying the effect of exchange and correlation functionals on liquid water structural and dynamical properties.

3.2.1 Basis set

In this study, core electrons were replaced by norm-conserving pseudopotentials [56] in their fully nonlocal representation.[57] Numerical atomic orbitals of finite support were used as the basis set, and the calculation of the self-consistent Hamiltonian and overlap matrices was done using the SIESTA method.[58, 59] A double-ζ polarized (DZP) basis set was used, which has been variationally optimized following the method proposed in Refs.[60, 61]. The validation of the method, pseudopotentials, and basis set can be found in Ref. [28]. In addition, a triple-ζ polarized (TZP)[62] basis set has also been

tested in this study. The summary of the basis test result is presented in Table 3.1.

The results show that the main difference between the DZP basis set used in this study and the well converged TZP basis is that the smaller basis produces a somewhat less structured liquid. The diffusivity is approximately the same for the two basis sets. The first peak in the O-O radial distribution function (RDF) is almost identical, the first minimum is 13% higher. The comparison of the radial distribution function between the TZP basis and the DZP basis is shown in Fig. 3.1. The error of the DZP basis on the location of the first maximum in the O-O RDF is less than 0.6%, indicating that the basis is very good in the description of the H-bond geometry, as already shown in Ref.[28].

In order to evaluate total energy errors associated with our choice of basis set, I have selected 10 snapshots, separated by 2 ps time intervals, from our simulation at density 1.00 g/cm^3. The difference between the TZP and DZP energies is an almost constant value of 0.12 eV/molecule, with a standard deviation of only 7 meV, which can be neglected even when we are studying the small van der Waals effects. Also, in Table 3.1, the details of the two simulations with DZP and TZP are compared. The energy drift is on the order of 10^{-6} a.u./atom/ps, which accounts for a change of only a few Kelvin during 20 ps, well below the statistical fluctuation of temperature from the MD simulation. We have estimated that basis-set-induced errors in the equilibrium pressure are on the same order as the error bar associated with the choice of different initial configurations, which is approximately 1 kbar. Both errors are much smaller than the statistical fluctuations of pressure during the MD simulation, which is on the order of 3-4 kbar. Overall, we can conclude that AIMD of water is not totally insensitive to the basis set choice,[28, 43] shorter basis sets providing slightly less structured liquids in general. However, the results and conclusions presented in this study are well beyond the uncertainties due to these limitations.

Table 3.1: Summary of AIMD NVT simulations results, for liquid water at 1.0 g/cm^3 and 340 K, using the PBE functional. We compare results with a DZP basis using a confining pressure of 2kbar with a run of 20 ps, and a TZP basis using a confining pressure of 2kbar with a run of 15 ps. Temperature T (K), pressure P (kbar), energy drift during the simulation E_{drift} (10^{-6} a.u./atom/ps), self diffusion coefficient D (10^{-5}cm^2/s), height of first peak g_{OO}^{max}, height of first minimum g_{OO}^{min} and position of first maximum r_{OO}^{max} (Å) of the O-O radial distribution function are compared.

Basis	T	P	E_{drift}	D	g_{OO}^{max}	g_{OO}^{min}	r_{OO}^{max}
DZP	353	4.5	-1.5	1.23	2.87	0.58	2.75
TZP	365	5.8	-2.3	1.20	2.85	0.50	2.73

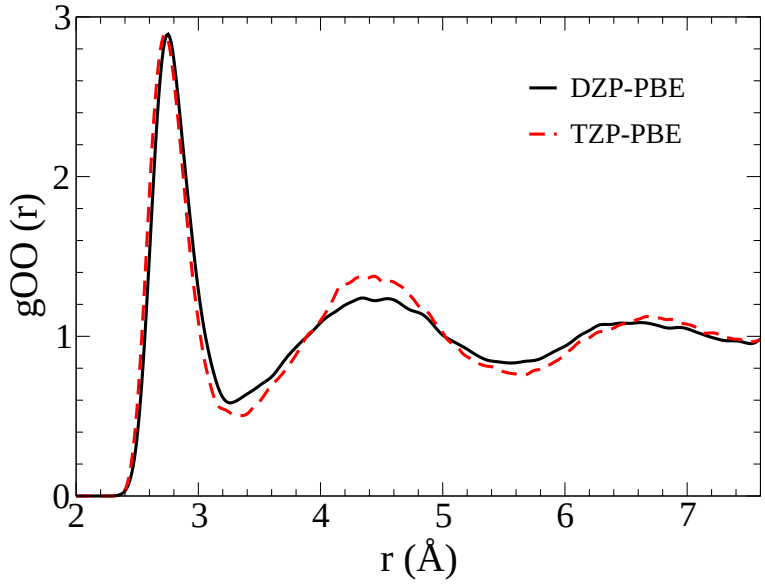

Figure 3.1: Comparison of the O-O radial distribution function (RDF) obtained with the DZP(solid black) and TZP(dashed, red) basis sets (see text) at 1.0 g/cm^3 with PBE functional.

3.2.2 Molecular Dynamics Simulations

All the results are based on AIMD simulations of 64 molecules of heavy water. Classical molecular dynamics simulations, where the electronic potential seen by the nuclei is replaced by an empirical force field, were performed before AIMD equilibration in order to prepare reasonably equilibrated initial

configurations. All empirical-potential-based simulations were performed with the TIP4P force field[63] as implemented within the GROMACS MD package [64, 65] under constant volume and temperature conditions, with a Nose-Hoover thermostat [66, 67] at 300 K, along a 1 ns equilibration trajectory. AIMD simulations were started from these pre-equilibrated systems imposing an additional 3 ps equilibration by means of temperature annealing (velocity rescaling).[68] The actual production runs of the AIMD simulations (20 ps each) were accomplished by constant-energy Verlet's integration, given our interest in dynamical properties. The time step in all simulations, (including empirical force field MD and AIMD) is 0.5 fs.

The simulations are performed under constant volume i. e. fixed cell size and shape, under periodic boundary conditions. Rather than performing a constant-pressure simulation to establish the theoretical equilibrium density under ambient conditions, we chose to perform a series of simulations by changing the volume of the unit cell while keeping the number of water molecules fixed. The reduced system size produces large pressure and temperature fluctuations and requires larger statistics for reliable comparisons between different simulations. Therefore, we compute three different trajectories for each density, starting from different equilibration configurations. In total, over 500 ps of AIMD simulations were produced in this study.

We use four different GGA functionals to study liquid water structural and dynamical properties. The temperature of the simulations using GGA functionals were set higher than 300 K due to the reason mentioned in the introduction of this chapter. With the PBE, BLYP functional I use ∼360 K[28] and with revPBE, RPBE I use ∼330 K.[69]

3.2.3 System Size Effects

System size effects on structural and diffusive properties of simulated liquid water have been addressed before. Most studies[25, 35] used empirical potentials and found that size effects seem not to be a problem for those properties. In AIMD simulations, size effects have been shown to be rather small for structural properties,[28, 70] but much larger for dynamical properties,[70,

71]meaning that finite size scaling is needed to obtain the infinite-size self-diffusivity coefficient.[72] With such finite size scaling, Kuhne *et al* found[70] an improved self-diffusivity but still much smaller than experiment.

I have explored the influence of size-dependent boundary conditions on both structural and dynamical properties of the system. The dependence of average pressure on the system size has also been studied in detail. These analyses were performed by means of classical molecular dynamics simulations. It seems reasonable to assume that size effects are robust enough to the change of interaction potential and that results obtained from force-field-based simulations are adequate to estimate the error due to the reduced size of the system in our AIMD studies.

I have performed molecular dynamics simulations of five different system sizes (32, 64, 128, 512 and 1024 molecules) at four different densities (0.95, 1.0, 1.1, and 1.2 g/cm^3) with the empirical force field TIP4P.[63] These simulations were equilibrated at 300 K along 100 ps runs using a Nose-Hoover thermostat. Subsequently, they were allowed to continue for 1 ns, using a Verlet integrator.[68]

The convergence of average pressure of TIP4P simulations with system size is shown in Fig. 3.2. Simulations with 32 water molecules result in a large discrepancy with the converged value. With 64 molecules the pressure is not yet fully converged but the error is much smaller. Considering the need for long simulation times and the large number of simulations required for this study, we chose to limit our systems to 64 water molecules to study the density-pressure dependence.

3.3 Structural Properties of Water

Liquid water is believed to have the topological character of a tetrahedral network due to the geometrical characteristics of the hydrogen bond (HB). The concept of the HB network in liquid water, as an ice-like network of amorphous and transient character was well defined and characterized in 1980 by F. Stillinger [12]. In his work he pointed to the special angular distributions of the HBs as being responsible for many of the anomalous water properties.

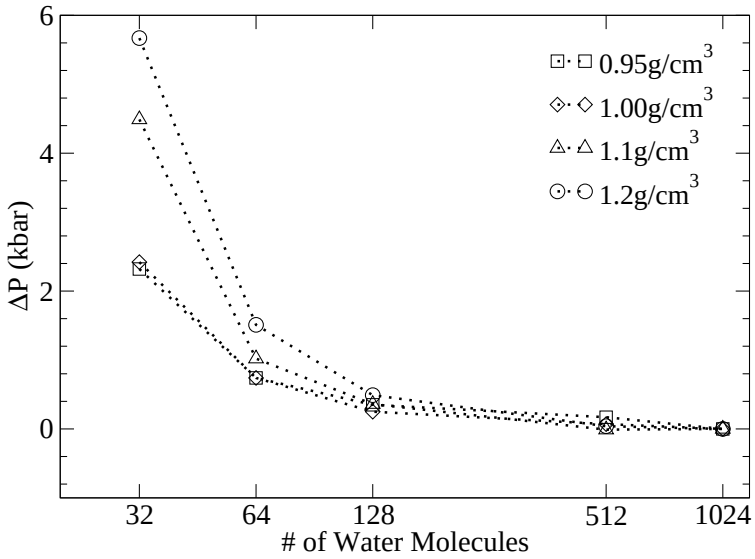

Figure 3.2: Convergence of average pressure with system size. ΔP is the pressure difference between the system of N molecules and that of 1024 molecules, at 300 K and four different densities. All the simulations in this figure were performed using the TIP4P empirical force field.

He also pointed to the connection between the different known ice network structures and the landscape and topology of the network in the liquid. In his computer simulations he related the RDFs of liquid water to the average coordination of the molecules in terms of the HBs defined after a geometrical criterion. L. Bosio et al. [17] in 1983 discovered that in the result of the subtraction of the RDFs at two different temperatures, also called isochoric temperature differential functions only the heights of the peaks and valleys (but not their positions!) depend on temperature. E. Stanley et. al[18] suggested that the RDF change due to temperature is because of the increasing number of defects which they called clusters with five neighbours in the first coordination shell. They explored the geometrical characteristics of these two components and associated the two distributions with molecules that have either four or five neighbors in the first coordination shell. And, even more, they suggested that the five-bonded component is the defect component that increases with T.

Although in our simulation we do observe the decrease of the height of the first peak of oxygen-oxygen radial distribution functions, as suggested by many previous studies, we believe the change due to the simulation temperature is far from the difference from different pressures and GGA functionals as shown in Fig. 3.3. So we neglect the small temperature effects on RDFs in our analysis.

Fig. 3.3 compares the O-O RDF of liquid water at 0.95 g/cm^3 for the PBE and revPBE functionals. The temperature difference between the the two simulations is under 15 K, and should have a effect of about 0.1 units drop on the RDF's first peak height[45], rather small compared with that resulting from pressure differences shown in this work. We compare our results with two different experimental data sets[75, 76], both obtained from Ref.[76]. The revPBE RDF matches the experiments rather well. Although the onset and position of the first peak are clearly shifted to the right, there is a large uncertainty in the experimental data for this peak (see Ref.[76]). However, at 0.95 g/cm^3, revPBE water is at a very large pressure. When this pressure is released, the density drops to ∼0.65 g/cm^3 and the agreement with the experimental RDF is totally lost[77]. Both the first and second peaks move further to the right. This effect is also observed in PBE. It should be noted that, for PBE, the height of the first minimum remains well below the experimental value and is barely modified, either by temperature or pressure effects[77].

Fig. 3.4 compares the oxygen-oxygen radial distribution functions (RDFs), $g_{OO}(r)$, of liquid water under high pressure (at 0.95 g/cm^3) and low pressure(at 0.65 g/cm^3) for the four GGA functionals considered in this study. The differences of average temperature at 0.95 g/cm^3 and at 0.65 g/cm^3 are within 30 K, and still should have negligible effects resulting from temperature difference on the RDFs[45] compared with those resulting from pressure differences.

First it is worth noting that even experiments have different results for the g_{OO}(r) of liquid water. The two experiments show different heights of the first peak of g_{OO}(r). However, the position of the first peak is the same within a small error (less than 0.2%), thus making this number important when comparing simulation results with experiments. When comparing the g_{OO}(r) obtained from different GGA simulations with experiments, PBE is the most widely used because it has the best agreement with the position of the first

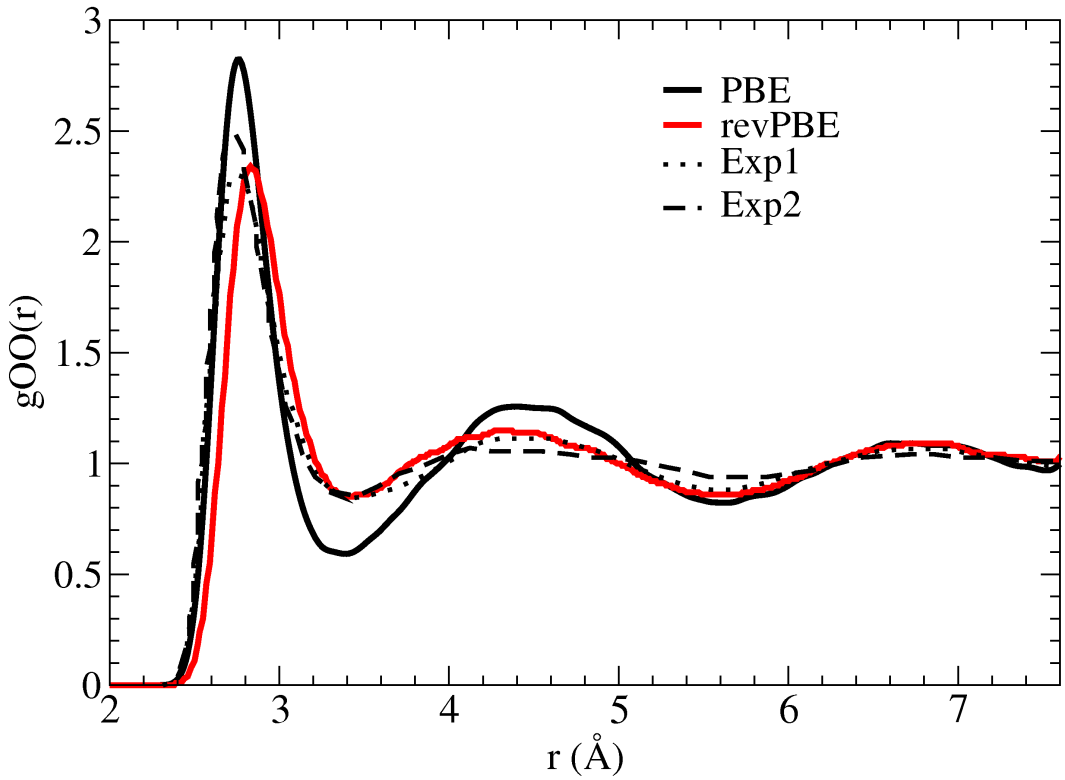

Figure 3.3: O-O radial distribution functions (RDF) of liquid water for AIMDs in this work, at 0.95 g/cm^3 with PBE at 354 K (solid black line) with revPBE at 341 K (solid red line). These temperatures are chosen[28] so that the structure and diffusivity compare best with those of experiments at 300 K. Exp1 (dotted line) and Exp2 (dashed line) data are the experimental data in Refs.[75] and [76] respectively.

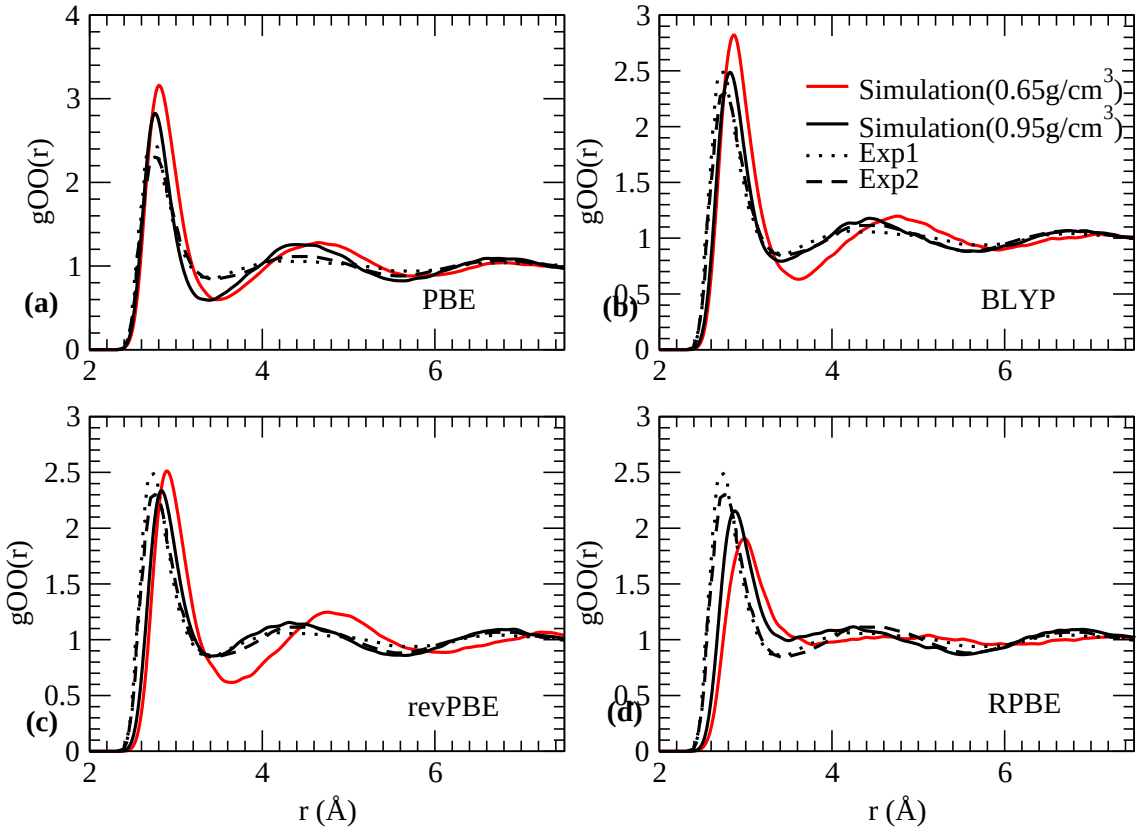

Figure 3.4: Comparison of the oxygen-oxygen RDFs of water from experiments(1.0 g/cm^3) at 300K[75, 76] and those from AIMDs in this work, at density 0.65g/cm^3 and 0.95g/cm^3, by using (a) PBE at 360K, (b) BLYP at 350K, (c) revPBE at 340K and (d) RPBE at 340K. The temperature of AIMD simulations are artificially set to be higher than desired temperature 300K to achieve good structure and diffusivity for liquid water.[28]

peak of $g_{OO}(r)$. BLYP and revPBE are very similar, both resulting in around 2% increase of the O-O distance due to stronger O-H covalent bonds and thus a weaker hydrogen bond interaction. RPBE has the worst comparison due its much more overestimated O-H covalent bond for water molecule. This can be clearly seen from Fig. 3.5, where electronic density of single water monomer with PBE and RPBE density functionals are shown. The electronic density of the water monomer shows that the PBE O-H bond is more ionic while the RPBE O-H bond is more covalent. Thus the RPBE water structure deteriorates due to this overestimation of the O-H covalent bond and corresponding underestimated hydrogen bond.

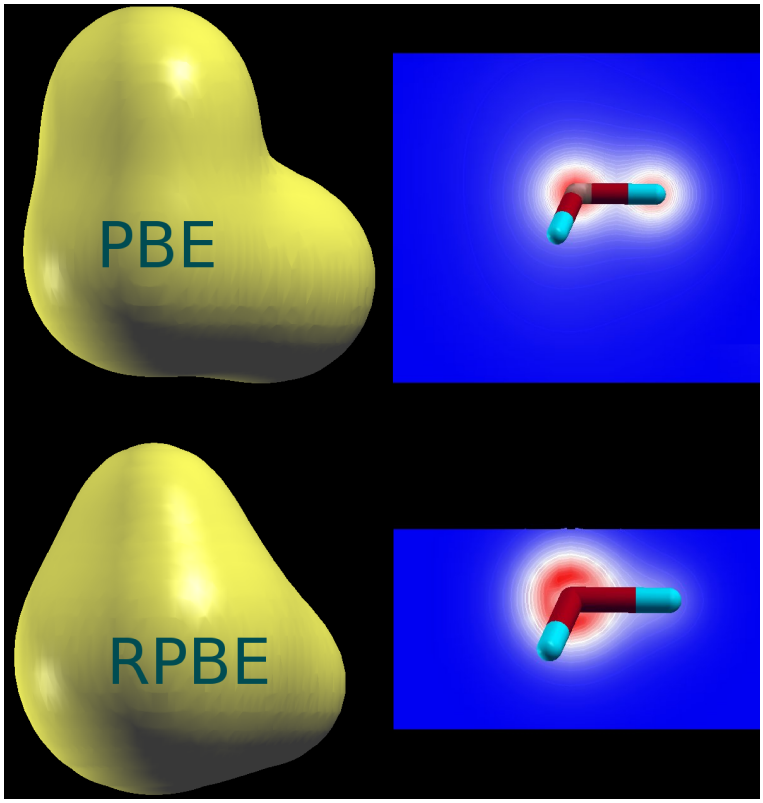

Figure 3.5: Comparison of the electronic density of a water monomer using two exchange and correlation functionals: PBE (top) and RPBE (bottom). The right panels shows the electronic density at the plane that contains one of the covalent O-H bonds. The red represents higher electronic density.

In Fig. 3.4, as expected, increasing the density (or pressure) of the simulations shifts the positions of the first peak in the oxygen-oxygen RDFs inward. Important changes are observed in the position of the first minimum and second maximum in $g_{OO}(r)$, which is the consequence of the decrease of $\widehat{OHO}$ hydrogen bond angle induced by pressure. However, it should be noted that, for PBE, the height of the first minimum remains well below the experimental data and is barely modified, either by temperature or pressure effects. The structure of RPBE water is significantly different from other GGAs and experiments. It has a weaker hydrogen bond network which can be seen in Fig. 3.3(c), showing a longer oxygen-oxygen distance.

The three density functionals: PBE, revPBE and BLYP all result in an increase of the first coordination number similar to results in Refs. [45, 91] when increasing pressure. The first neighbor coordination shell around oxygen atoms is significantly changed due to the collapse of the second-nearest neighbor coordination shell with pressure, resulting in more linear hydrogen bonds between the central oxygen atom and the first shell.[45, 91]

However, RPBE shows opposite effect which results in an decrease of the first coordination number when increasing pressure for the system. This could be explained by its underestimated hydrogen bond nature. Because it is much less structured, applying strong pressure to this system forces oxygen atoms to become closer and form stronger hydrogen bonds within the first coordination shell. This will make the underestimated hydrogen bond from RPBE stronger and thus number of hydrogen bonds within first coordination shell will also be increased. In summary, this unique opposite effect of introducing pressure demonstrates another problem of reproducing correct chemical and structural properties using RPBE density functional to simulate liquid water.

3.4 Dynamical Properties of Water

The diffusion coefficient is calculated using the Einstein relation:

$$6D = \lim_{t\to\infty} \frac{d}{dt} < |r_i(t) - r_i(0)|^2 > \tag{3.1}$$

Eq. 3.1 is evaluated by computing the mean square displacement (MSD) of the oxygen atoms for multiple initial configurations equally spaced by 7 fs.

If equilibration is still taking place and the diffusivity is not stabilized yet, it misleads to a reading of the slope from Fig. 3.6 as that of an equilibrated system.

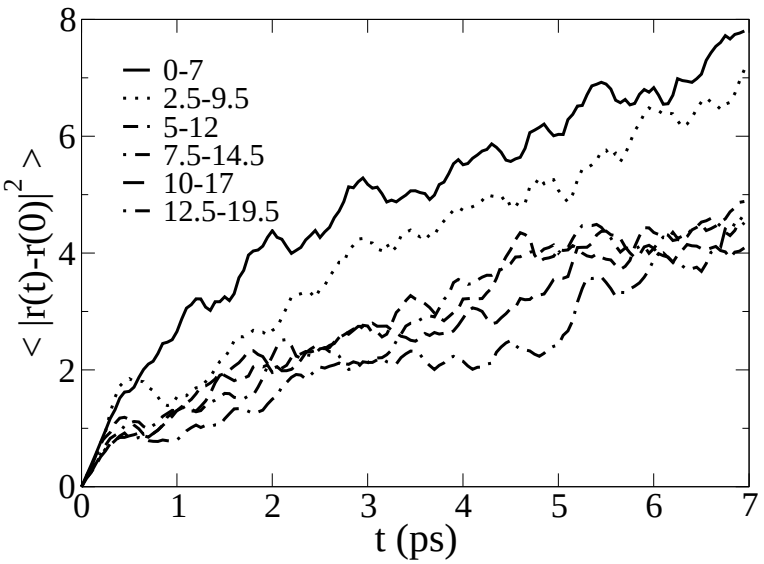

Figure 3.6: Mean square displacement for the oxygen atoms vs time for PBE water at 1.0 g/cm^3. The plots are computed in 7-ps-wide windows every 2.5 ps.

Fig. 3.6 shows an example of how diffusivity of liquid water in this work is calculated. In Fig. 3.6, mean square deviation for oxygen atoms vs time for PBE water at 1.0 g/cm^3 is calculated and plotted to determine the self-diffusivity. The plots are computed in 7-ps-wide windows every 2.5 ps so that we can see a evolution of self-diffusivity relaxation. It usually takes 5 ps to equilibrate the liquid system. However, obtaining a slope from them is still tricky and not devoid of ambiguities, including the choice of start and end times within the time window for the linear fit. It has been checked, however, that, if systematic and carefully done, the variability in the extracted values does not affect the results in a substantial way for the purposes of this study. This moving-window approach allows observing the evolution of the diffusivity

with time, and address the equilibration problem. In practice, since during the very first 5 ps slope of MSD vs time is not equilibrated, I consistently use the average slope value after 5 ps time window to determine the slope and thus self-diffusivity. Another advantage of using this time-window method is that we can get an estimation of the error of the self-diffusivity from simulations, which can be determined by the standard deviation. The error is approximately 30%. However, since the difference of self-diffusivity due to the choice of GGA functionals and pressures(densities) can be far more than the error due to the choice of t ed.

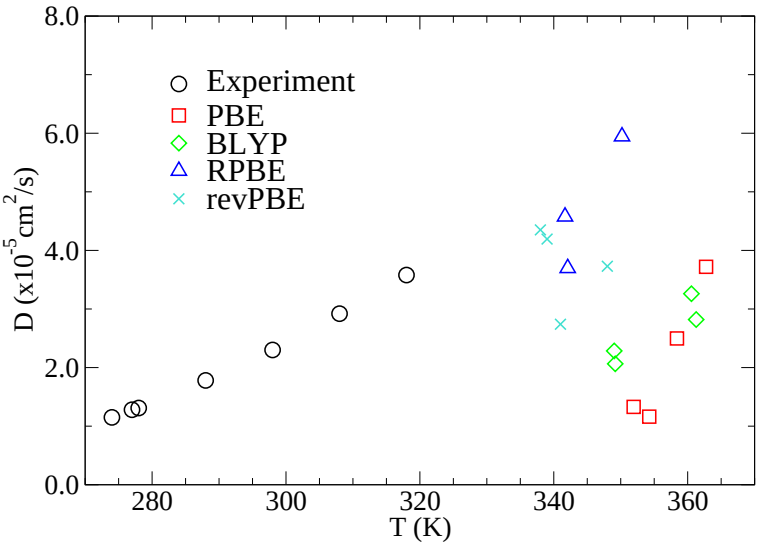

Figure 3.7: Self-diffusion coefficient vs temperature for PBE(square), BLYP(diamond), revPBE(cross), RPBE(upper triangle) and experiment(circle)[33]. For each GGA density functional, self-diffusivity coefficients of a series of simulations at densities ranging from 0.65 g/cm^3 to 0.95 g/cm^3 are calculated.

In Fig. 3.7, self-diffusion coefficients are calculated using the time window methods for all four GGA functionals at different densities(pressures). It is obvious that smaller pressure(density) will result in a weaker hydrogen bond. At the same time, the average volume occupied by each molecule is also decreased by lower pressure(density). The two effects both increase the self-diffusivity of the liquid system. For each GGA functional, the diffusivity will increase with

lower density of simulated liquid water when pressure is released.

Confirming previous results [28], we also find a temperature overestimation for AIMD with PBE and BLYP that required scaling up by 16% to 20% to give an acceptable agreement with experimental diffusivity of water (circle in the Figure). For AIMD with revPBE and RPBE, we obtain much better results by only overestimating the temperature by 6% to 15%. It is unclear, however, what kind of agreement one would obtain for other properties, since the local dynamics is controlled by atoms moving at velocities corresponding to the actual temperature of the simulations. It is clear that semi-local exchange-correlation functionals like these ones miss the non-local correlation effects that give rise to dispersion forces. The non-local correlation dispersive van der Waals interaction effect on liquid water diffusivity will be studied in details in Chapter 4. One of the most important conclusion will be that this non-local effect will significantly improves the diffusivity of the simulated liquid water.

3.5 Hydrogen Bond Network

The molecules in water bind to each other by HBs. Even if the character of this kind of bond is still controversial, two important features are clear, namely, its strength (between that of a covalent bond and a van der Waals one), and its directionality. In water, each molecule tends to be surrounded by four others, donating two HBs and receiving two HBs in a nearly tetrahedral arrangement. This translates into a HBs network with a majority of four-coordinated molecules. However it also contains tetrahedral defects due to the presence of under-coordinated and over-coordinated molecules. The population of these under-coordinated defects correlates with an increasing self diffusion constant. The average bond life-time of the HBs in liquid water is of the order of 1ps. [92]. We perform in this section an analysis of the HB network in our simulations.

To study the population of HBs near molecules in our simulations we need a criterion to decide the existence of a HB. Our criterion relies on two aspects, (i) an oxygen-oxygen distance shorter than the first minimum of the $g_{OO}(r)$ [24] and (ii) a HB angle larger than an chosen minimum value. As in Ref. [24],

we choose a minimum angle 145^0. For the characterization of network defects, a temporal criterion for the definition of a HB has been included, since fluctuations of distances or angles close to the critical values would otherwise appear as short-lived coordination defects, masking the defect statistics that needs to be monitored. Keeping track of HBs with life-times longer than typical vibrational or librational periods is enough for the purpose.

Fig. 3.8 shows the equilibrium distribution of the population of HBs for all XC functionals in this study at the same density $0.95 g/cm^3$. Effective temperatures for all simulations are close to 300K. Note the asymmetry of all four distributions; everything happening between the ideal coordination and under-coordination. PBE water has the least number of under-H-Bonded defects and RPBE water has the most, indicating that PBE favors the formation of a more tetrahedral structure. On the contrary, RPBE is less structured due to more defects. This can be explained by the overestimation of RPBE O-H bond, which results in weaker hydrogen bonds.

Fig. 3.9 shows the change of the distribution of coordination at low and high pressures. It shows that high pressure increases the defect concentration. For all GGA functionals, the under-coordination defects are decreased while the ideal coordination ones are increased, indicating that the HB network structure has been changed under high pressure. This is similar to previous findings as in [45, 91]. However, Fig. 3.9 only considers HBs within first coordination shell. As already shown in 3.3, the second coordination shell collapses under high pressure. Therefore an increase in ideal coordination only within first coordination shell under high pressure does not necessarily indicate a stronger HB network. On the contrary, the HBs between the first and the second shell molecules are broken under high pressure, allowing more water molecules to connect with four other water molecules within the first coordination shell.

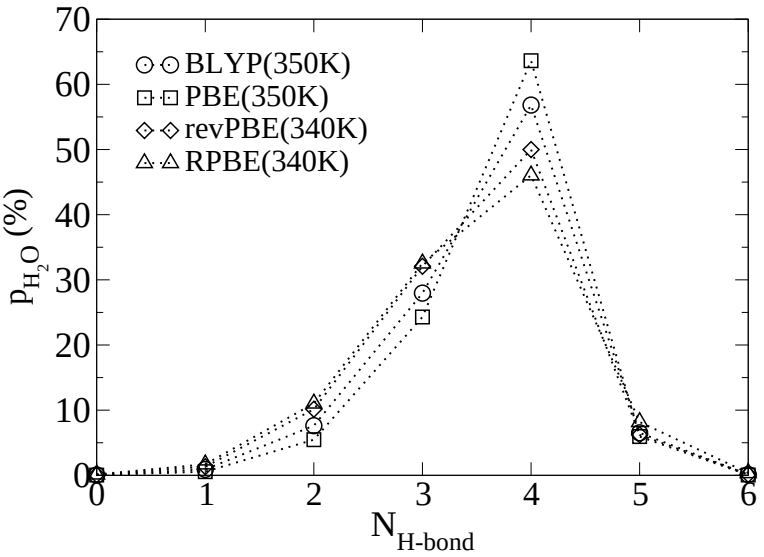

Figure 3.8: Distribution of the population of the neighbor HBs of molecules (N_{HBs}) for all the GGA XC functionals in this study. p_{H_2O} is the percentage of water molecules that make N_{HBs}. PBE(square), revPBE(diamond), BLYP(circle) and RPBE(triangle). All simulations in this graph are performed for liquid water at density 0.95 g/cm^3. Effective temperatures of all simulations are close to 300K.

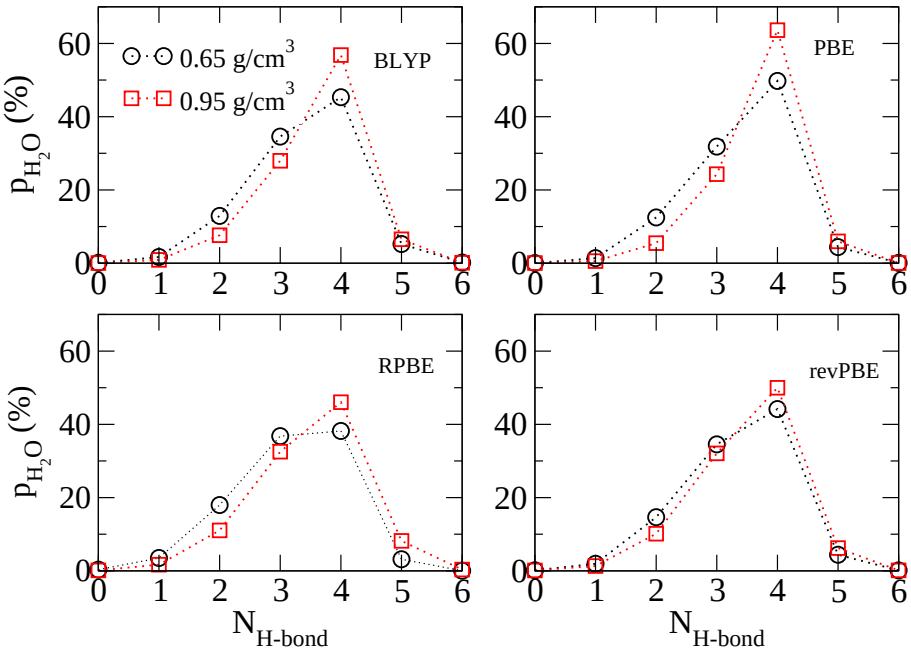

Figure 3.9: Comparison of the distribution of molecules with different coordination for low density 0.65g/cm^3 and high density 0.95g/cm^3 with BLYP, PBE, RPBE and revPBE.

3.6 Equilibrium Density of Water in Simulation

Table 3.2 summarizes the parameters used, and the average values obtained, in all our AIMD simulations, spanning four GGA functionals, two van der Waals functional that will be studied in detail in the next chapter and a wide range of pressures(densities). As explained before, the simulation temperatures were chosen, for each functional, to achieve a reasonable comparison with the experimental diffusivities and radial distribution functions.[28, 69] [1]

Pressure-density curves obtained with four GGA functionals (BLYP, PBE, RPBE and revPBE) and two vdW-DFs (DRSLL and DRSLL-PBE) are compared in Fig. 3.10. Because of the reasons given in the introduction, each functional is simulated at a different temperature (see Table 3.2), but we would like to stress that this has only a minor effect on the resulting average pressures.[73, 74] To illustrate this, we show in Fig. 3.10 the experimental densities at 300 K and 360 K for $P = 1$ atm. Their difference is much smaller than that between different functionals.

All GGA functionals result in theoretical equilibrium densities considerably lower than the experimental value ($\rho = 0.997$ g/cm^3 at $P = 1$ atm). The equilibrium density of PBE is 0.85 to 0.90 g/cm^3, close to the value presented in Refs. [32, 45] and around 12% lower than experiments. The BLYP equilibrium density of 0.76 to 0.85 g/cm^3, also within the range provided by Schmidt *et al*[32] and 19% lower than experiments. The revPBE and RPBE density is 0.63 to 0.75 g/cm^3, or 31% less dense than experiments.

The large differences in the calculated densities of similar GGAs are surprising and require some analysis. Like many liquids, water maintains much of the short-range order of its solid. In ice Ih, a rigid framework of hydrogen bonds forces a tetrahedral coordination and a relatively open structure with large voids. Four of these interstitial voids surround each molecule, along orientations opposite to those of its H bonds (we will call them 'anti-tetrahedral' orientations). In the liquid, entropy implies that part of the H bonds are

[1] a: As there is no sharply identifiable first minimum in $g_{OO}(r)$ at 1.05 g/cm^3, we can not provide the accurate value here.

Table 3.2: Simulations parameters used, and average values obtained in this work: mass density ρ, exchange-correlation functional, average temperature T_{avg}, diffusion coefficient D, position r_{OO}^{max} of first maximum in $g_{\mathrm{OO}}(r)$, position r_{OO}^{min} of first minimum in $g_{\mathrm{OO}}(r)$, average coordination number, and average number of hydrogen bonds $N_{\mathrm{H-bond}}$. For each calculation, quantities are averaged over 20 ps. At ambient conditions, the experimental self-diffusion coefficient is 2.2×10^{-5} cm^2/s for H_2O and $1.8{\times}10^{-5}$ cm^2/s for D_2O[33]. The experimental coordination number is 4.7[35]

ρ (g/cm^3)	Functional	T_{avg} (K)	D (10^{-5}cm^2/s)	r_{OO}^{max} (Å)	r_{OO}^{min} (Å)	Coord.	$N_{\mathrm{H-bonds}}$
0.65	BLYP	361	2.82	2.87	3.63	3.85	3.49
0.75	BLYP	361	3.26	2.86	3.53	3.89	3.40
0.85	BLYP	349	2.29	2.83	3.45	4.03	3.58
0.95	BLYP	349	2.01	2.82	3.40	4.33	3.61
0.65	PBE	363	3.72	2.81	3.52	3.77	3.43
0.75	PBE	358	2.49	2.80	3.47	4.21	3.51
0.85	PBE	352	1.33	2.77	3.41	4.28	3.67
0.95	PBE	354	1.16	2.76	3.36	4.31	3.69
1.00	PBE	353	1.18	2.75	3.28	4.23	3.78
0.65	RPBE	354	13.93	2.98	3.81	3.58	2.73
0.75	RPBE	342	4.58	2.93	3.69	3.63	3.19
0.85	RPBE	350	5.95	2.91	3.66	3.83	3.19
0.95	RPBE	342	3.70	2.87	3.52	3.90	3.49
0.65	revPBE	338	4.35	2.89	3.62	3.58	3.34
0.75	revPBE	339	4.19	2.88	3.55	3.79	3.56
0.85	revPBE	348	3.73	2.85	3.51	4.09	3.46
0.95	revPBE	341	2.74	2.83	3.45	4.46	3.50
0.95	DRSLL	296	2.68	2.93	3.50	4.87	3.63
1.00	DRSLL	300	2.63	2.92	3.46	4.90	3.68
1.05	DRSLL	303	2.12	2.92	a	-	-
1.00	DRSLL-PBE	304	2.08	2.83	3.38	4.52	3.58

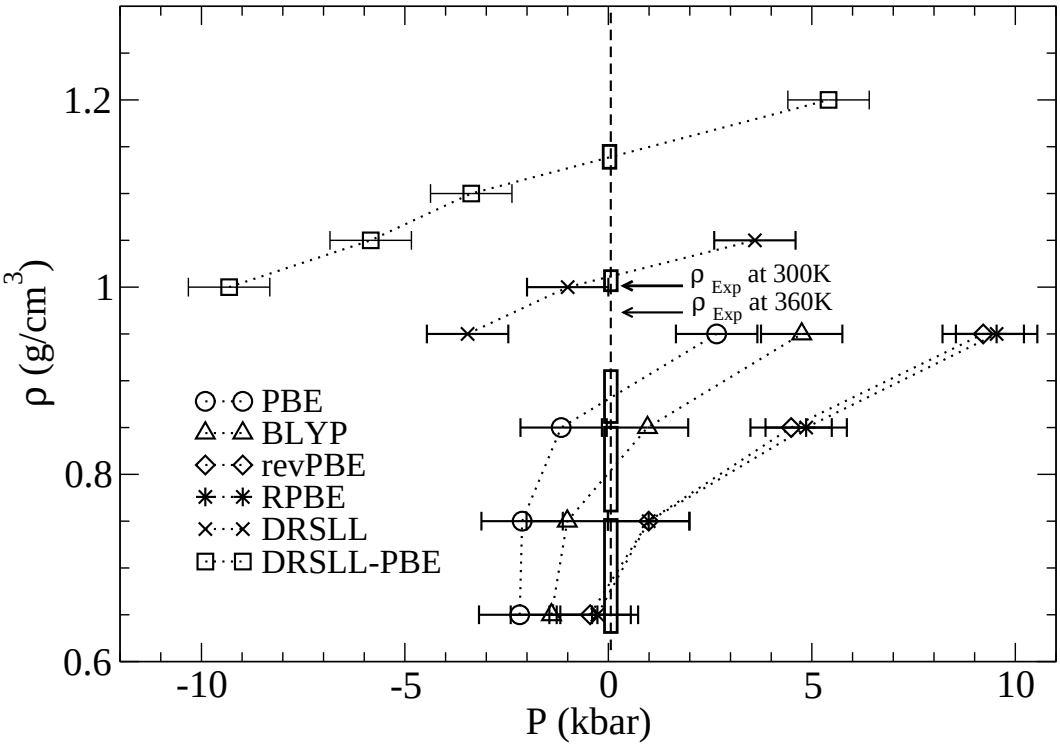

Figure 3.10: Pressure-density curves obtained in AIMD simulations with different GGA and vdW XC functionals. The error bars are standard deviations of average pressures in three different runs with the same density, XC functional, and temperature. The simulation temperatures can be found in Table 3.2. The boxes show the estimated range of equilibrium densities at $P = 1$ atm $\simeq 1$ bar. The arrows indicate the experimental densities at 300 K and 360 K and 1 atm. [73]

broken and part of the interstitial voids are occupied. Thus, we can imagine three different properties of a functional or force field, that will determine the density of liquid water: *i*) the length of the hydrogen bonds, causing a possible dilation of the H-bond framework; *ii*) the strength of these bonds, that determines the average H-bond coordination; and *iii*) the potential energy of molecules at interstitial positions, that determines their average occupation.

With a rigid H-bond framework, the density would be proportional to d_{OO}^{-3}, where d_{OO} is the average O-O distance. The change in d_{OO} between PBE and revPBE (see Table 3.2) is ∼3%, which would translate into a difference in density of just ∼10%, far from the ∼25 % observed.

However the density also depends on the number of H bonds, which increases with their strength. Fig. 4.3(b) shows that, despite the similarity of the two functionals, the H bond energy is ∼50% larger with PBE than with revPBE. As a consequence, the first coordination peak in the O-O radial distribution function (RDF) $g_{\mathrm{OO}}(r)$, plotted in Fig. 3.3, is ∼30% higher with PBE, showing that the H-bond network is better preserved with this functional.

All put together, the difference in densities within the first coordination shell, calculated as $\frac{N_{coor}+1}{4\pi r_{\mathrm{OO}}^{min}/3}$ (with values from Table 3.2), where N_{coor} is the average coordination number and r_{OO}^{min} is the radius of the first minimum in $g_{\mathrm{OO}}(r)$, is larger than 30%.

3.7 Conclusion

A series of AIMD simulations of liquid water have been carried out using the SIESTA method, for temperatures between 300K and 360K. The conclusions of the present study can be summarized as follows:

- Water under standard atmospheric pressure condition simulated with BLYP, PBE, RPBE and revPBE is less dense than is seen in experiments. PBE results in 10% less density, BLYP results in 20% less and RPBE, revPBE result in 35% less. On the other hand, DRSLL water is only 2% more dense than the experimental density of liquid water and thus is in good agreement with experiments. This indicates some important

structural change due to the dispersion interaction and will be explained in the next chapter.

- RPBE and revPBE water are less structured than BLYP and PBE. PBE gives the best description of structure. So far PBE is still the best GGA exchange and correlation functional to study liquid water.

- The effective temperature for revPBE and RPBE is less than the simulation temperature by -6 to -9% while for BLYP and PBE it is -20 to -23%. The diffusivity obtained for DRSLL is very close to experiment at room temperature which makes the study of van der Waals interaction promising.

- RPBE water has the weakest hydrogen bond strength due to the overestimated O-H covalent bond while PBE water has the strongest hydrogen bond strength.

- With ascending pressure, GGAs water will be less structured due to the fact that HBs between first and second coordination shell break causing the second coordination shell structure to collapse.

In this chapter we have studied the most common GGA functionals used in today's gigantic DFT field. Although there is no perfect GGA XC functional till present that can reproduce both structural and diffusive properties of liquid water, including non-local dispersion interaction within DFT does show significant improvements in terms of diffusivity and equilibrium density under ambient condition. However, its impact on structural and especially, HB network, is not clear and requires a detailed study which will be presented in the next chapter.

Chapter 4

The Effect of van der Waals Interaction on Water

Ab initio molecular dynamics (AIMD) simulations of liquid water, based on density functional theory (DFT), yield structural and diffusive properties in reasonable agreement with experiment when artificially high temperatures are used in the simulations for gradient-corrected (GGA) functionals such as BLYP[46, 47], PBE[48], revPBE[54] and RPBE[53], with NVT ensemble. The equilibrium density, at ambient conditions, of DFT water has been shown in the previous chapter to be underestimated by different GGA functionals for exchange and correlation, and corrected by the addition of non local correlation interactions to describe van der Waals (vdW) interactions.

In this chapter, I will present a DFT-AIMD study of liquid water using the van der Waals density functional (vdW-DF) of Dion et al. [Phys. Rev. Lett. **92**, 246401(2004)]. When vdW-DF is used, the density improves drastically and the experimental diffusivity is reproduced without the need of thermal corrections. I also analyze the origin of the density differences between all the functionals. I show that the vdW-DF increases the population of non-H-bonded interstitial sites, at distances between the first and second coordination shells. However, it excessively weakens the H-bond network, collapsing the second coordination shell. This structural problem is partially associated to the choice of GGA exchange in the vdW-DF. I show that a different choice for

the exchange functional is enough to achieve an overall improvement both in structure and diffusivity.

4.1 Introduction

Van der Waals (vdW) dispersion interactions, due to non local electron-electron correlations, are not treated properly by the local density approximation[78] (LDA) and GGA[48, 79, 80] functionals, in which electron correlations are treated as local or semi-local effects. It is known that in water, due to the high polarizability of oxygen,[80–82] vdW interactions have a significant contribution to the binding.

When vdW interactions are added, using the interatomic pair potentials proposed by Grimme,[49] the experimental density is recovered. The vdW attraction contributes to strengthening both H-bonds and non-H-bond interactions[83] and it increases the overall cohesive energy in the liquid. A recent study by Schmidt *et al.*[32] of liquid water under isothermal and isobaric condition, using both GGA and so-called DFT+dispersion (DFT-D) method has analyzed this question in detail. They have shown that two of the most commonly used GGAs, BLYP[46, 47] and PBE[48] have an equilibrium density of 0.75 and 0.88 g/cm^3 respectively, 25% and 12% below the experimental value. Schmidt *et al* have studied the vdW effect on the density of water with the PBE-D method,[49] which includes an interatomic pair potential correction added to the PBE functional.[32] They showed that the density of PBE-D water is very close to the experimental value, and the resulting liquid is also structurally closer to experiments. The dynamical properties of their liquid were not accessible due to the use of both temperature and pressure thermostat in their simulations.

Furthermore, classical force fields, that represent electronic dispersion correlations with $-1/r^6$ interatomic pair potentials, could be inaccurate because these correlations are not atom-centered in principle and they depend on the instantaneous electronic distributions of electrons of each atom and molecule. In fact, van der Waals interaction is nothing but a dipole-induced dipole interaction.

Since the current DFT description of liquid water overestimates intermolecular binding, it is not clear whether vdW interactions will reduce the difference with experiments of various magnitudes. However, from the physics point of view, the attractive vdW effects could be especially relevant to increase the density of the simulated liquid, bringing it closer to experiment, as Schmidt *et al* have seen using the PBE-D method.

As seen in Fig. 3.10, the equilibrium density computed with the DRSLL vdW-DF is 1.02 g/cm^3, only 2% *above* the experimental value. This is much better than any of the commonly used GGA functionals which give too low a density. The shape of $\rho(P)$ is also different, and DRSLL water has a much smaller compressibility (larger bulk modulus), at $P = 1$ atm, than any of the GGAs, indicative of a very rigid liquid seen as a smaller slope in Fig. 3.10.

The O-O RDF of DRSLL water shows large disagreements with experiments, as shown in Fig. 4.1. O-H and H-H RDFs are presented in Ref.[84]. The average first neighbor distance, is longer than the experiments. The second coordination peak in $g_{\mathrm{OO}}(r)$ 'collapses' significantly with this functional, and an anomalous hump at $r = 3.8$ Å appears.

Differences between functionals in their liquid H-bond interactions can be characterized by relaxing typical liquid-phase structures.[85] Table 4.1 shows several characteristic magnitudes calculated after relaxing five pentamer clusters, randomly chosen from my AIMD,[86] with different functionals (but with the same initial geometries for all functionals). The table shows that DRSLL increases the H-bond binding energy of revPBE but it also yields a longer H-bond, producing the shift of the first coordination peak to longer distances. This overestimation of DRSLL binding distances has been observed in many other systems.[50, 87]

4.2 Effect of PBE Exchange

As mentioned before, the exchange energy in the DRSLL functional is taken from the revPBE formulation.[50] This choice reduces, relative to PBE, the spurious exchange-induced binding in simple systems like noble gas dimers.[50] However, revPBE underestimates the H-bond interaction, which translates

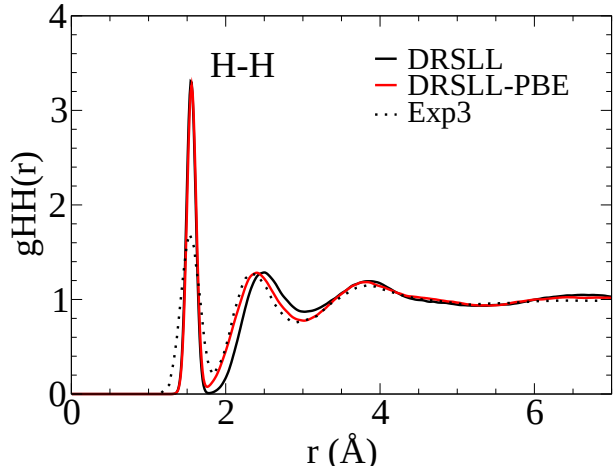

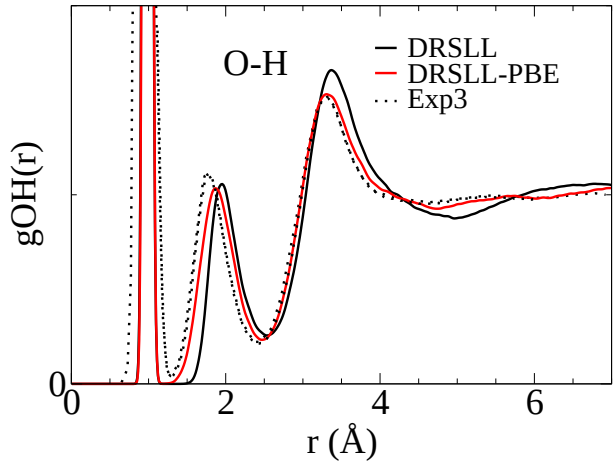

(b)

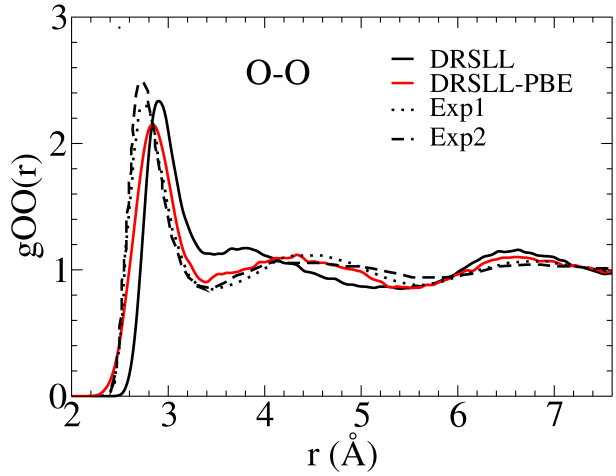

(c)

Figure 4.1: Comparison of the hydrogen-hydrogen, oxygen-hydrogen and oxygen-oxygen RDFs obtained with DRSLL(solid line), DRSLL-PBE(dashed line) functional and experimental result: Exp1[75], Exp2[76] and Exp3[34, 35]. Both simulations and experiments are at 1.0 g/cm^3 and 300K.

Table 4.1: Comparison of average H-bond energy E_{HB}, and distance d_{HB}, first neighbor O-O distance d_{OO}, and intramolecular O-H bond length d_{OH} obtained by relaxing the same five pentamer clusters with different XC functionals. Each cluster contains a randomly-chosen central molecule plus its first neighbors.

Functional	E_{HB} (eV)	d_{HB} (Å)	d_{OO} (Å)	d_{OH} (Å)
BLYP	0.222	1.921	2.881	0.978
PBE	0.262	1.872	2.809	0.979
revPBE	0.199	2.022	2.974	0.974
DRSLL	0.225	2.022	2.980	0.974
DRSLL-PBE	0.290	1.918	2.833	0.976

into larger O-O distances and a clear under-structuring of the RDF, compared to experiments. Therefore, it is worth studying the effect of combining vdW correlations, as described by the DRSLL functional, with a stronger H-bond interaction, as obtained using PBE exchange. Thus, by replacing the revPBE exchange in DRSLL by PBE exchange, we will refer to this functional as DRSLL-PBE. Recent studies[88, 89] have shown that minor modifications of the exchange enhancement factor, in the same line as that used here, can improve geometries and binding energies of small molecular systems. However in this study I chose the original DRSLL and DRSLL-PBE to allow comparisons with their GGA counterparts.

Simulations are performed with DRSLL-PBE for 1.00, 1.05, 1.10 and 1.20 g/cm^3 at 300 K. The data points in Fig. 3.10 for this functional represent a single simulation each, and the same error bars are obtained as for DRSLL. At 1.00 g/cm^3, the average pressures are $\sim$10 kbar, indicating that the strong binding of PBE exchange, added to that induced by vdW correlations, has a net effect of over-correcting the positive pressure of GGAs. I find an equilibrium density at 1 atm of 1.13 g/cm^3 Indeed, the pressure reduction achieved by DRSLL versus revPBE is 13 kbar, close to that of DRSLL-PBE versus PBE, 14 kbar.

As shown in Fig. 4.1, DRSLL-PBE recovers an O-O RDF similar to experiments, without an artificial increase in the simulation temperature. The height of the first minimum in $g_{\mathrm{OO}}(r)$ is very close to the experimental one, and the anomalous hump displayed by DRSLL is almost completely eliminated. The

fact that the long range tail of $g_{OO}(r)$ matches closely the experimental one may be indicative of a correct characterization of the long range structure of water, obtained when vdW interactions are included[**?**].

4.3 Self Diffusion Properties

In Fig. 4.2, the temperature dependence of diffusivity, computed from all my AIMD simulations, is compared with experimental values at similar and lower temperatures. Values corrected for finite size effects are also shown here, using methods proposed in Ref.[72]. Confirming previous results,[28] we find that the temperature of AIMD with PBE and BLYP must be 16-20% higher than the experimental one, to give a similar diffusivity. With revPBE, the temperature needs to be only 6-9% higher.

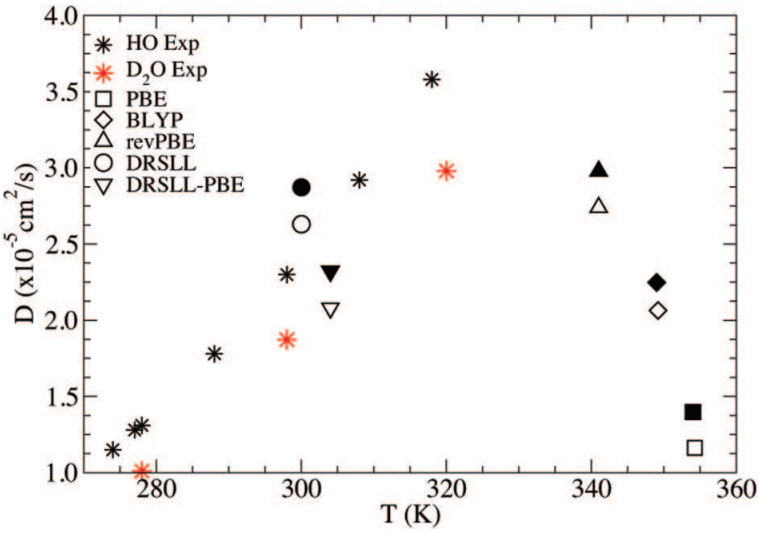

Figure 4.2: Self-diffusion coefficient vs temperature obtained in AIMD simulations with various XC functionals compared to H_2O and D_2O experimental values.[33] Values corrected for finite size effects[72] are shown as solid symbols, and uncorrected values as open symbols. Note that my simulations are performed for D_2O.

On the other hand, both DRSLL and DRSLL-PBE nearly reproduce the experimental diffusivity at room temperature, without any temperature rescal-

ing. This is not unexpected, given the strong link between structure and dynamical properties of liquid water.[28] Thus, one of my most important conclusions is that DRSLL-PBE is a very good XC functional to describe liquid water: PBE requires scaling up the temperature to reach an agreement with experiments. DRSLL replicates diffusivity well, but it substantially fails to describe the RDFs. DRSLL-PBE corrects the structure while maintaining a very good diffusivity.

4.4 Analysis and Discussion

4.4.1 Intermolecular Interactions

Since the vdW attraction of vdW-DFs does not reduce the H-bond distances (actually they increase, relative to their GGA counterparts), what causes the large increase in equilibrium density? One possibility is that the stronger H-bonds, shown in Fig. 4.3(b), increase the average first-neighbor coordination. However, the height of the first peak in $g_{\mathrm{OO}}(r)$, as shown in Figs. 3.3 and 4.1, actually decreases from the GGAs to the vdW-DFs. Therefore, there is left only the third possibility mentioned before, i. e. an increase in the occupation of the 'interstitial', non-H-bonded sites.

In order to characterize the vdW binding between water molecules, I have calculated the interaction energy between two water molecules oriented as shown in Fig. 4.3(a), thus avoiding the hydrogen bond interaction. By comparison, we also use PBE and revPBE. Fig. 4.3(a) clearly shows that DRSLL exhibits a minimum in the potential at $\sim$3.7 Å with a binding energy of 10 meV, not shown by the GGAs. Although this is many times times weaker than the H-bond, it will have an important effect in increasing the occupation of the interstitial sites, which are roughly at that distance. It is worth noting that the position of this potential energy minimum is close to the first minimum of $g_{\mathrm{OO}}(r)$, obtained with the GGAs. This means that this new 'vdW bond', and its effect on increasing the occupation of interstitial sites, may account for the unusual hump appearing in the $g_{\mathrm{OO}}(r)$ of DRSLL at this distance, as seen in Fig. 4.1. The potential energy minimum in DRSLL-PBE is even deeper, 25

meV, and shifted to shorter distances (3.4 Å). This is also the origin of the increase of the height of the first $g_{OO}(r)$ minimum from PBE to DRSLL-PBE.

I have also computed the H-bond potential energy curve between two water molecules in a H-bond configuration. The results are shown in Fig. 4.3(b). The depth of the potential is lower that the optimal H-bond interaction energy because the geometry of the molecules was not optimized. Still the results show the same tendency observed in the RDF and in Table 4.1. When the vdW functional is included, the energy of the H-bond interaction increases by approximately 25 meV independently of the GGA used to describe the exchange interaction. Therefore, the weakening of the H-bond network by vdW interactions (reduction of the first and second coordination peaks) is not associated to the weakening of the H-bond itself, but to the increase of new, favorable, non H-bonded configurations that compete with the H-bonds.

4.4.2 Spatial Distribution Functions

RDFs give angular-integrated information, but the angular distribution of molecules around a given one also contains very valuable information that can differentiate between similar RDFs. In Fig. 4.4 we plot the O-O spatial distributions functions (SDF)[90] $g_{OO}(r, \theta, \phi)$ for three functionals. The polar angles θ, ϕ are referred to a local coordinate set of the central molecule, with origin at the oxygen atom: x (direction of the $\widehat{\mathrm{HOH}}$ angle bisector), y (perpendicular to x, within the molecular plane) and z (normal to the molecular plane). We plot isosurfaces $g_{OO}(r, \theta, \phi) = g_c$, restricted to spherical shells of thickness $\delta r = 0.2$ Å centered at three different distances r: *i*) at the first maximum of $g_{OO}(r)$, with $g_c = 2$, Figs. 4.4(a-c); *ii*) at the first minimum of $g_{OO}(r)$, with $g_c = 0.5$, Figs. 4.4(d-f); and *iii*) at the second maximum of $g_{OO}(r)$, with $g_c = 1$, Figs. 4.4(g-i). To ease the visualization we show three different viewpoints (front, top and side) for each shell.

Fig. 4.4 compares the O-O SDF of PBE, DRSLL, and DRSLL-PBE water at 1.0 g/cm^3. RevPBE is omitted because of its close similarity to PBE. The structure of the first maximum is almost identical for all the functionals considered, i.e, nearly tetrahedral. The density of acceptor molecules (lobes

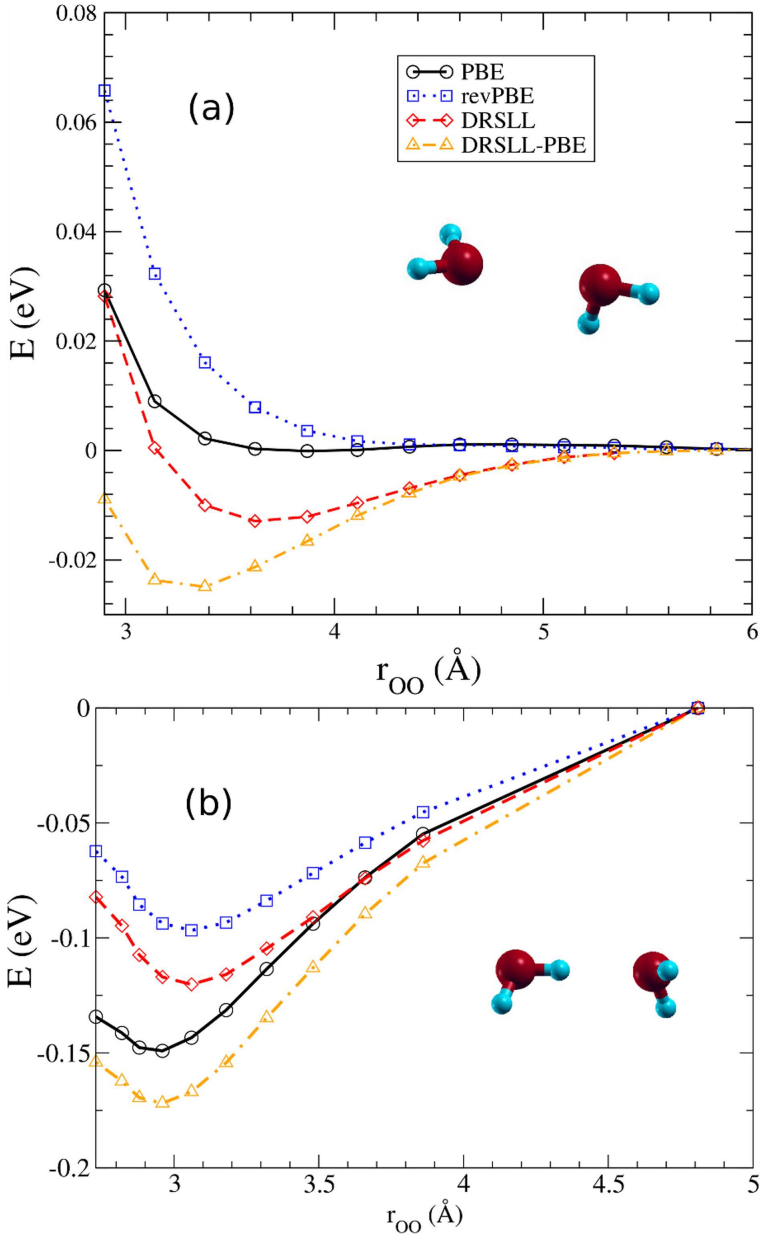

Figure 4.3: Total energy of the water dimer as a function of the intermolecular separation for two different molecular orientations calculated for PBE (circles), revPBE (squares), DRSLL (diamonds) and DRSLL-PBE (triangles). (a): Non H-bonded configuration as shown in the inset (with partially facing O lone pairs from each molecule). (b): H-bonded configuration as shown in the inset. In both graphs the energies have been shifted to have the zero at the largest separation.

in front of the H atoms) is much more localized than the density of donor molecules (lobes in the region of the oxygen lone pairs behind the oxygen atom) which is more disperse. This dispersion reflects the asymmetry of the H bonds, which are less directional on the accepting molecule.

The most important differences between the vdW and GGA functionals occur beyond this tetrahedral shell, at the distance of the first minimum of $g_{OO}(r)$ (Figs. 4.4(d-f)). At this distance, the angular distribution for the PBE functional has small lobes in the tetrahedral directions and larger ones in the opposite directions, that we will refer as anti-tetrahedral.[91] The small tetrahedral lobes correspond to the tail of the first coordination peak. The anti-tetrahedral lobes correspond to the directions of the interstitial sites, and it is fully dominant in the vdW-DFs (Figs. 4.4(e-f)). Thus, although this anti-tetrahedral shell is already present with the GGA due to entropic effects, its density significantly increases in the vdW-DF due to the vdW attraction. Soper et al.[91] observed a similar effect in liquid water under pressure. Thus, the effect of non local vdW correlations in DFT water is similar to the effect of pressure in experimental water.

The third shell shown in Figs. 4.4(g-i), corresponds to the position of the second coordination shell, at $r \sim 4.4$ Å. This peak, formed by second neighbors, tetrahedrally coordinated to the first coordination shell, is depleted in vdW water in favor of the interstitial anti-tetrahedral shell.

One can conclude from this analysis that the effect of vdW-DF correlation is to increase the density of the liquid by populating the interstitial sites that are at a distance between the first and second coordination shells. These interstitial structures become more favorable because of non-H-bonded vdW interactions, as shown in Fig. 4.3(a), and they compete with, and destabilize, the H-bond network. They also increase the height of the first minimum in $g_{OO}(r)$, that is too low with PBE. On the other hand, revPBE water is already relatively unstructured, H-bonds being rather weak for this functional, as shown in Table 4.1. Therefore the density increase induced by vdW interactions, combined with a weak H-bond network, results in a collapse of the structure, characteristic of water under pressure.

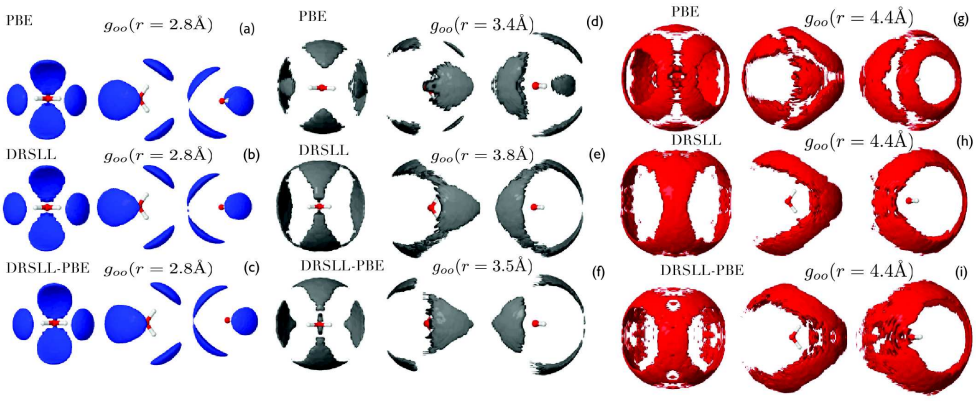

Figure 4.4: Spatial distribution function(SDF) of liquid water, from 3 viewpoints (front,top and side) and for 3 different shell radii as indicated in the legend: (a) PBE, first coordination shell, (b) DRSLL, first coordination shell, (c) DRSLL-PBE, first coordination shell, (d) PBE, interstitial shell, (e) DRSLL, interstitial shell, (f) DRSLL-PBE, interstitial shell, (g) PBE, second coordination shell, (h) DRSLL, second coordination shell, and (i) DRSLL-PBE, second coordination shell.

4.4.3 Hydrogen Bond Network

In previous sections I did not explicitly analyze the hydrogen bond network. In water, each molecule tends to be surrounded by others, donating two H-bonds and receiving two others in a nearly tetrahedral arrangement. This translates into a H-bond network with a majority of four-coordinated molecules. However it also contains under-coordinated and over-coordinated molecules, and the population of under-coordinated molecules correlates with an increasing self diffusion constant. The average bond life-time of the H-bonds in liquid water is of the order of 1 ps. [92]

One of the most striking differences between the GGA functionals and their vdW-DF counterparts is the large change observed in the first peak of the O-O RDF. In average, this implies both a reduced number of H-bonds and longer H-bond lengths when vdW interactions are accounted for. This however does not correlate with the average H-bond energies and geometries presented in table 4.1. The table shows that vdW interactions increase the

H-bond energy by ∼25 meV, both for revPBE and PBE. This is close to the vdW (non-H-bond) binding energy shown in Fig. 4.3(a). Also, the right shift of the O-O RDF peak (2.5%) is much larger than the increase in average O-O distances shown in table 4.1 (0.9%). To study the origin of these deviations we have analyzed the statistics and geometries of: (i) H bonds, defined by the molecules that contribute to the first, tetrahedral, shell shown in Fig. 4.4(a-c) and (ii) VdW bonds, or interstitial molecules in anti-tetrahedral coordination to the H-bond network as shown in Fig. 4.4(d-f). The total $g_{OO}(r)$ has been divided in three contributions: first-shell and second shells of H bonds (HB1 and HB2) and a remainder $g_{OO}^{total}(r) - g_{OO}^{HB1}(r) - g_{OO}^{HB2}(r)$.

To explore further this relationship, I show in Fig. 4.5 the difference between GGA and vdW g_{OO}(r) RDFs. This difference gives the excess density, as seen from a molecular center. Three features are relevant in this graph. First one can observe a large, negative peak at $\sim$ 2.7 Å . This is followed by a maximum at $\sim$ 3.1 Å . These two features are due to the right shift of the first coordination peak in vdW-DFs, with respect to the corresponding GGAs. Third, we also observe a hump at $\sim$ 3.4 Å for DRSLL-PBE and at $\sim$ 3.8 Å for DRSLL, that occurs exactly at the positions of the vdW potential minima shown in Fig. 4.3(a) and marked by arrows in Fig. 4.5.

Results are shown in Fig. 4.6 and Table 4.2 for PBE and DRSLL-PBE[93]. VdW correlations produce slightly fewer H-bonds per molecule (3.78 vs 3.81) with a broader distribution of lengths. The second shell of H-bonds, represents $\sim$ 60% of the second peak in the RDF. Again, there are slightly fewer second shell H-bonded molecules with DRSLL-PBE (10.47 vs 10.59). These numbers are very close to the ideal 'mean-field' value $N_{HB2} = N_{HB1}(N_{HB1} - 1)$. The bottom plot in Fig. 4.6 represents all the neighbors not included in the previous two distributions. These include the third shell of H-bonds and the vdW-bonded molecules (these two are not mutually exclusive). We see an important 20% increase in DRSLL-PBE, up to a distance of 4.5 Å, a region in which non-H-bonded interstitial molecules are dominant. This increase is about twice as large from revPBE to DRSLL[93]. Notice that the maximum of this distribution for DRSLL-PBE, at 3.5 Å, coincides approximately with the position of the vdW energy minimum of Fig. 4.3, and also with the first mini-

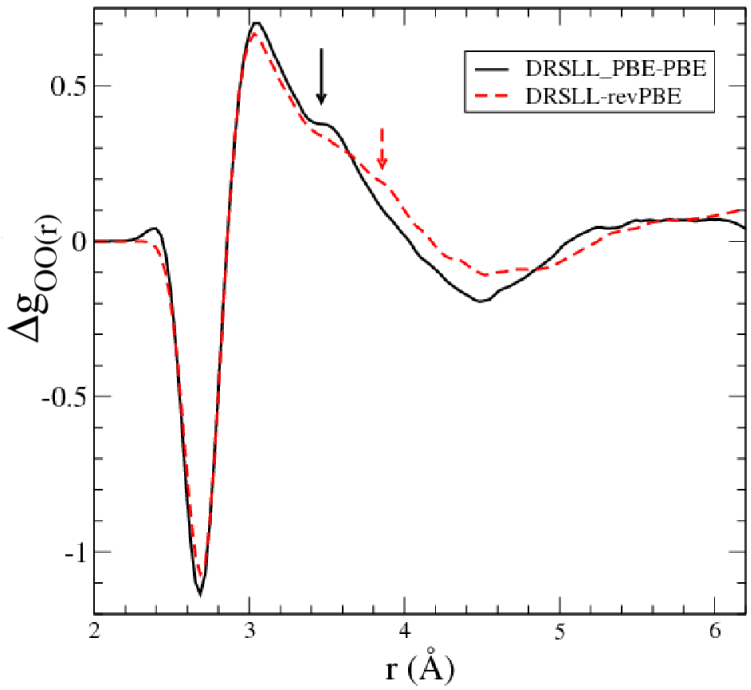

Figure 4.5: The difference between GGA and vdW $g_{OO}(r)$ RDFs ($\delta g_{OO}(r)$), defined as $g_{OO}^{vdW}(r)$-$g_{OO}^{GGA}(r)$ for DRSLL ($\rho = 1.0$ g/cm^3) compared to revPBE ($\rho = 0.95$ g/cm^3), red dotted lines and DRSLL-PBE ($\rho = 1.0$ g/cm^3) compared to PBE ($\rho = 0.95$ g/cm^3), black line. The arrows indicate the position of the energy minima in Fig. 4.3(a).

mum of the total $g_{OO}(r)$. One can also observe a positive correlation between the number of non-H-bonded neighbors of a molecule and its average H-bond distances. This produces a 1.7% right shift of the average O-O distance for the first H-bonded shell from PBE to DRSLL-PBE, due to the increase of vdW bonds. A more detailed analysis of this, and other related effects, needs further investigation in the future.

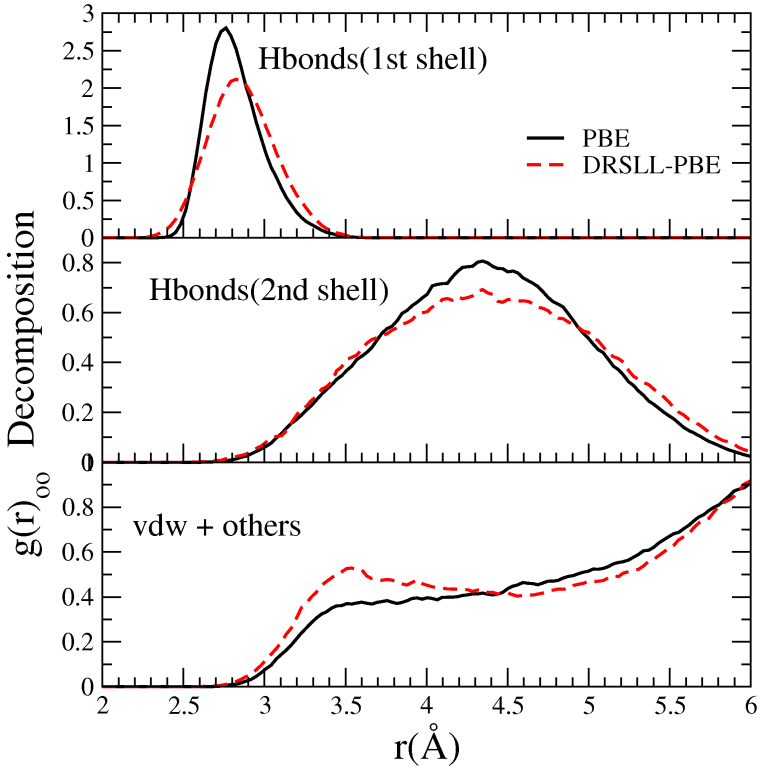

Figure 4.6: Decomposition of $g_{OO}(r)$ into H and vdW bonds. Top, tetrahedral shell of first H-bonded neighbors, shown in Fig. 4.4(a-c). Center, second H-bonded shell shown in Fig. 4.4(g-h). Bottom, remaining molecules which include vdW-bonded, interstitial and third shell H-bonded molecules. The maximum of the lower DRSLL-PBE curve, at r=3.5Å, is due to the molecules in anti-tetrahedral coordination to the H-bond network, as shown in Fig. 4.4(d-f). Simulations in this figure are for liquid water at 1.0 g/cm^3 and ∼300 K.

To study the distribution of H-bonds in simulations I use the following requirements to define a H-bond: i) the O-O distance must be shorter than that

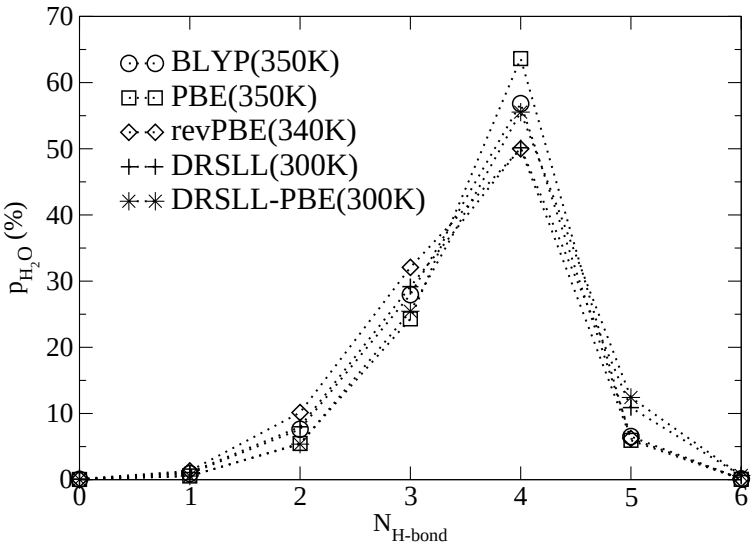

Figure 4.7: Distribution of the population of H-bonds per central molecule ($N_{\mathrm{H-bonds}}$) for all the XC functionals in this study. $P_{\mathrm{H_2O}}$ is the percentage of water molecules that have $N_{\mathrm{H-bonds}}$. All simulations in this graph are performed for liquid water at a density of 0.95 g/cm^3 except for DRSLL and DRSLL-PBE, which are at 1.0 g/cm^3. Their effective temperatures are all close to 300 K.

Table 4.2: Mean values for H and vdW bonds at 1.0 g/cm^3 and ∼300 K. N_{HB1} and N_{HB2}: average number of H-bonded molecules in the first and second coordination shells (integral of first two curves in Fig. 4.6). N_{vdW}: average number of non-H-bonded molecules (vdW-bonded and others) in a sphere of 4.5 Å radius. r_{HB1}: average O-O distance for first H-bonded shell.

Functional	N_{HB1}	N_{HB2}	N_{vdW}	r_{HB1} (Å)
PBE	3.81	10.59	3.25	2.847
DRSLL-PBE	3.78	10.47	3.89	2.895

of the first minimum of $g_{OO}(r)$,[24] and *ii*) the $\widehat{OOH}$ angle (with the central oxygen in the donor molecule) must be smaller than an arbitrary maximum value[24] of 45°.

Fig. 4.7 shows the distribution of H-bonds per central molecule at a density of 0.95 g/cm^3 (except DRSLL and DRSLL-PBE, which are at 1.0 g/cm^3). PBE gives the smallest number of under-coordinated H-bond defects, and revPBE gives the largest, indicating that PBE favors the formation of strong H-bonds. In both cases of DRSLL-PBE and DRSLL, the population of vdW-DF is lower than corresponding GGA, probably because the energy of the competing vdW-bond (Fig. 4.3(a)) is stronger in vdW-DF functional. In either case, the main change introduced by vdW interactions is the decrease of under-coordinated or tetra-coordinated molecules in favor of over-coordinated defects. Overall the number of H-bonds remains the same.

4.5 Conclusion

A summary of the effect of non-local dispersion van der Waals interaction on the simulations for liquid water is as follows:

- The net effect of vdW non-local correlations is to reduce the pressure and to increase the equilibrium density, which is just 2% larger than experiments with DRSLL and 13% higher with DRSLL-PBE. With vdW interactions, non-H-bonded water-water configurations are introduced, due to the occupation of interstitial sites. These configurations have an anti-tetrahedral orientation, opposite to H-bonds, and they contribute

to increase the height of the first minimum in $g_{OO}(r)$.

- While the interstitial sites are partially occupied due to entropy in GGA water, their population increases greatly when the vdW attraction is added. The use of angular-resolved spatial distribution functions is necessary to understand the overall structural changes. These anti-tetrahedral structures are the key factor to increase the self diffusion of AIMD water. The diffusivity obtained with DRSLL is very close to experiment at room temperature, without the need of temperature rescaling.

- DRSLL water is under-structured when compared to experiments, with a significant collapse of the second coordination shell induced by the increased density. This is related to the use of revPBE as local exchange, which produces too weak H-bonds. The combination of non local vdW correlation, as in DRSLL, combined with PBE exchange, produces a better liquid, with structural and dynamical properties not far from experiments, without the need of any temperature rescaling. However PBE H-bonds are too strong and DRSLL-PBE causes an over correction of the density with respect to PBE.

- A better treatment of the exchange interaction should improve the H-bond description and, together with vdW correlations, might end up providing the final overall agreement with experimental results in terms of structure, density, and diffusivity of liquid water. A modification of the vdW density functional has been proposed very recently,[89] and a brief study of this flavor of vdW functional shows very similar high density liquid structure as the DRSLL density functional. Future modification to the density functional can be improved to soften the liquid, as the bulk modulus calculated from Fig. 3.10 is too large compared with GGA results and even larger if compared with experimental value. At the same time, inclusion of nucleus quantum effect could further soften the overall system and thus results in smaller value of the bulk modulus.

In this chapter, a detailed study of van der Waals interaction on liquid water is presented. It is shown that the increased density with van der Waals density functional is due to the VdW type of bond which leads to increased population of interstitial shell between first and second coordination shell. By reference to the ice crystal structure, this interstitial shell is identified to be anti-tetrahedral structure, which is driven by entropy. At the same time, the overall structure of the hydrogen bond is significantly affected by VdW bond, populating more molecules in anti-tetrahedral shell which in turn results in a significant increase in self-diffusivity. However, we have also found that the bulk modulus with vdW density functional is almost 3 times larger than corresponding GGA ones and almost 5 times more than experiments. The reason for this underestimation of the compressibility of liquid water is still not clear. A good exchange and correlation functional may be helpful and nuclear quantum effects can also increase the compressibility. Here the question is proposed and future work can be done to solve this problem.

So far I have presented a first principles study of pure water. A parallel project on the application of first principles study of liquid water at a semiconductor interface was also investigated in detail. This accounts for the rest of my thesis and will be presented in the next chapter.

Chapter 5

AIMD Study of GaN/aqueous Interface

GaN is an important semiconductor material. Its wide band gap of 3.4 eV makes it ideal for applications in optoelectronic, high-power and high-frequency devices. For example, GaN is the substrate which makes violet (405 nm) laser diodes possible, without use of nonlinear optical frequency-doubling. The main phase of GaN is the wurtzite structure and can be found in many forms such as bulk, film and nano cluster. In 2006, Domen et al, [97] discovered that the GaN/ZnO semiconductor alloy solid solution can function as a photocatalyst for the water splitting reaction, with cocatalyst needed for reducing electrons. The overall reaction is found to be $2H_2O(l) \rightarrow H_2(g) + O_2(g)$ under visible light. The reaction at semiconductor and aqueous interface is identified to be $2H_2O(l) \rightarrow 4H^+ + O_2$ with the surface of semiconductor work as a photocatalyst and the quantum efficiency for this process is found to be around 50%. Pure GaN is known to be also photocatalytically active but only in the UV region, because the semiconductor band gap is 3.4 eV, outside the visible region of the solar spectrum. However, it serves as an appropriate model system in the absence of details of the complicated alloy structure and surface reconstruction.

The purpose of my work in this chapter is to use the ab initio molecular dynamics simulations and knowledge of simulating liquid water obtained from

previous experience to examine the fully solvated aqueous interface near room temperature. A flat non-polar GaN 10$\underline{1}$0 surface is chosen to be examined due to its stable nature and analogy to structure of other widely studied photocatalyst such as TiO_2. The work in this chapter is actively collaborated within Swassit (The Stony Brook/BNL Solar Water Splitting Simulation Team). Xiao Shen is a former graduate student at Stony Brook University under supervision of Professor Philip B. Allen. He did the part of atomistic modeling and proposed a sequence of intermediate steps for the water oxidation process at a pure GaN/water interface. The cluster model configuration he used to study water oxidation mechanism is cut out from snapshots of AIMD simulations that have been done within this thesis. So in the first section, I will summarize the proposed reaction intermediates which follow a sequence of four proton-coupled electron transfers. Their calculated standard free energies give a full picture of proposed water oxidation mechanism.

In the rest of the sections, the focus is on ab initio molecular dynamics simulations that examine the fully solvated aqueous interface at room temperature. The question addressed here is the nature of water adsorption on GaN 10$\underline{1}$0 surface, including hydrogen bond network of dissociated and non-dissociated water molecules, structural and dynamical properties of water at interface, proton diffusion process and electronic structure of the whole system.

5.1 Water Oxidation Mechanism on GaN 10$\underline{1}$0 Surface

Shen et. al presented a first-principles study of water adsorption on a wurtzite GaN (10$\underline{1}$0) surface[94]. In their work, they answered a focused question: How does a monolayer of water adsorb on the surface of pure GaN? They used a density functional theory (DFT) approach to study the adsorption structures and energetics. They studied different coverages on the surface, with a conclusion that dissociative adsorption energy is around 1-1.5 ev higher than molecular(non-dissociative) adsorption, suggesting a stable structure when water molecules on the surface are dissociated. More importantly, they have also

found that the energy barrier from molecular adsorption to dissociative adsorption is negligible using the nudged elastic band (NEB) method. They suggested that due to this negligible energy barrier, the ground-state of a water monolayer on GaN (10$\underline{1}$0) is the completely dissociative state. This is quite interesting because ZnO 10$\underline{1}$0 non-polar surface tends to have a lower dissociative adsorption energy and thus only around 50% of the water molecules are dissociated. GaN tends to have a stronger covalent bond and dangling bond at the surface and thus dissociates water molecules more easily.

Following the study of a monolayer of water on GaN (10$\underline{1}$0) surface, I performed ab initio molecular dynamics simulations of the GaN (10$\underline{1}$0)-aqueous interface in a slab geometry without initial water dissociation events. One of the purposes of this study is to find feasible surface structures after full solvation and use these structures as the starting points for a detailed cluster model study to find the likely water oxidation mechanism. The details of the ab initio molecular dynamics simulations of this system will be presented in more detail later in this chapter; here I concentrate on its connection with the photocatalytic water oxidation mechanism. From AIMD simulations, it has been found that almost 80% of water on top of the GaN 10$\underline{1}$0 surface will be dissociated within 1 ps, confirming Shen's main conclusion in ref[94]. Among all the dissociated water molecules, the majority of OH^-s that bonded to a Ga dangling bond on the surface are forming pairs through hydrogen bonds between other surface bonded OH^-s. These are analogous to water dimers with Ga atom replacing one proton. Those OH^- dimers are formed under the constraint of the distance between surface Ga atoms because of GaN wurtzite crystal structure. An important observation is that the hydrogen bond (HB) network of the fully solvated surface is disrupted compared to the monolayer structure, with around 50% of the hydroxide ions making HBs to molecules in the bulk liquid region. The assignment of ionic adsorbates is consistent with this very small, early energy barrier to the dissociation of a water molecule on the GaN(10$\underline{1}$0) surface, reflecting the long-range attraction of the incipient dissociated species with the Ga and N surface sites compensating for the large amount of energy required to stretch the HOH bond. The stability of the dissociated waters bonded to the interface, together with the relatively

ordered and rigid HB structure of interfacial waters, allows us confidence in selecting snapshots from our calculations to build models of solvated clusters (see Figure 5.1 as in [95] Figure 2).

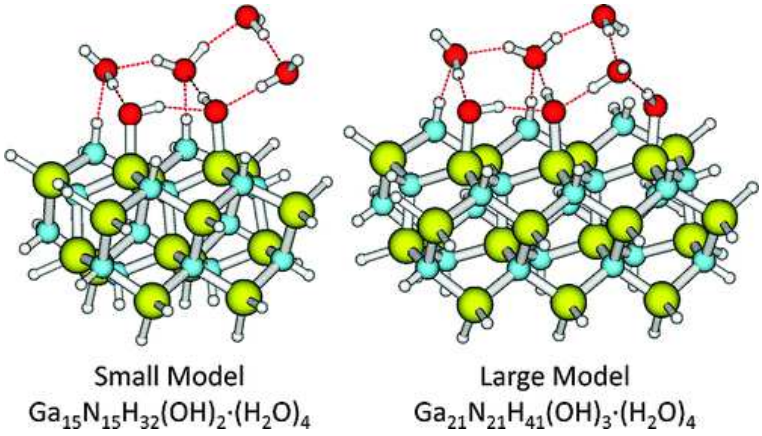

Figure 5.1: Optimized structures of the resting state of the small and large cluster models employed by Shen et al.[95] Both models include four explicit solvent water molecules in addition to the two (in the smaller) or three (in the larger) dissociated water molecules on the surface of the clusters. [95]

After a characteristic initial configuration is identified, a cluster model using DFT theory is chosen to probe the structure of the solvated interface and react on intermediates. Reaction intermediates connected by proton-coupled electron transfers are identified and the Gibbs free energy of each intermediate in aqueous solution is also computed. A summary of all intermediates in the proton-coupled electron transfer process, and reduction potentials for the proposed reaction steps are shown in Fig. 5.2(a) and 5.2(b).[95]

In summary, AIMD simulations showed a non polar GaN $10\underline{1}0$ surface with 83% surface sites bound to dissociated water molecules, with no vacant Ga sites. A cluster model was constructed in which the initial states conformed to the states of full water dissociation on available surface Ga and N sites extracted from AIMD simulation structure. A possible sequence of reaction intermediates for water oxidation at a specific interface using a solvated cluster model approach was carried out by Shen et al[95].

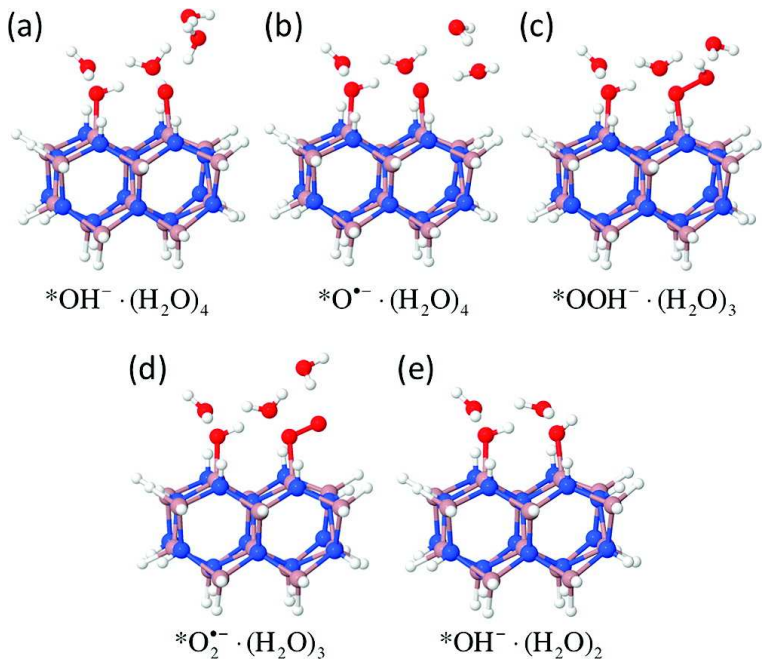

(a)

step	reaction on a GaN Surface	E^o(V)
(1)	$*O^{\bullet -} + e^- + H^+ \rightarrow *OH^-$	2.56
(2)	$*OOH^- + e^- + H^+ \rightarrow *O^{\bullet -} + H_2O$	0.99
(3)	$*O_2^{\bullet -} + e^- + H^+ \rightarrow *OOH^-$	1.01
(4)	$*OH^- + O_2 + e^- + H^+ \rightarrow *O_2^{\bullet -} + H_2O$	−0.11
(1)+(2)	$*OOH^- + 2e^- + 2H^+ \rightarrow *OH^- + H_2O$	1.77
(3)+(4)	$O_2 + *OH^- + 2e^- + 2H^+ \rightarrow *OOH^- + H_2O$	0.45

(b)

Figure 5.2: A summary of all intermediates in the proton-coupled electron transfer process and reduction potential for proposed reaction steps.[95] 5.2(a):Relaxed structures of the intermediates for the small cluster model: Ga (brown), N (blue), O (red), and H (white). 5.2(b): Calculated standard one- and two-electron reduction potentials for proposed reaction steps with the small cluster model at the GaN/Aqueous interface, and measured potentials for the corresponding reactions in aqueous solution.[95]

5.2 First Principles Study of GaN(10$\underline{1}$0)/Aqueous Interface

5.2.1 Introduction

GaN:ZnO alloy semiconductors have been shown to be promising materials to serve as the photo-anode in photocatalytical water-splitting devices[97]. The microscopic details explaining origin of their high quantum efficiency ($\approx 51\%$ in the 420-440 nm photon wavelength range) to oxidize water in the presence of a sacrificial electron scavenger were proposed in the previous section. Two physical reasons are suggested here to be major contributors to the high photocatalytic oxidation activity of this alloy. The first one is its optimal band gap. As shown by Domen[97, 98] and subsequently studied by others, both theoretically[94, 111] and experimentally[112], the the GaN:ZnO solid solution absorbs light in the visible, while the optical activity of the two pure semiconductor counterparts only begins in the UV range. The second one is associated to the suitability of the conduction band edge (CBE) and valence band edge (VBE) potentials of the alloy for the overall water splitting reaction[113]. In GaN the VBE formed by N 2p states[94, 98] is located below the water oxidation potential[98], while the CBE, formed by hybridized Ga 4s and 4p orbitals, is located above the water reduction potential. The activity of the solid solution as an overall water splitting material, despite the reduction in band gap, indicates that this band alignment with respect the water redox potentials is maintained.

There is a third question regarding the efficiency of a photocalayst that has not been analyzed in detail to date. This is the importance of spontaneous water dissociation, $H_2O \rightarrow H^+ + OH^-$, at the surface of the semiconductor photocatalyst. One of the most studied photocalysts, TiO_2 is only active in the UV range of the solar spectrum. Many experimental and theoretical studies have shown that photoactive TiO_2 surfaces do not dissociate water. The non polar GaN(10$\underline{1}$0) surface has been shown to spontaneously dissociate water[94, 95]. The same surface in ZnO only achieves a 50% dissociation of the molecules adsorbed at the surface[110].

The previous sections outlines Shen *et al.*'s[95] proposed a sequence of intermediate steps for the water oxidation process at this particular GaN/water interface. The reaction intermediates follow a sequence of four proton-coupled electron transfers and they require that water dissociates at the surface to start with. The question of how the efficiency of a photocatalyst correlates with the H_2O dissociative potential of the surface, and how dissociated species interact with other water molecules at the interface is yet to be addressed. In this contribution we analyze the dynamics of water dissociation at the GaN(10$\underline{1}$0). The work is an extension to the preliminary results presented by Shen *et al*[95]. Here we present a thorough analysis of the changes in structure and dynamics of water interacting with a dissociating surface. We also present a detailed technical analysis of the method and show how the surface dissociation potential is strongly dependent on the valence charge of the Ga atom.

5.2.2 Methodology

Ab initio molecular dynamics simulation is performed for a GaN (10$\underline{1}$0) surface slab hydrated by 94 D_2O molecules, with a geometry as shown in Fig. 5.3. Density functional theory, with the PBE generalized gradient approximation (GGA) exchange and correlation functional[48] are used. Core electrons were replaced by norm-conserving pseudopotentials [56] in their fully nonlocal representation.[57] The Kohn-Sham eigenstates are expressed as linear combination of atomic orbitals as employed in the SIESTA program.[58, 59] The calculation of the self-consistent Hamiltonian and overlap matrices was done using the SIESTA method[58, 59]. In this study, a double-ζ polarized (DZP) basis set was used, which has been variationally optimized following the method proposed in Refs. [60, 61]. The validation of the method, pseudopotentials and basis set can be found in Ref. [28]. The quality of the DZP basis for describing water should not be underestimated, given good description of the H-bond geometry and the structure of liquid water.[28] The simulations of liquid water shows that the difference between the TZP and DZP energies is an almost constant value of 0.12 eV/molecule, with a standard deviation of only 7 mev, which can be neglected.[96]

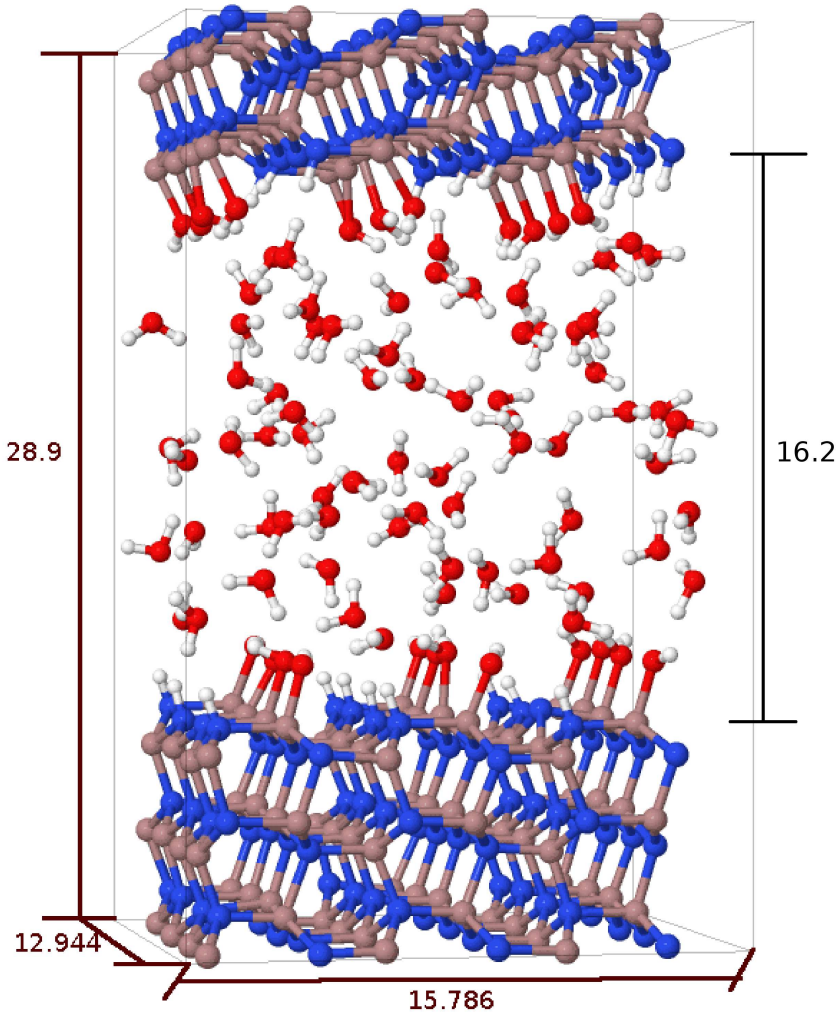

Figure 5.3: Fully solvated GaN slab 10$\underline{1}$0 wet surface. Periodic repetitions of a 5 double layers slab(4×3×5 GaN units) are separated by 16.2 Å of vacuum with unit cell dimension as 12.944Å × 15.786Å × 28.9Å . 94 water molecules are accommodated in the vacuum. After full solvation, 20 of 24 possible GaN surface sites dissociate water molecules, and the remaining 4 Ga sites are occupied by undissociated water molecules. Ga is in brown, N is in blue, O is in red, and H is in white.

The Ga pseudopotentials must be carefully generated since Ga 3d states resonance with N 2s states and thus cation d bands are not inert. The role of 3d electrons on the structural and electronic properties of GaN has been studied before as in Ref.[99, 100] The 3d electrons can be either treated as valence electrons or semi-core electrons. The semi-core electrons repulsion interaction has a noticeable effect on the cohesive properties and energetic band structure of GaN.[99] The lattice parameters of zinc-blend GaN with Ga 3d valence electrons was reported to be about 3% larger.[99]

In this work, we studied the role of 3d electrons on wurtzite GaN structural and energetic properties. Due to the well known core-valence exchange-correlation non-linearity problem, a non-local core correction (NLCC) is made for Ga pseudopotentials. In the pseudopotential generating process, the Ga 4s orbital radius cutoff is set to be 2.1 Å and Ga 4p orbital radius cutoff is set to be 2.5 Å . The other two most important parameters in generating Ga pseudopotentials with 3d valence electrons are the 3d orbital cutoff radius (r_{c-3d}) and NLCC cutoff radius(r_{c-NLCC}). A series of simulations of wurtzite GaN with 9 different Ga pseudopotentials are performed with different parameters (3d orbital cutoff radius: r_{c-3d} and NLCC cutoff radius: r_{c-NLCC}) to generate pseudopotentials. Their corresponding structural properties are shown in Table 5.1. Also, a simulation using a Ga pseudopotential without 3d valence electrons is performed and the GaN bulk properties from it is also shown in Table 5.1.

The structural and energetic properties such as lattice parameters, unit cell energy and band Gap energy from simulations with a series of different Ga pseudopotentials are shown in Table 5.1. In general, Table 5.1 shows the expansion of cohesive properties such as lattice parameters due to the semi-core electrons repulsion effect of 3d electrons. Comparing with experiment[107] values: a=3.188 Å and c/a=1.6267, plane wave DFT results already shows 1% overestimation of lattice parameters with a=3.219Å and c/a=1.6287.[94] The choice of r_{c-3d} and r_{c-NLCC} is somewhat arbitrary. We choose three Ga pseudopotentials that show the overall best agreement between experimental and plane wave results of lattice parameters. The parameters used to generate these three pseudopotentials are: 1. r_{c-3d}=0.5 Å and r_{c-NLCC}=1.0 Å 2.

r_{c-3d}=1.0 Å and r_{c-NLCC}=1.0 Å and 3. r_{c-3d}=1.5 Å and r_{c-NLCC}=1.0 Å . These pseudopotentials are further studied and compared to give the overall best performance on surface energetic and geometric properties. The three pseudopotentials chosen are named after Ga^{3d2}, Ga^{3d5} and Ga^{3d8}, respectively.

Table 5.1: Calculated structural and energetic properties for GaN in the wurtzite structure from a series of simulations of wurtzite GaN with 9 different Ga pseudopotentials with 3d valence electrons and one without 3d charge. r_{c-3d} is the cutoff radius of Ga 3d orbital and r_{c-NLCC} is the cutoff radius of NLCC(non local core correction). a is the short lattice parameter of wurtzite GaN, c/a is the ratio of c axis lattice constant over a axis lattice constant, E_g is the band gap and E_0 is the total energy per GaN unit cell. Experimental lattice constant a is equal to 3.188 Å , long/short lattice constant ratio c/a is equal to 1.6267 and band gap Eg is equal to 3.44 ev [107] at the room temperature. Compared with experiments, the plane wave DFT results show 1% overestimation of lattice parameters with a=3.219Å and c/a=1.6287.[94]

r_{c3d} (Å)	r_{NLCC} (Å)	a(Å)	c/a	E_g(ev)	E_0(ev)	Label
0.5	0.4	3.296	1.607	1.88	-5587.8	Ga^{3d1}
0.5	1.0	3.236	1.628	1.87	-5501.2	Ga^{3d2}
0.5	1.6	3.225	1.637	1.72	-5071.2	Ga^{3d3}
1.0	0.4	3.243	1.633	1.81	-5525.3	Ga^{3d4}
1.0	1.0	3.236	1.627	1.89	-5439.6	Ga^{3d5}
1.0	1.6	3.236	1.629	1.89	-5011.1	Ga^{3d6}
1.5	0.4	3.265	1.626	1.62	-5319.3	Ga^{3d7}
1.5	1.0	3.252	1.629	1.72	-5231.4	Ga^{3d8}
1.5	1.6	3.252	1.628	1.72	-4808.0	Ga^{3d9}
-	-	3.231	1.624	2.18	-1102.7	Ga^{no3d}

So far we have studied the Ga pseudopotentials effects on the bulk wurtzite GaN. Because our main purpose of studying Ga pseudopotential is to find a good approximation to represent the core electrons screening effect to study the chemical and electronic properties near the GaN wurtzite $10\underline{1}0$ surface, it is important to further study how different Ga pseudopotentials affect the surface energy and water dissociation at the surface. Shen *et al.*[94] have studied the adsorption of monolayer of water at the GaN($10\underline{1}0$) surface. We have done a series of simulations using three Ga pseudopotentials chosen above to calculate surface energies of GaN wurtzite $10\underline{1}0$ surface and adsorption

energy of a monolayer of water on it. The results are compared with plane wave results and are shown in Table. 5.2.

Table 5.2: Calculated surface energy(E_{sur}) of GaN wurtzite 10$\underline{1}$0 surface, adsorption energy(E_{ad}) of monolayer of water on it, and surface Ga-O bond length(r_{Ga-O}) formed by Ga cations and dissociated ions OH^-. The adsorption energy $E_{ad} = E_{slab} + E_{water} - E_{total}$ is the energy released from water adsorption, where E_{slab} is the total energy of the relaxed bare slab and E_{water} is the total energy of a relaxed water molecule. Three Ga pseudopotentials with valence 3d electrons are used; they are Ga^{3d2}, Ga^{3d5} and Ga^{3d8} as shown in Table. 5.1. Another Ga pseudopotential without 3d electrons is also used (Ga^{no3d} in Table. 5.1). The corresponding surface and water adsorption energy from plane wave basis simulations using GGA exchange and correlation approximation (PW-GGA) are as shown in [94].

	Ga^{3d2}	Ga^{3d5}	Ga^{3d8}	Ga^{no3d}	PW-GGA
E_{ads}	2.06	2.09	2.09	2.26	2.18
E_{sur}	1.46	1.86	1.91	2.05	1.60
r_{Ga-O}	1.888	1.875	1.874	1.858	1.845

Table 5.2 shows that GaN wurtzite 10$\underline{1}$0 surface energy and monolayer water adsorption energies on that surface are substantially affected by Ga pseudopotentials. Due to the semi-core repulsion effect introduced by 3d valence electrons, the adsorption and surface energy differences with Ga 3d valence electrons are ≈10%. This indicates that the surface Ga-O bond is more affected by the choice of Ga pseudopotentials than Ga-N bond in bulk wurtzite structure. Comparing our simulation results with corresponding results from plane wave basis simulations shown in [94] and [108], we believe Ga^{3d5} is the best Ga pseudopotentials to describe GaN wurtzite 10$\underline{1}$0 surface and surface Ga-O bond after water adsorption. Together with GaN wurtzite cohesive properties as shown in Table 5.1, we chose Ga^{3d5} to be the Ga pseudopotential with 3d valence electrons in our simulations.

So far we have studied the role of 3d valence electrons of Ga for both bulk wurtzite GaN and 10$\underline{1}$0 surface water adsorption. The semi-core electrons repulsion causes surface Ga-O bond to be 10% weaker. As shown in Table 5.2 and Table 5.1, we are able to reproduce the absorption energies and geometries of the fully dissociated water monolayer on the surface described by Shen *et*

al.[94] with less than less than 0.3% errors in terms of lattice parameters and less than 7% error in terms of surface adsorption energies.

In order to see the effect of the choice of Ga pseudopotentials on water dissociation speed, two AIMD simulations are performed in this study using different Ga pseudopotentials Ga^{3d5} and Ga^{no3d}. We used a slab geometry of 5-layer($4 \times 3 \times 5$) GaN units separated by 16.2 Å of vacuum with total 24 surface GaN sites available to adsorb water. In the first simulation run, we used pseudopotential Ga^{no3d} for all Ga atoms. In the second simulation run, we replaced the pseudopotential of 48 Ga atoms within the surface double layer with Ga^{3d5} while still using Ga^{no3d} for the rest Ga atoms as "bulk". There are 94 water molecules to be inserted in the vacuum region of the cell. The density of bulk water is between 0.97 and 1.00 g/cm3. Because of the periodic boundary conditions, both the top and bottom GaN $(10\underline{1}0)$ surfaces in the slab are wet, and therefore a total of 24 GaN units are capable of dissociating water. To obtain an initial structure for the water layer, we cut a box of 94 water molecules with the appropriate geometry from a previous AIMD simulation of pure liquid water with 128 molecules. The system was equilibrated at a temperature of 340 K using a Nose thermostat for 2 ps, with a time step of 0.5 fs. This choice of temperature ensures the simulation of a liquid state of water, following the temperature rescaling recipe given in [28]. After the equilibration, the AIMD simulation was continued within a microcanonical (NVE) ensemble using a Verlet integrator. A total of 10 ps were used to obtain statistics of the structural and dynamical properties of the fully solvated GaN interface.

Fig. 5.4 shows the evolution of the formation of surface bonds within the first 1.5 ps. The three types of surface bonds are Ga-OH bonds($n_{Ga\text{-}OH}$), Ga-Water bonds($n_{Ga\text{-}Water}$) and N-H bonds($n_{N\text{-}H}$). Results from two simulations with two different pseudopotentials of surface Ga atoms(with and without 3d valence electrons) are compared. Water molecules on the GaN$(10\underline{1}0)$ surface are dissociated into ions such as OH^- and H^+. The long-range attraction of the incipient dissociated species with the Ga and N surface sites compensates for the large amount of energy required to stretch the H-OH bond. From Fig. 5.4, we observe that during this time we observed that 20∼21 of the 24 possible

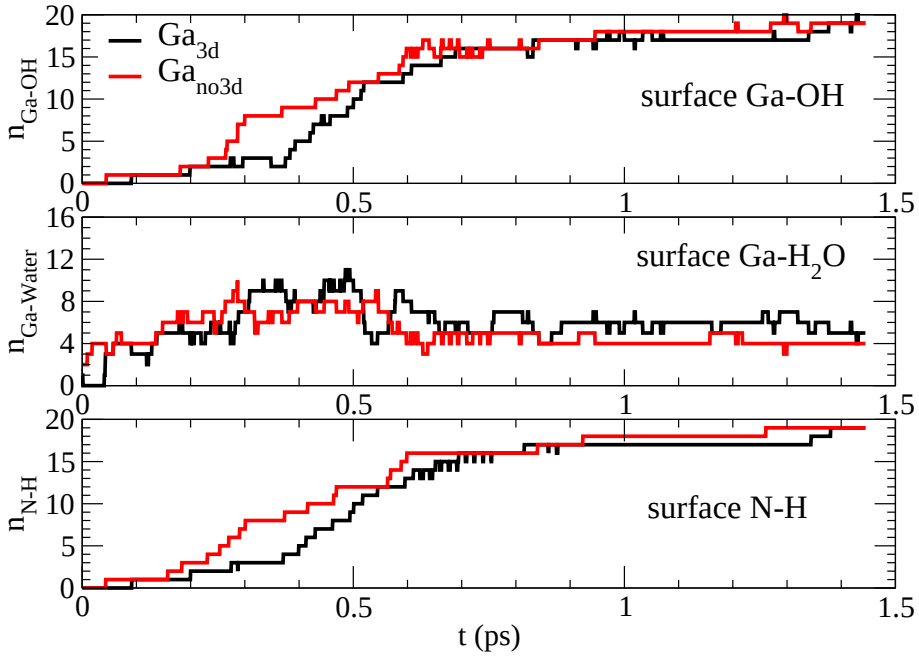

Figure 5.4: The evolution of the formation of surface chemical bonds for the equilibration process with two AIMD simulations. The red line is the one using Ga pseudopotential with only 4s and 4p valence electrons(Ga^{no3d}) and the black line is the simulation using Ga pseudopotential with 3d valence electrons(Ga^{3d}) chosen as above. Top: The evolution of the total number of surface Ga-OH bonds($n_{Ga\text{-}OH}$). Middle: The evolution of the total number of surface Ga-Water bonds($n_{Ga\text{-}Water}$). Bottom: The evolution of the total number of surface N-H bonds($n_{N\text{-}H}$).

GaN surface sites (83%) dissociate water molecules. The remaining 3∼4 Ga sites (17%) are occupied by undissociated water molecules. The dissociation events are very fast, happening in the first 1.5 ps of simulation, confirming Shen et al's previous finding which showed a tiny energy barrier for dissociation at this surface for a monolayer of water.[94]

The surface bonds studied in Fig. 5.4 are characterized by specific cut-off lengths of bonds considered chemically bonded. Since there are always fluctuations of the chemical bond lengths due to thermal effect or chemical environment, the cutoffs of chemical bonds are determined by the mean length plus two standard deviation from the distribution. The stability of the dissociated waters bonded to the interface should be very high as shown in Fig. 5.4 because the number of N-H bonds is stable after equilibrium. The fluctuation of Ga-O bonds for Ga-OH and Ga-Water bonds in the same figure indicates transformation between those two type of bonds due to proton transfer process that will be shown in later in detail.

Fig. 5.4 shows the speed of dissociation events can be affected by the choice of Ga pseudopotentials. As already shown in Table 5.2, Ga^{3d} and Ga^{no3d} have a 10% difference of adsorption energy for a mono layer of water on the GaN $10\underline{1}0$ surface. The average Ga-OH bond length from simulations using Ga pseudopotential Ga^{3d} and Ga^{no3d} are 1.91 Å and 1.85Å , respectively. Again, Ga pseudopotential with 3d electrons as valence has a 3% to 4% longer Ga-O bonds due to the core repulsion. However, the choice of Ga pseudopotentials would not affect the fact that the energy barrier for dissociation at this surface is very small, and that the full solvation process can be well established within 1.5 ps.

In summary, the role of Ga 3d valence electrons is carefully studied in terms of both bulk GaN wurtzite and $10\underline{1}0$ surface, including Ga-O bonds of surface Ga sites with dissociated water molecules. The neglect of 3d states causes the cohesive properties such as lattice constant to contract about 2% but has a larger effect on surface Ga-O bonds with around 4% reduction of bond length and 10% increase of bond energy. Since GaN $10\underline{1}0$ surface properties are sensitive to a proper treatment of the cation d bands, pseudopotentials including only nonlinear core correction(NLCC) are not sufficient for a description of

the GaN surface, at the DFT level of accuracy with GGA approximation. At the surface, a carefully generated Ga pseudopotential must contain d states to determine the properties of this material.

5.2.3 Solvated Surface

Fig. 5.4 shows that the water dissociation events are very fast on GaN 10$\underline{1}$0 surface, happening in the first 1∼1.5 ps of simulation. An important direct observation (see Figure 5.3) is that the hydrogen bond (Hbond) network of the fully solvated surface is disrupted compared to the monolayer structure, with hydroxide ions OH^-s making H-bonds to molecules in the bulk liquid region. AIMD simulation shows that 80% of hydroxide ions OH^- to be $OH^- \cdots OH^-$ dimers connected by hydrogen bonds as shown in Fig. 5.6. This means that 40% of all hydroxide ions OH^- can be categorized as OH_1^- that donate hydrogen bonds to other hydroxide ions OH^-. Thus an equal number of hydroxide ions OH^- can be categorized as OH_2^- that accept hydrogen bonds from hydroxide ions OH_1^-. The remaining 20% are isolated and do not belong to hydroxide ions dimers on the surface. However, the isolated 20% of hydroxide ions OH^- are found to form pairs with H_2O, the non dissociated water, with H-bonds. The stability of the dissociated waters bonded to the interface, together with the relatively ordered and rigid H-bond structure of hydroxide ions OH^- dimers interacting with interfacial water, allows us confidence in selecting snapshots from our calculations to build two models of solvated clusters in [95], which are all based on $OH^- \cdots OH^-$ dimers.

On the GaN 10$\underline{1}$0 surface, Ga cations are not only bound to hydroxide ion OH^- from dissociated water but also bound to the lone pairs of non-dissociated water molecules. The later is categorized as "molecular adsorption" of water described in [94]. It is mostly due to the mismatch of Ga cations and N anions on the surface, because water dissociation requires attraction from both neighbor cations and anions at the same time to break OH-H covalent bond. So this type of "molecular adsorption" is often due to a water molecule near Ga cation site while missing a neighbor N anion.

Both Ga-OH and Ga-H_2O species interact with bulk water through hy-

drogen bonds. The tetrahedral structure of hydrogen bonds with respect to central O atoms within Ga-OH and Ga-H_2O is broken. To address this, we analyze the hydrogen bond structure as a function of distance to GaN 10$\underline{1}$0 surface. In Fig 5.5, the average total number of hydrogen bonds per molecule within the layers along the direction perpendicular to the GaN 10$\underline{1}$0 surface for different species (continuous solid line) is shown. In particular, we also count the number of H-bond donors(dotted line) and acceptors(dashed line) for each species. We choose the following geometric criterion to define a hydrogen bond: O$\cdots$O distance shorter than 3.5 Å and O$\cdots$H–O angle larger than 140 °. In the top panel, the average number of hydrogen bonds per hydroxide ion OH^- is shown as a function of distance to the GaN surface. In the bottom panel, the average number of hydrogen bonds per water molecule is also shown.

Fig. 5.5 top panel shows that hydroxide ions OH^- have an average total number of 2.0$\sim$2.3 H-bonds when bonded to surface Ga cation sites. The number of their donor and acceptor H-bonds are about 0.8 and 1.4, respectively. Fig. 5.5 bottom panel shows the average number of H-bonds of H_2O molecules in the system. When H_2O is bound to surface Ga cation sites, it has an average total number of of 2 H-bonds where all H-bonds are donor type. However, when H_2O is sufficiently far away from surface, it becomes bulk water and thus has an average total number of 3.8$\sim$4.0 H-bonds, with equal numbers of donor type and acceptor type of H-bonds. In between bulk and surface, there is an interfacial layer of water that interacts with both surface and bulk. The hydrogen bond structure of this interfacial layer is different from the bulk region since the nearly tetrahedral H-bond structure is broken and more defects are included within the interfacial layer.

It is worth noting that a Ga-OH species can be analogous to a water molecule and Ga-H_2O species can be analogous to hydronium H_3O^+ with Ga replacing one of the protons. However, hydrogen bonds can only be formed by H atoms interacting with O lone pairs within a specified distance. Since hydroxide ions OH^- only have one proton, they can have at most one donor type of H-bond. The lone pairs of O atom in hydroxide ions OH^- are redistributed because of a Ga-O bond replacing an O-H bond but it is still possible for the

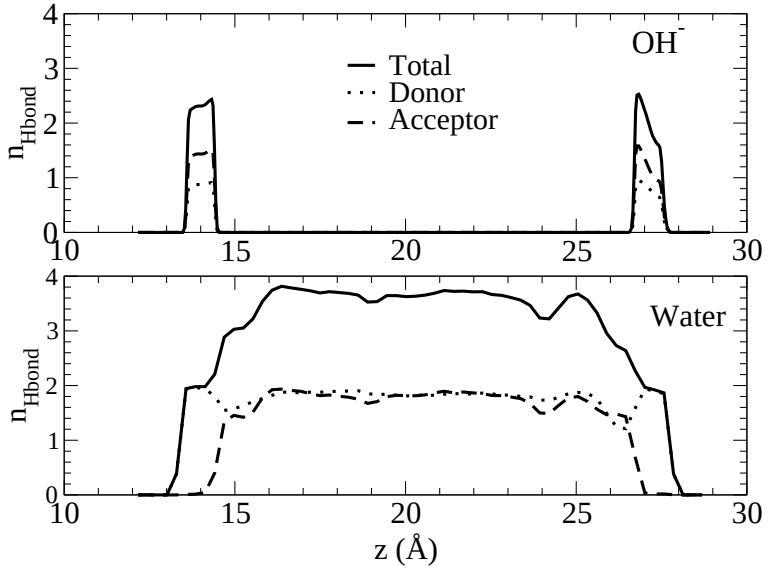

Figure 5.5: The average number of hydrogen bonds with respect to central O atom of molecules in the layers along the direction perpendicular to the GaN $10\underline{1}0$ surface for different species. Top: The average number of hydrogen bonds per hydroxide ion OH^- as a function of distance to GaN surface. Bottom: the average number of hydrogen bonds per water molecule as a function of distance to GaN surface. In particular, we further count the number of H-bond donors(dotted line) and acceptors(dashed line) for each species and the total number of hydrogen bonds per molecule is also reported as a continuous line. We chose the following geometric criterion to define a hydrogen bond: $O\cdots O$ distance shorter than 3.5 $\mathring{A}$ and $O\cdots$ H–O angle larger than 140 °.

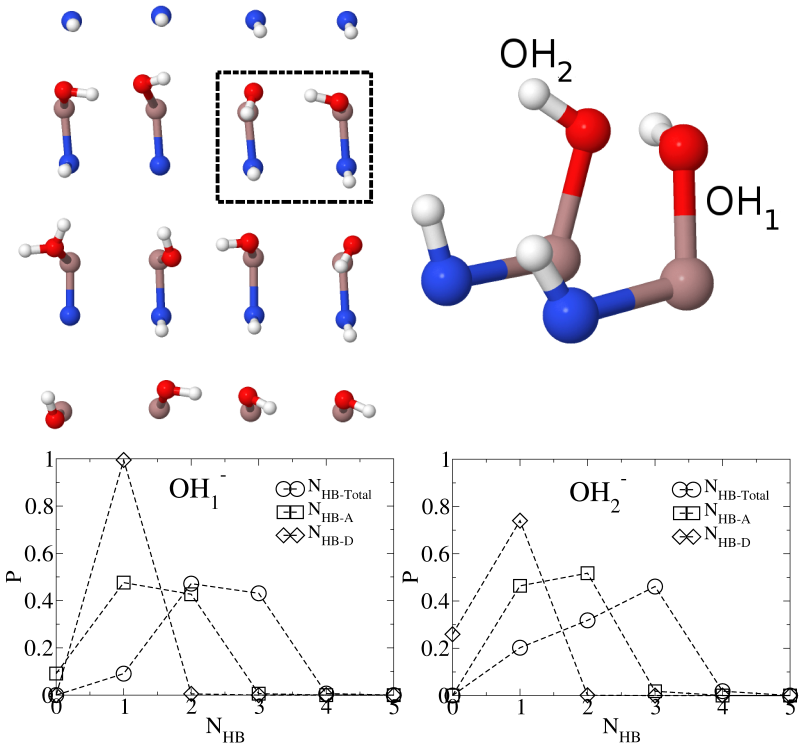

Figure 5.6: Top: (left) Top view of the a typical fully solvated GaN 10$\underline{1}$0 surface from a snapshot. The species bonded to Ga cation sites include hydroxide ions OH^- and H_2O. We define hydroxide ions OH^- that make hydrogen bonds to other hydroxide ions OH^- as OH_1^- and those receive hydrogen bonds from hydroxide ions OH_1^- as OH_2^-. The average O-H bond distance is 0.993 Å for OH_1^-s and 0.986 Å for OH_2^-s. Bottom: The distribution of total number of hydrogen bonds of OH_1^- and OH_2^- ($N_{HB\text{-}total}$, circle). The distribution of average number of donor($N_{HB\text{-}D}$, diamond) and acceptor($N_{HB\text{-}A}$, square) type of H-bonds are also shown.

OH^- to form acceptor type of H-bonds. In the case of Ga-H_2O, the lone pairs of O atom are bound to Ga cations and thus no acceptor type of H-bond can be formed for that type of species. At the same time, two H atoms of Ga-H_2O can form two donor types of H-bond.

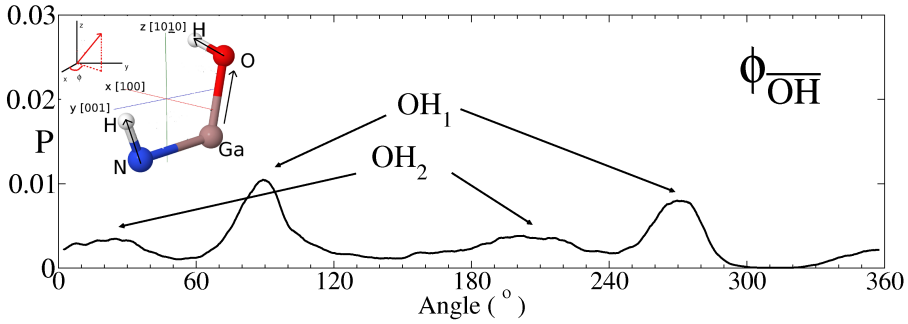

Figure 5.7: The angular distribution of O-H vector of hydroxide ions OH^- on fully solvated GaN 10$\bar{1}$0 surface during the AIMD simulation is shown. The distribution of the angle $\phi_{\text{O-H}}$ (defined as the angle between the projection of O-H vectors of the hydroxide ions OH^- onto the 10$\bar{1}$0 surface and the x axis) is shown. The y axis is GaN wurtzite c axis (001) and z axis is normal vector of 10$\bar{1}$0 plane, x axis is perpendicular to y axis within the 10$\bar{1}$0 plane.

In Fig. 5.7, the distribution of the angle $\phi_{\text{O-H}}$ (defined as the angle between the projection of O-H vector of the hydroxide ions OH^- on GaN 10$\bar{1}$0 plane and x axis) is shown. The y axis is GaN wurtzite c axis (001) and z axis is the normal vector of the 10$\bar{1}$0 plane. The x axis is perpendicular to y axis within the 10$\bar{1}$0 plane. Fig. 5.7 shows the angular distribution of O-H vectors of hydroxide ions OH^- on fully solvated GaN 10$\bar{1}$0 surface during the AIMD simulation. The two strong peaks at around 90° and 270° can be associated with the O-H bond of OH_1^-. They represent a rather strong donor type of H-bond, which softens the intramolecular O-H bond in OH_1^-. On the other hand, O-H bond of OH_2^- can only form donor type of H-bond with interfacial water. Therefore the two broader angular distribution peaks at 30° and 210° can be associated with OH_2^- which has a rather weaker donor type of H-bond with water. In turn the covalent OH bond in OH_2^- will be stronger and the two types of hydroxyl ions at the surface should in principle be distinguishable

in the IR spectrum of the system. OH_2^- should have the highest frequency in the spectrum, and OH_1^- should have a smaller frequency, different both from the bulk water OH stretching and the OH_2^- stretching.

In Fig. 5.6, we define hydroxide ions OH^- that make hydrogen bonds to other hydroxide ions OH^- as OH_1^- and those receive hydrogen bonds from hydroxide ions OH_1^- as OH_2^-. The configuration of a typical hydroxide ions OH^- dimers is shown. The average O-H bond distance is 0.993 Å for OH_1^-s and 0.986 Å for OH_2^-s. The covalent O-H bonds of two types of hydroxide ions OH^- are different because of different H-bond configuration. The bottom panel of Fig. 5.6 shows the distribution of H-bonds of OH_1^- and OH_2^-. The distribution of average number of donor and acceptor type of H-bonds of OH_1^- as OH_2^- are also shown in the same figure. Both OH_1^- and OH_2^- can form at most one donor hydrogen bond with its sole H atom. By definition, OH_1^- always makes one donor type of H-bond to OH_2^-. However, OH_2^- has the freedom to not form any H-bond with water, causing the average donor type of H-bond to drop to around 0.8. On the other hand, the average number of acceptor type of H-bonds is 1.3 for OH_1^- and 1.5 for OH_2^-. Although the total average number of H-bonds of hydroxide ions OH^- is the same, ~ 2.3, the H-bond structure characteristics are very different. The strong donor type of H-bond of OH_1^- makes its O-H covalent bond weaker and thus has 0.7% larger O-H bond length.

5.2.4 Structure of the System

Fig. 5.5 shows that water molecules confined within two GaN surfaces can be separated into three region: surface, interfacial and bulk. We have shown that about 80% of water molecules at the surface are dissociated to ions OH^- and H^+ that are bound to Ga cation sites and N anion sites. The rest of water molecules at the surface are bonded to Ga cation sites through the O atom lone pairs. Both hydroxide ions OH^- and H_2O on the surface are interacting with interfacial water via H-bonds. The tetrahedral structure of this interfacial water is broken. This can be seen from H-bond analysis in Fig. 5.5, in which interfacial water has more under-coordinated defects.

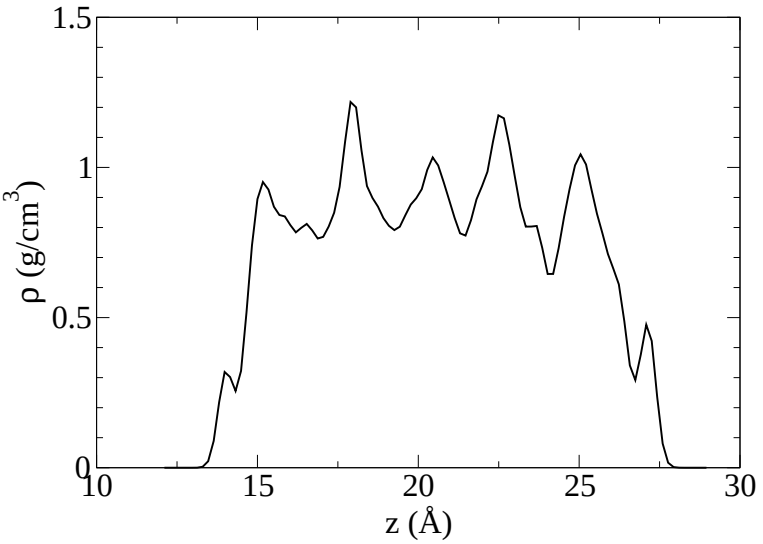

Figure 5.8: The density of water molecules computed along the direction perpendicular to GaN 10$\underline{1}$0 surface.

In Fig 5.8, the densities of water are calculated in layers along the direction perpendicular to GaN 10$\underline{1}$0 surface. Therefore water in the interfacial layer not only have a broken tetrahedral H-bond network, but also have a substantially lower density than bulk water. The depth of this interfacial water can be defined from water density distribution in Fig 5.8 or H-bond structure in Fig. 5.5, both $\approx 1.5\mathring{A}$. If we consider bulk water to have almost four H-bonds per molecule and equal number of donor type and acceptor type of H-bonds, then the bulk water can be identified within [16Å , 25Å] in the direction perpendicular to GaN surfaces. Thus bulk water molecules can be viewed as confined in a 12.944 Å ×15.786 Å × 9.0Å cell. On average, the bulk region contains 60 $\sim$ 62 water molecules and thus the bulk water equilibrium density is within range between 0.97 to 1.01 g/cm^3.

Fig. 5.9 shows the distribution of the number of H-bonds per water molecule from AIMD simulation. The distributions are separated into three groups which are top: total number of H-bonds per molecule(N_{HB}), center: the number of acceptor H-bonds per molecule(N_{HB-A}) and bottom: the number of donor H-bonds per molecule(N_{HB-D}). Bulk represents all bulk water

molecules. L1 represents interfacial water that are hydrogen bonded with surface groups such as Ga–OH, Ga–H_2O or free N anion sites. Surface represents water molecules bonded with the surface cation Ga sites with the lone pairs of O atom.

The first obvious result is that once the water molecules are molecularly adsorbed by the surface Ga sites, the lone pairs of the water molecules are no longer available, which limits this type of water molecules to donate two H-bonds with bulk water molecules.

The bulk water in this study has a similar distribution of H-bonds per molecule as pure water from the chapter 3. Due to the nearly tetrahedral structure of the H-bond network, the ideal coordination of neighboring H-bonds for water in the bulk region is close to 4, with 2 Donor type of H-bonds and 2 acceptor type of H-bonds.

The L1 (interfacial layer) water, on the other hand, has more under-coordinated defects due to the broken symmetry of the H-bond structure near the surface. This broken symmetry has many causes. The most important one is the constraint of H-bond between surface molecules and interfacial water. Surface hydroxide ions OH^- and H_2O interact with interfacial water via H-bonds, but with limited types and ranges of solid angles. At the same time, surface free anion N sites tends to attract the H atom of water molecules to form a H-bond like bond with their strong dangling bonds. This pseudo "H-bond" will have a stronger bond strength than normal H-bond because the N dangling bond will be more attractive to H atoms than O atom lone pairs. In summary, interfacial water is interacting with all surface groups including Ga–OH^-, Ga–H_2O and free N anion sites with different characteristics of limited types of H-bonds.

Fig. 5.10 shows radial distribution functions of several species. In the top panel, oxygen-oxygen (O-O) radial distribution functions (RDF) of oxygen atoms of bulk water and oxygen atoms of surface OH^-s are compared. At the same time, oxygen atoms of 64 water molecules from an independent simulations using PBE is also shown. Compared with oxygen atoms of bulk water and PBE-water, OH^-s have almost the same position of the first peak, indicating that the first neighbor O-O distance between dimer OH^-s is similar to that

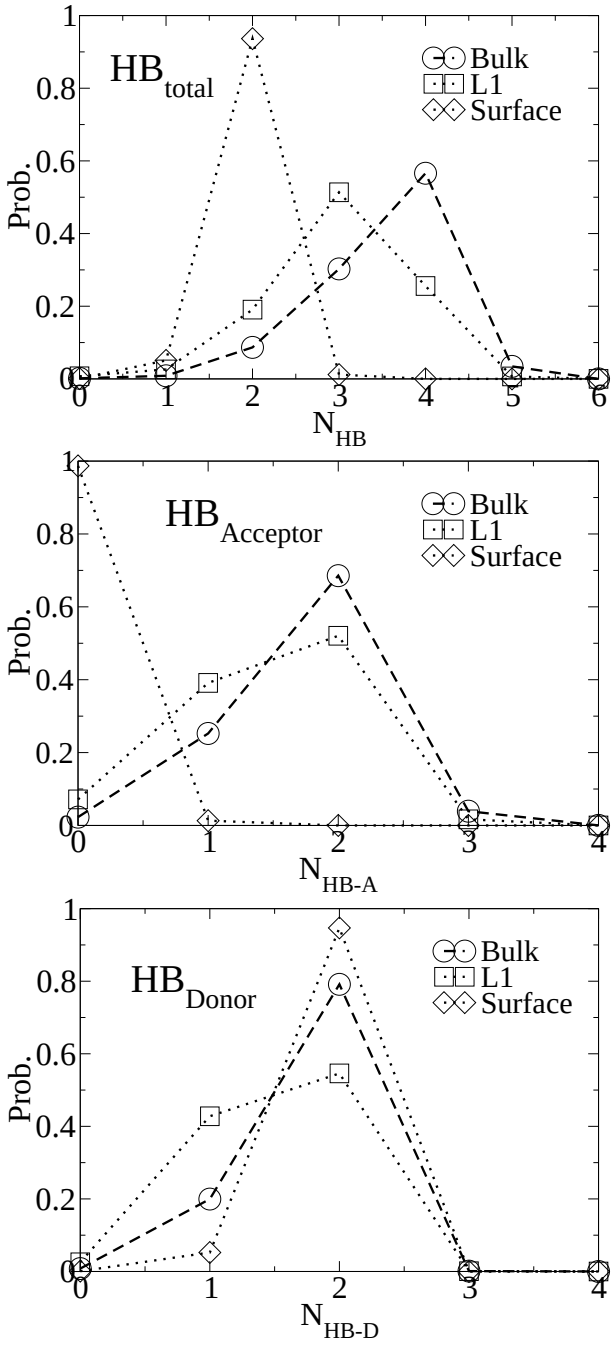

Figure 5.9: The distributions of the number of H-bonds per water molecule from AIMD simulation are shown. The distributions are separated into three groups which are top: total number of H-bonds per molecule(N_{HB}), center: the number of acceptor H-bonds per molecule(N_{HB-A}) and bottom: the number of donor H-bonds per molecule(N_{HB-D}) Bulk represents all bulk water molecules. L1 represents interfacial water that are hydrogen bonded with surface groups such as Ga–OH, Ga–H_2O and free N anion sites. Surface represents water molecules bonded with the surface cation Ga sites with the lone pairs of O atoms.

of water. However, the oxygen atoms of other OH^-s are populated between the first and the second neighbor shell. At the same time, the second neighbor shell of OH^-s are still interfacial water and collapse due to the breaking of H-bonds. The two effects together make the oxygen-oxygen RDF as shown in Fig. 5.10. Please note that although the height of the first peak of RDF of surface OH^-s are quite similar to that of bulk water, the number of O atoms within first shell are not the same. This is due to formula:

$$N = \int_0^{R_1} \rho A(r) g_{OO}(r) dr \tag{5.1}$$

where $g_{OO}(r)$ is the O-O RDF, R_1 is the first coordination shell cutoff radius, which is considered to be the first minimum of $g_{OO}(r)$, and A(r) is a space phase factor for each species. $A(r) = 4\pi r^2$ for bulk water and $A(r) = 2\pi r^2$ for surface OH^- since only half sphere is available to populate. Here we also assume that the entropic factors are adequately sampled in the AIMD trajectories; otherwise additional constraints and entropic factors need to be considered. Therefore the average number of O atoms within first coordination shell of surface OH^- is only about half of water.

Fig. 5.10 middle panel shows oxygen and hydrogen RDFs of bulk water molecules in this work, surface OH^-s in the system. At the same time, oxygen atoms of 64 water molecules from an independent simulations using PBEis also shown. The first peak represents the covalent bond and O-H distance of OH^-s is slightly smaller than that of water, indicating a slightly stronger covalent bond. The second peak is the usual distance of $H\cdots O$ within a typical hydrogen bond. The position of the second peak for OH^-s is 1.77Å , slightly smaller than the position for water which is around 1.79∼1.80 Å . This indicates that acceptor type of hydrogen bonds of OH^-s are relatively stronger.

Fig. 5.10 bottom panel shows nitrogen and hydrogen RDFs of nitrogen atoms that are bound to H^+ (Bonded N) (solid line) and nitrogen atoms that still have dangling bonds (Free N). The bonded N atoms have N-H covalent bonds with an average distance of 1.015 Å (this is shown as the first peak of N-H RDF of Bonded N), longer than usual O-H covalent bond. The free N

atoms still have strong dangling bonds that attract H atoms of water molecules. Therefore there is a H-bond-like bond formed between free N sites and water molecules, which can be seen from the first peak of N-H RDF for the Free N at around 1.76Å . This indicates that mismatched N anion sites attract water H atoms to form pseudo "H-bond". Similarly, Ga cation sites attract water lone pairs to form another type of pseudo "H bond".

Please note that once those mismatched N anion sites exist in the system, they will become the natural photo-holes holders. So the photo-induced hole will be localized to those N atoms. Also part of the localized hole will have weight on the O atoms of neighbor waters that are bonded to those free N atoms through "pseudo H-bonds". This raise extremely important question of many possible reaction initial states and photocatalytic reaction models starting from these initial configurations which need to be studied.

5.2.5 Proton Diffusion

Proton diffusion was found in liquid water with excess protons two hundred years ago. The Grotthuss mechanism was proposed in which an "excess" proton or protonic defect diffuses through the hydrogen bond network of water molecules or other hydrogen-bonded liquids through the formation or cleavage of covalent bonds. In his 1806 publication "Theory of decomposition of liquids by electrical currents", Theodor Grotthuss proposed a theory of water conductivity. The Grotthuss mechanism is now a general notation for the proton-hopping mechanism. The details of the hopping and transport mechanism are still under debate, but the main two forms of processes were proposed to be either $H_9O_4^+$ (Eigen cation) or $H_5O_2^+$ (Zundel cation). Currently there are two plausible mechanisms which are: 1. Eigen to Zundel to Eigen (EZE), on the basis of experimental NMR data[109] and Zundel to Zundel (ZZ), on the basis of molecular dynamics simulation[103].

Proton diffusion can be only found in liquid water with relatively short simulation (within ps) when excess protons exist[103], we have observed it during our AIMD simulation with the GaN $10\underline{1}0$ surface serving as catalyst. From careful observations and analysis of the AIMD simulations performed in

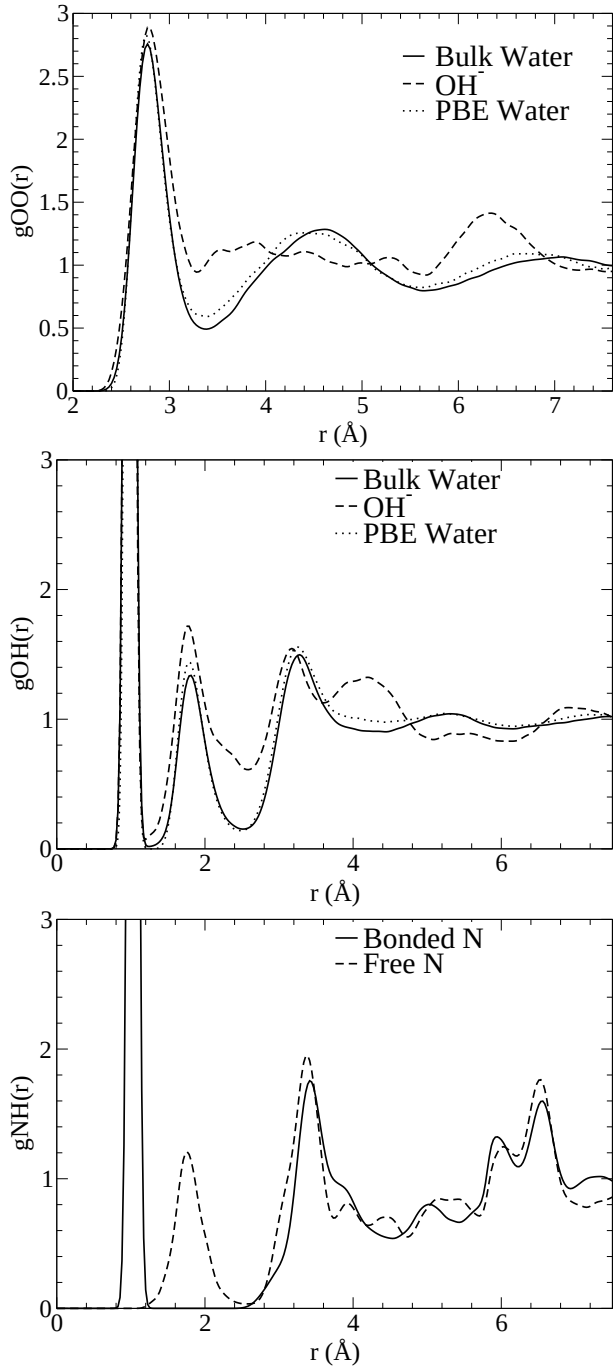

Figure 5.10: Top: Oxygen-oxygen(O-O) radial distribution function(RDF) of oxygen atoms of bulk water in this work (Bulk Water), oxygen atoms of surface OH^-s (OH^-) and oxygen atoms of 64 water molecules from an independent simulations using PBE (PBE-Water) is shown. Middle: Oxygen and hydrogen RDFs of bulk water molecules in this work (Bulk Water)(black solid line), surface OH^-s in the system (OH^-s)(black dashed line) and water molecules from an independent simulations using PBE (PBE-Water)(black dotted line). Bottom: Nitrogen and hydrogen RDFs of nitrogen atoms that are bound to H^+ (Bonded N) (solid line) and nitrogen atoms that still have dangling bonds (Free N) (dashed line).

this work, we have found that all proton diffusion processes are initiated from molecularly adsorbed water. H_2O on the surface is bound to free Ga cation site with pseudo "H-bond" in which a Ga dangling bond attracts the lone pair of O atoms. This type of Ga–H_2O group can be thought as a hydronium H_3O^+, with Ga replacing the excess proton. From Fig. 5.5 and Fig. 5.9, it can be already seen that H_2O of Ga–H_2O groups prefers to form two donor H-bonds with neighbor molecules, with one proton forming an H-bond with a neighbor OH^- that is bound to a surface cation Ga site and one proton forming an H-bond with a bulk water. Therefore there are two possible pathways of proton diffusion with initial Ga–H_2O groups along H-bonds, one from surface H_2O to neighbor surface OH^-s ($Diff_{s\text{-}s}$), and the other from surface H_2O to bulk water ($Diff_{s\text{-}b}$). Fig . 5.11 shows the two types of proton diffusion processes mentioned above. After the hopping protons are transferred into bulk, we have found the Grotthuss mechanism type of proton diffusion "$Diff_{b\text{-}b}$" shown at the right of Fig . 5.11.

In the AIMD simulation, these types of diffusion processes can happen both during the solvation process(within 1.5ps) and after the solvation process (after 1.5 ps). We find the frequencies of all types of proton transfer events after equilibration are rather high, indicating their free energy barriers should be comparable to room temperature thermal energy. One can already know from [103] that excess protons can be considered part of a "low barrier hydrogen bond", in which tunneling is negligible and transition-state theory does not apply. Although the classical treatment of nuclei during proton transfer processes has been shown to overestimate effective free energy barrier by 50% [103], it would not hurt our purpose to compare the free energy barriers of different types of proton transfer processes in this study or to compare those values with free energy barriers found for hopping excess protons in liquid water when ignoring zero point energy.

The choice of a proton diffusion reaction coordinate is somewhat arbitrary and should be chosen so as not to influence the free energy barrier. In Fig. 5.12, Fig. 5.13 and Fig. 5.14 we show the two dimensional distribution function $P(\delta,R_{OO})$ of the displacement coordination δ=R_{O_aH}-R_{O_bH} of a given proton and corresponding oxygen-oxygen atom distance R_{OO}, where O_a and O_b are

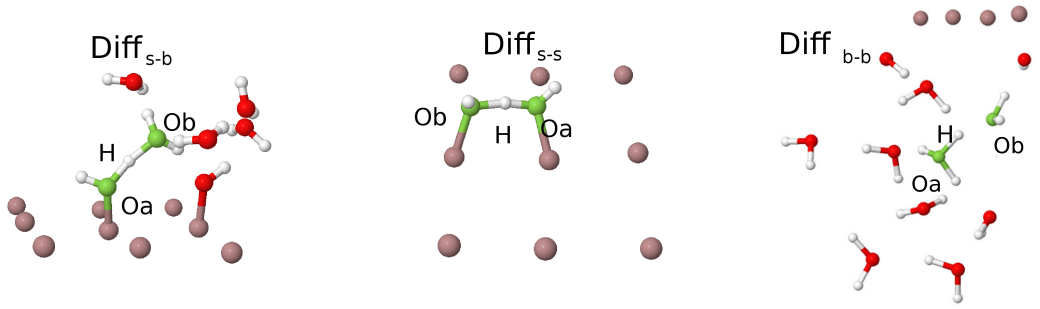

Figure 5.11: Three types of proton diffusion processes are defined as (left) "$\text{Diff}_{\text{s-b}}$" to be the proton diffusion between Ga–H_2O and bulk water, (middle) "$\text{Diff}_{\text{s-s}}$" to be the proton diffusion between Ga–H_2O and Ga–OH and (right) "$\text{Diff}_{\text{b-b}}$", the Grotthuss mechanism after hopping protons are transferred by "$\text{Diff}_{\text{s-b}}$" into bulk. The green atoms are oxygen atoms that are involved in proton transfer process, red atoms are oxygen atoms of neighbor water molecules, white are H atoms and brown are Ga.

defined as oxygen atoms that are involved in donating and receiving proton H. The definition of O_a and O_b are different for "$\text{Diff}_{\text{s-b}}$", "$\text{Diff}_{\text{s-s}}$" and "$\text{Diff}_{\text{b-b}}$". In addition, the $P(\delta,R_{OO})$ distributions are normalized to unity and shown on the same scale.

As shown in Fig. 5.11(left), O_a in "$\text{Diff}_{\text{s-b}}$" is always defined as the O atoms of H_2O bound to surface Ga cation sites (Ga–H_2O) and O_b is always defined as the O atom of water that receive the hopping proton H through a hydrogen bond. For "$\text{Diff}_{\text{s-s}}$", O_a is defined as the O atom of Ga–H_2O and O_b is defined as the O atom of Ga–OH that receive the hopping proton H through a hydrogen bond on the surface. Please note that the definition of O_a and O_b can be switched, meaning O_a can be defined as O atom of Ga–OH and O_b can be defined as O atom of Ga–H_2O. The reason is that once the proton transferred, the original Ga–H_2O becomes the new Ga–OH and vice versa. It is worth recalling that Ga–H_2O can be considered analogous to H_3O^+. Like H_3O^+, we should always find the hopping proton within Ga–H_2O. In our case, the transferring proton is defined as the one that has the smaller absolute value of R_{O_aH}-R_{O_bH}, meaning that this proton is more likely to be "on its way" of transferring to the next O atom.

Once the hopping proton is transferred into bulk, then it becomes an excess proton in liquid water. Thus we use the same definition of O_a and O_b for "$\text{Diff}_{\text{b-b}}$" as in Ref.[103]. O_a is defined as the center O atom of the most probable H_3O^+, and there are three H atoms to form H-bonds with neighbor molecules. The most probable O_b is defined as the O atom that has the smallest absolute value of δ=R_{O_aH}-R_{O_bH}, meaning this H atom is the most probable proton "on its way" to find next O atom.

Fig . 5.12 shows the two-dimensional distribution function P(δ,R_{OO}) and its contour plot for the proton diffusion processes ($\text{Diff}_{\text{s-b}}$). The distribution (geometric character of O_aHO_b triplets) is characterized by two prominent peaks around (δ,R_{OO})$\approx$(-0.55,2.6) Å and (0.7,2.6) Å . The P(δ,R_{OO}) distribution of both "$\text{Diff}_{\text{s-b}}$" type of proton diffusion has a non-negligible weight at $\delta\approx$0 Å. This provides evidence of the existence of centrosymmetric complexes (Ga–$H_2O\cdots H_2O$), similar to $H_5O_2^+$ (Zundel cation) in liquid water. However, the distribution shows that protons are more likely to be within Ga–H_2O. The effective free-energy profile along the proton transfer coordinate δ can be obtained from ΔF=-K_bT ln$[\int dR_{OO}P(R_{OO},\delta)]$. Fig . 5.12 shows that the effective free-energy barrier for proton transferring from Ga–H_2O to bulk water is around 65 mev. The reverse path, from H_3O^+ to Ga–OH, has a free-energy barrier around 55 mev. The asymmetry of the free-energy profile is due to the asymmetry of Ga–$H_2O\cdots H_2O$.

Fig. 5.13 shows two-dimensional distribution function P(δ,R_{OO}) and its contour plot for the first type of proton diffusion process($\text{Diff}_{\text{s-s}}$). The distribution (geometric character of O_aHO_b triplets) is characterized by two prominent peaks around (δ,R_{OO})$\approx$($\pm$0.5,2.5) Å . It also has significant non-negligible weights at $\delta = 0$ Å . This evidence of existence of centrosymmetric complexes(Ga–$H_2O\cdots$Ga–OH) is also similar to $H_5O_2^+$ (Zundel cation) in liquid water. Fig. 5.13 shows that the effective free-energy barrier for hopping protons between Ga–H_2O and Ga–OH is around 40 mev, lower than free-energy barrier of "$\text{Diff}_{\text{s-b}}$".

In Fig. 5.14, we also study the Grotthuss mechanism after hopping protons are transferred into bulk. This type of proton diffusion is recognized as "$\text{Diff}_{\text{b-b}}$" as shown in Fig.5.11(right). The effective free-energy profile along the proton transfer coordinate δ can be obtained from ΔF=-K_bT ln$[\int dR_{OO}P(R_{OO},\delta)]$.

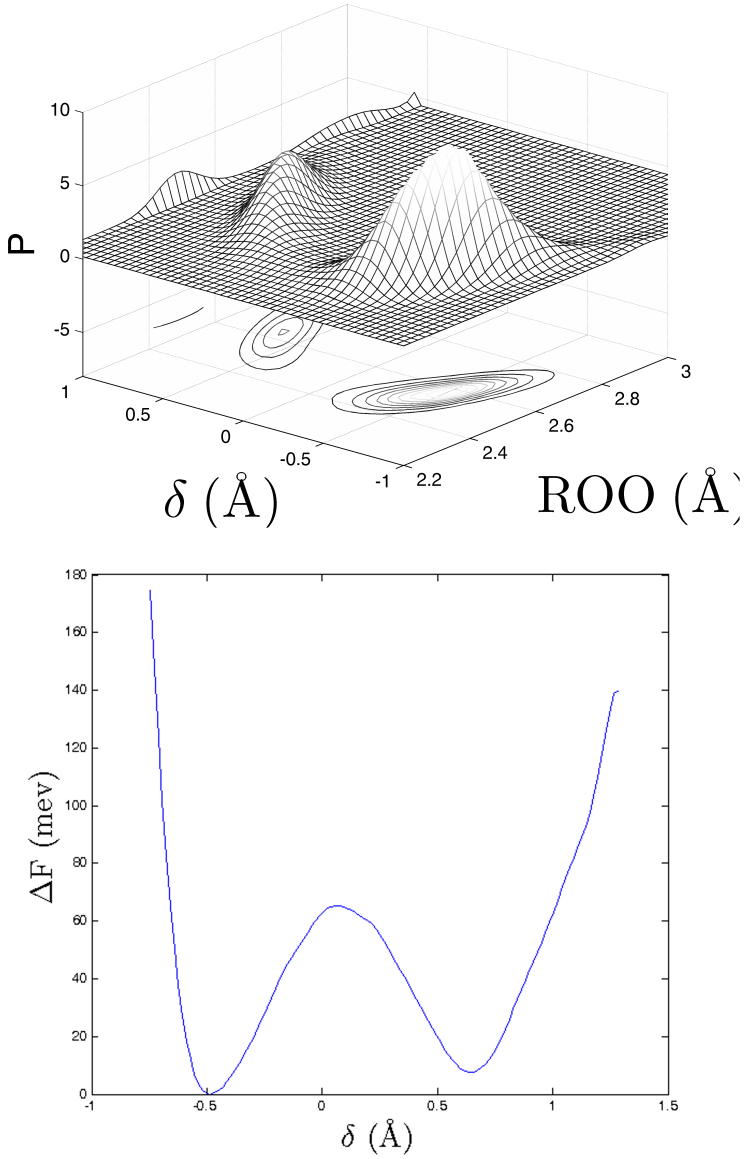

Figure 5.12: "$\text{Diff}_{\text{s-b}}$" type of diffusion process: The two-dimensional distribution function P(δ,R_{OO}) of the displacement coordination δ=R_{O_aH}-R_{O_bH} of a given proton and corresponding oxygen-oxygen atoms distance R_{OO}. O_a in "$\text{Diff}_{\text{s-b}}$" is always defined as the O atom of H_2O bound to a surface Ga cation site (Ga–H_2O) and O_b is always defined as the O atom of a water that receives the hopping proton H through a hydrogen bond. In addition, the P(δ,R_{OO}) distributions are normalized to unity and shown on the same scale. The effective free-energy profile along the proton transfer coordinate δ can be obtained from $\Delta\text{F}=-\text{K}_b\text{T}\ \ln[\int dR_{OO}P(R_{OO},\delta)]$.

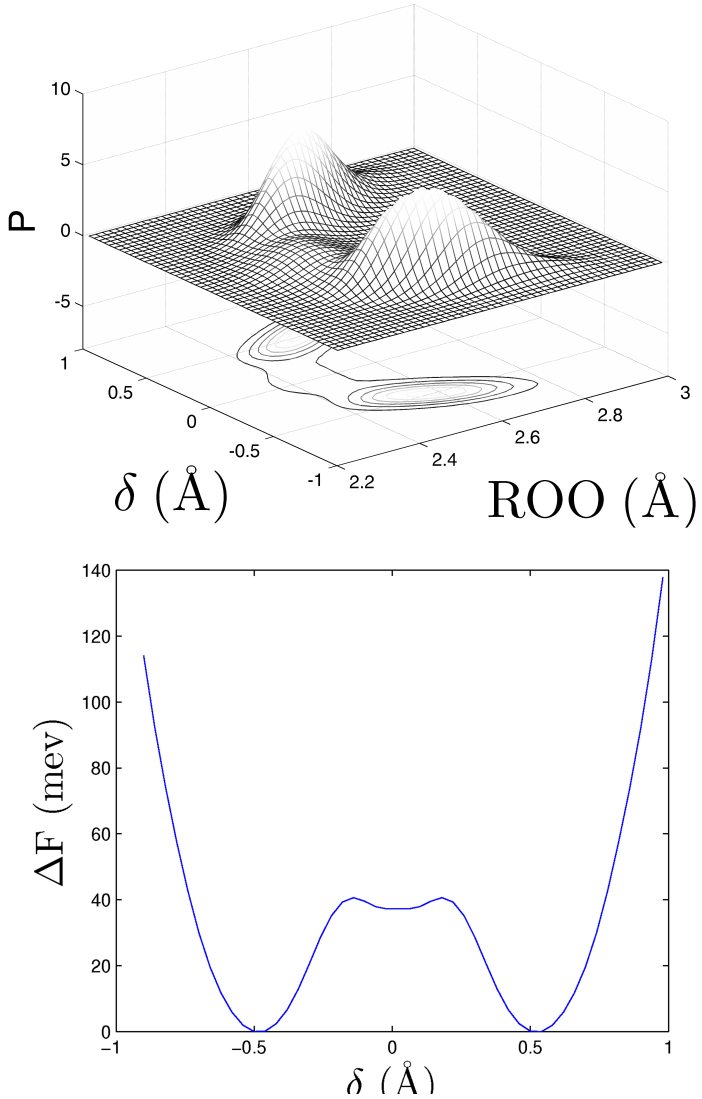

Figure 5.13: "Diff$_{s\text{-}s}$" type of diffusion process: The two-dimensional distribution function P(δ,R$_{OO}$) of the displacement coordination δ=R$_{O_aH}$-R$_{O_bH}$ of a given proton and the corresponding oxygen-oxygen atom distance R$_{OO}$, where O_a is defined as the O atom of Ga–H_2O and O_b is defined as the O atom of the Ga–OH that receives the hopping proton H through a hydrogen bond. Please note that the definition of O_a and O_b can be switched, meaning O_a can be defined as the O atom of Ga–OH and O_b can be defined as the O atom of Ga–H_2O. The reason is that once the proton transfers, the original Ga–H_2O becomes the new Ga–OH and vice versa. The P(δ,R$_{OO}$) distribution is smoothed and symmetrized about $\delta = 0\mathring{A}$. In addition, the P(δ,R$_{OO}$) distributions are normalized to unity and shown on the same scale. The effective free-energy profile along the proton transfer coordinate δ can be obtained from ΔF=-K$_b$T ln$[\int dR_{OO}P(R_{OO},\delta)]$.

The free-energy barrier for "$\text{Diff}_{\text{b-b}}$" is found to be around 20 meV, about the same as the value in the classical limit in Ref.[103]. As in excess protons in liquid water, the effective free energy barrier is also very small (comparable to thermal energy $K_bT \approx 26$ mev at room temperature) for "$\text{Diff}_{\text{b-b}}$". It has been shown that the rate of excess proton diffusion in liquid water is determined by thermally induced hydrogen-bond breaking in the second solvation shell. In our AIMD simulation with GaN facilitated proton transfer, the second shell of both oxygen atoms of water within interfacial shell or surface groups is broken as already shown in Fig. 5.5 and Fig. 5.9. It seems to be easier to transfer a proton into interfacial water or other surface OH^- groups. However, in our system, constraints are applied, since the initial proton transfer process can only be initiated from Ga–H_2O. Although Ga–H_2O can be viewed as H_3O^+, the Ga–O bond is much weaker than the O–H covalent bond. If a hopping proton of H_3O^+ can be viewed as pushed away by the two other H atoms, the higher free energy barrier of $\text{Diff}_{\text{s-b}}$ means the Ga–O bond is too weak to "push" the proton away.

The deprotonation free energy barrier of transfering a proton from a surface water to a bulk water ("$\text{Diff}_{\text{s-b}}$") at the GaN $10\underline{1}0$/Aqueous interface is around 65 mev as shown in Fig.5.13. The pK_a can be derived from a similar method as in Ref[114]the standard-state deprotonation free energy $\Delta G^{(0)}$ via $-log_{10}exp(-\beta\Delta G^{(0)})$, where β is $1/k_BT$ and

$$\Delta G^{(0)} = -k_BTln\left\{C_0\int_0^{R_{cut}} dRA(R)exp[-\beta\Delta F(R)]\right\} \tag{5.2}$$

Here C_0 denotes 1.0 M concentration, R is the reaction coordinate defined as R_{O_aH} in Fig.5.11 for "$\text{Diff}_{\text{s-b}}$", A(R) is a space phase factor determined by the integral of vector $\overrightarrow{O_aH}$'s solid angle distribution times R^2, R_{cut} is the cutoff distance delimiting the reaction corresponding to $\delta \approx 0$ as in Fig.5.12, and $\Delta F(R)$ is the free energy potential profile which provides information needed to calculate the free energy of deprotonation.

The pK_a in liquid water from our AIMD simulations using the above method is $\sim$ 3.0. This indicates that the GaN $10\underline{1}0$ surface yield an acid aqueous media.

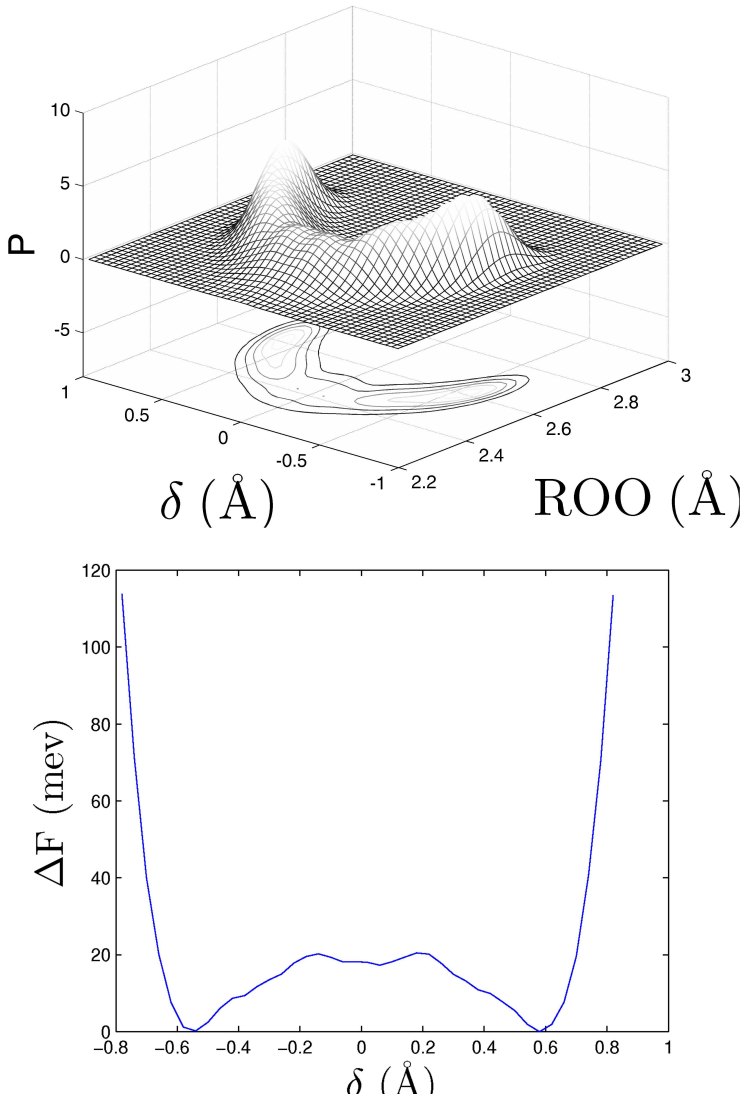

Figure 5.14: "$\text{Diff}_{\text{b-b}}$" type of diffusion process: The two dimensional distribution function P(δ,R_{OO}) of the displacement coordinate δ=R_{O_aH}-R_{O_bH} of a given proton and corresponding oxygen-oxygen atoms distance R_{OO}, where O_a is defined as the center O atom of the most probable H_3O^+, and there are three H atoms to form H-bonds with neighbor molecules. The most probable O_b is defined as the O atom that has the smallest $|\delta|$ of δ=R_{O_aH}-R_{O_bH}, meaning this H atom is the most probable proton "on its way" to find next O atom. In addition, the P(δ,R_{OO}) distributions are normalized to unity and shown on the same scale. The P(δ,R_{OO}) distribution is smoothed and symmetrized about $\delta = 0\mathring{A}$. The effective free-energy profile along the proton transfer coordinate δ can be obtained from ΔF=-K_bT ln$[\int dR_{OO}P(R_{OO},\delta)]$.

5.2.6 Vibrational Spectrum

In Fig. 5.15, we analyze the O-H vibrational spectrum for water in our study with GaN interfaces, and compare with our independent study of 64 pure water molecules with PBE. Also, we analyze the Ga-O vibrational spectrum for Ga-O bond at the surface. We calculate the vibrational density of states by computing the Fourier transform of the velocity-velocity autocorrelation functions. Please note that we are using the heavy water in all our simulations so that here we use heavy water experimental vibrational spectrum data to compare with our simulation results.

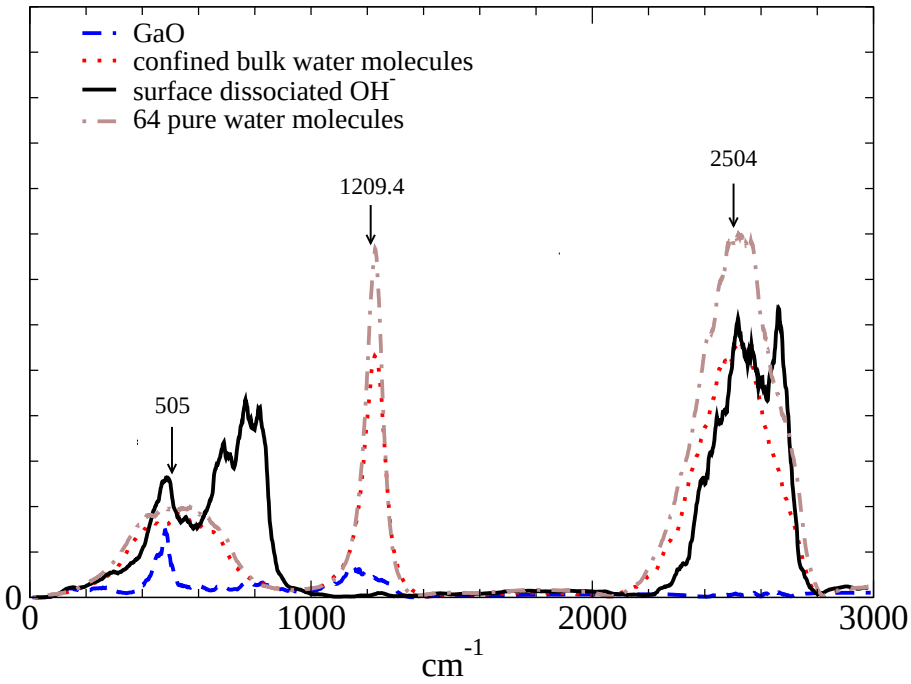

Figure 5.15: Velocity Density of the States(VDOS) of OD^-(solid black line), bulk water(dashed green line), PBE-water and GaO (solid red) are compared. Arrows indicate the experimental peak positions of heavy water from Ref.[104, 105].

From our simulations, the vibrational spectrum obtained from PBE water and bulk water in this study both match well with experiment in the high frequency range.[104] The bond-bending mode of D_2O water is at about 1210

cm^{-1} and the stretching modes are at about 2500 cm^{-1}. Our results for both are close to the experimental value with small errors. The low frequency peak at 505 cm^{-1} is associated with librational modes due to the restrictions imposed by hydrogen bonding. [105, 106] Meanwhile, OD^- show a stronger mode at 800 cm^{-1} compared with normal covalent O-H bonds in water molecules. The new modes could be associated with bending modes of Ga–OH species. The surface Ga-O bond stretching mode is near 480 cm^{-1}. The OH^-s show two stretching modes at 2496cm^{-1} and 2663 cm^{-1}. We have identified that 2496 cm^{-1} peak is associated with OH_1^- and 2663 cm^{-1} peak is associated with OH_2^-. This is because OH_2^- has a stronger O-H covalent bond which correlates with the fact that the average bond length of OH_2^- is much shorter.

5.2.7 Conclusion

Ab initio molecular dynamics simulation is performed for a GaN (10$\underline{1}$0) surface slab hydrated by 94 D_2O molecules. A slab geometry of 5-layer($4 \times 3 \times 5$) GaN units separated by 16.2 of vacuum is used to contain total 24 surface GaN sites available to adsorb water. A summary of this system from AIMD simulation is as following:

- Water molecules on the GaN(10$\underline{1}$0) surface are dissociated into ions such as OH^- (bound to Ga)and H^+ (bound to N). The long-range attraction of the incipient dissociated species with the Ga and N surface sites compensates for the large amount of energy required to stretch the H-OH bond. Dissociation events happen very fast and the surface is fully solvated after the first 1.5 ps of simulation, with no free Ga cation sites on the surface. 20∼21 of the 24 possible GaN surface sites (83%) dissociate water molecules. The remaining 3∼4 Ga sites (17%) are occupied by undissociated water molecules. 40% of all hydroxide ions OH^- can be categorized as OH_1^- that make hydrogen bonds to other hydroxide ions OH^- and equal number of hydroxide ions OH^- can be categorized as OH_2^- that receive hydrogen bonds from hydroxide ions OH_1^-. The remaining 20% do not belong to hydroxide ions dimers on the surface.

- The O-H covalent bond of OH_2^- is stronger than that of OH_1^- which can be directly seen from vibrational spectrum. Although they have the same total number of hydrogen bonds (around 2.3), OH_2^- has more acceptor type H-bonds than OH_1^-, making their H-bond structure very different.

- H_2Os at the surface region are bound to Ga cation sites with pseudo "H-bonds" between the Ga dangling bond and the lone pairs of water. Such H_2Os have two donor type H-bonds, with one to hydroxide ions OH^- and one to water in bulk. When H_2O is sufficiently far away from surface, it becomes bulk water and thus has an average total of 3.6 H-bonds with equal numbers of donor type and acceptor type H-bonds. In between bulk and surface, there is an interfacial layer of water that interacts with both surface and bulk, with more under-coordinated defects.

- Mismatched free N atoms exist, and there is a pseudo H-bond formed between free N sites and water, which can be seen from the first peak of the N-H RDF for the free N at around 1.76Å .

- A GaN surface-facilitated proton diffusion process has been found with Ga–H_2O initial configurations, which are analogous to H_3O^+ in liquid water. There are two possible pathways of proton diffusion with initial Ga–H_2O groups along H-bonds. One is from surface H_2O to neighbor surface OH^-s ($Diff_{s\text{-}s}$), and the other is from surface H_2O to bulk water ($Diff_{s\text{-}b}$). The free energy barriers for both proton transfer processes are larger than excess proton transferring Grotthuss mechanism in liquid water.

Chapter 6

Conclusions and Outlook

Liquid water properties are the main focus of this thesis. Ab initio molecular dynamics simulations are used to investigate those properties. New methods of including van der Waals interactions into the DFT scheme are employed to simulate liquid water. The GaN semiconductor to water interface is studied in particular to unveil the water oxidation mechanism with the GaN $10\underline{1}0$ surface as photocatalyst.

6.1 Water

The performance of ab initio molecular dynamic simulations (AIMD) for liquid water has been studied since the mid nineties. It has been shown that AIMD simulations performed in the past with DFT-GGA methods at room temperature were in fact describing supercooled water, with an effective temperature ranging from 240K to 270 K (at least for diffusivity and RDF purposes) using GGA exchange and correlation density functionals.

The work presented in this thesis represents a very thorough analysis of ab initio liquid water with GGA functionals. This work and others by analyzing the actual situations, illustrates the problems and the strengths of the method. The work related to this purpose was presented in chapter 3.

A large number of simulations have been performed. Structural and dynamical properties of liquid water from different GGA functionals are carefully

investigated and compared. The most widely used PBE[48] density functional shows the best structure in terms of radial distribution fucntion (RDF). However its diffusivity significantly underestimates the measured value. On the other hand, another density functional RPBE[53] gives a significantly understructured behavior however, the self-diffusivity is improved. The two very different results are due to the different description of chemical and electronic properties of water molecule. It has been shown in chapter 3 that RPBE gives an overestimated covalent O-H bond. A common behavior of different GGA's is that equilibrium liquid water densities under ambient conditions are less than experiments.

In chapter 4, improvements to the equilibrium density are shown using functionals that include dispersion non-local van der Waals interactions. A density increase could be accomplished by shortening of bond or increasing number of hydrogen bonds within first coordination shell. However, these two initial hypotheses are ruled out by careful analysis. Addition of van der Waals type bonds are found to account for the density increase by populating the interstitial shell between first and second coordination shell. Although the van der Waals bond strength is almost 10 times smaller than the hydrogen bond, it results in a significant change in structure, with larger first neighbour O-O separation and more structure in interstitial shell. At the same time, self-diffusivity is also improved, meaning no need for temperature rescaling.

A further conclusion to be made is that despite the fact that ab initio liquid water does not compare to experiment as well as was previously thought, it still represents a complete first principles simulation of a very complex system. There is room for improvements, but already important physical properties can be learnt from the study of ab initio water. As long as the limitations are known, it is always possible to distinguish how much of the obtained results can be associated with inherent properties of water and how much should be related to the problems posed by ab initio simulations of the system. Future research areas are open, such as finding a more accurate exchange and correlation functional to describe both inhomogeneity and non-local effects. The overestimation of the bulk modulus using both GGAs and VdWs needs to be solved and deserves more attention.

6.2 GaN/Water Interface

Water is a widely studied interdisciplinary area because of its connections to many subjects such as wet-chemistry, geo-chemistry and biology. In this thesis, an interesting example of wet-chemistry is presented with the study of the pure GaN aqueous interface. The ultimate purpose of this study is related to photocatalytical activity of Pure GaN in the UV region.

In chapter 5, a first principles study of GaN $10\underline{1}0$ - Aqueous interface is carried out to find water oxidation mechanism. An AIMD study of an aqueous GaN slab shows an 80% dissociation of water on the surface of GaN ($10\underline{1}0$), with no vacant Ga sites. This supports Shen et al.'s previous finding that a monolayer of water favorably dissociates on the ($10\underline{1}0$) surface, occupying available surface Ga atoms with hydroxide ions and available N atoms with hydrogen ions.[94] A cluster model was constructed in which the initial state is chosen from AIMD structures. Intermediates of the water oxidation process are identified and studied with the cluster model.

In chapter 5, a thorough and more detailed analysis of GaN ($10\underline{1}0$)-aqueous interface is also performed. OH^- dimers at interface are carefully examined as the characteristic structures of dissociated water molecules on GaN . The dimers are separated into two different types due to the different hydrogen bond environment. It has been shown that they not only have different characteristics of covalent O-H bonds, but also have appreciable difference of neighboring hydrogen bond networks. More importantly, these structural differences of two type of species lead to distinguishable energy levels for the oxygen atoms.

Proton diffusion processes starting with non-dissociated surface water molecules are also found. This unique type of proton diffusion process has a free energy barrier close to room temperature thermal energy, indicating a very different type of water dissociation from the previous finding[94], in which OH^- and H^+ occupy available surface Ga and N atoms at the same time. The proton diffusion is analogous to that found in liquid water with excess protons hydroniums. In this case, surface Ga atoms act as the excess protons.

The method of AIMD simulations and analysis used in investigating this

particular GaN (10$\underline{1}$0)-aqueous interface can be used in any non-polar semiconductor/conductor and aqueous interface. However, recent experiments suggest that a GaN (10$\underline{1}$1) polar surface is common and energetically favored in many GaN nano clusters. The GaN (10$\underline{1}$1) surface is polar, and needs to be carefully treated carefully before including liquid water into the system. A thorough and detailed AIMD study of GaN (10$\underline{1}$1) aqueous interface is needed to unveil the water oxidation mechanism at that interface.

Bibliography

[1] D. Russo, G. Hura, and T. Head-Gordon, Biophysical Journal **86**, 1852 (2004).

[2] D. Denzler, C. Hess, R. Dudek, S. Wagner, C. Frischkorn, M. Wolf, and G. Ertl, Chem. Phys. Lett. **376**, 618 (2003).

[3] A. Poissier, S. Ganeshan, and M. V. Fernandez-Serra, Phys. Chem. Chem. Phys. **13**, 3375 (2011).

[4] T. Futterer, T. Hellweg, G. Findenegg, J. Frahn, A. D. E. Schlter, and C. Bottcher, Langmuir **19**, 6537 (2003).

[5] I. A. Beta, H. Bohlig, and B. Hunger, Phys. Chem. Chem. Phys. **8**, 1975 (2004).

[6] E. Stanley and P. Debenedetti, Physics today **56**, 40 (2003).

[7] R. W. Whitworth and V. F. Petrenko, *Physics of ice* (Oxford University Press, 1999).

[8] C. A. Angell, Ann. Rev. Phys. Chem **55**, 559 (2004).

[9] H. E. Stanley, S. V. Buldyrev, O. Mishima, M. R. Sadr-Lahijany, A. Scala, and F. W. Starr, Journal of Physics: Condensed Matter **12(8A)**, 403 (2000).

[10] Richard M. Martin, "Electronic Structure," Cambridge University Press, 2004, Cambridge, UK.

[11] P. Hohenberg and W. Kohn, "Inhomogeneous Electron Gas," Phys. Rev. **136**, b864 (1964).

[12] F. Stillinger, "Water revisited," Science **209**, 451 (1980).

[13] J. Junquera, O. Paz, D. Sánchez-Portal and E. Artacho, "Numerical atomic orbitals for linear-scaling calculations," Phys. Rev. B. **64**, 235111(2001)

[14] J. M. Soler, E. Artacho, J. D. Gale, A. García and J. Junquera, P. Ordejón and D. Sánchez–Portal, "The Siesta method for ab initio order-N materials simulation," J Phys. Condens. Matter **14**, 2745(2002)

[15] L. Kleinman and D. M. Bylander, "Efficacious Form for Model Pseudopotentials," Phy. Rev. Lett. **48**, 1425(1982)

[16] N. Troullier and J. L. Martins, "Efficient pseudopotentials for plane-wave calculations," Phy. Rev. B. **43**, 1425(1993)

[17] L. Bosio, S. Chen, and J. Teixeira, "Isochoric temperature differential of the x-ray structure factor and structural rearrangements in low-temperature heavy water," Phys. Rev. A **27**, 1468 (1983).

[18] F. Sciortino, A. Geiger, and E. Stanley, "Isochoric differential scattering functions in liquid water: the fifth neighbor as a network defect," Phys. Rev. Lett. **65**, 3452 (1990).

[19] M. Sprik, J. Hutter, and M. Parrinello, J. Chem. Phys. **105**, 1142 (1996).

[20] J. Ortega, J. P. Lewis, and O. Sankey, "First principles simulations of fluid water: The radial distribution functions.," J. Chem. Phys. **106**, 3696 (1996).

[21] P. L. Silvestrelli and M. Parrinello, "Structural, electronic, and bonding properties of liquid water from first principles.," J. Chem. Phys. **111**, 3572 (1999).

[22] S. Izvekov and G. A. Voth, "Car–Parrinello molecular dynamics simulation of liquid water: New results.," J. Chem. Phys. **116**, 10372 (2002).

[23] J. C. Grossman, E. Schwegler, E. W. Draeger, F. Gygi, and G. Galli, "Towards an assessment of the accuracy of density functional theory for first principles simulations of water.," J. Chem. Phys. **120**, 300 (2004).

[24] M.W. Mahoney and W.L. Jorgensen, J. Chem. Phys. **112**, 8910 (2000).

[25] J. Grossman, E. Schwegler, E. Draeger, F. Gygi, and G. Galli, J. Chem. Phys. **120**, 300 (2004).

[26] E. Schwegler, J. Grossman, F. Gygi, and G. Galli, J. Chem. Phys. **121**, 5400 (2004).

[27] D. Asthagiri, L. Pratt, and J. Kress, Phys. Rev. E **68**, 41505 (2003).

[28] M. V. Fernandez-Serra and E. Artacho, J. Chem. Phys. **121**, 11136 (2004).

[29] P. Sit and N. Marzari, J. Chem. Phys. **122**, 204510 (2005).

[30] H. Lee and M. Tuckerman, J. Chem. Phys. **125**, 154507 (2006).

[31] M. Guidon, F. Schiffmann, J. Hutter, and J. VandeVondele, J. Chem. Phys. **128**, 214104 (2008).

[32] J. Schmidt, J. VandeVondele, I.-F. W. Kuo, D. Sebastiani, J. I. Siepmann, J. Hutter, and C. J. Mundy, J. Phys. Chem. B **113**, 11959 (2009).

[33] R. Mills, J. Chem. Phys. **77**, 685 (1973).

[34] A. Soper, Chem. Phys. **258**, 121 (2000).

[35] J. Sorenson, G. Hura, R. Glaeser, and T. Head-Gordon, J. Chem. Phys. **113**, 9149 (2000).

[36] M. Allesch, F. Lightstone, E. Schwegler, and G. Galli, J. Chem. Phys. **128**, 014501 (2008).

[37] M. Sharma, R. Resta, and R. Car, Phys. Rev. Lett. **95**, 187401 (2005).

[38] G. Cicero, J. Grossman, E. Schwegler, F. Gygi, and G. Galli, J. Am. Chem. Soc. **130**, 1871 (2008).

[39] J. Morrone and R. Car, Phys. Rev. Lett. **101**, 017801 (2008).

[40] B. Chen, I. Ivanov, M. Klein, and M. Parrinello, Phys. Rev. Lett. **91**, 215503 (2003).

[41] S. Habershon, T. Markland, and D. Manolopoulos, J. Chem. Phys. **131**, 024501 (2009).

[42] R. Car and M. Parrinello, Phys. Rev. Lett. **55**, 2471 (1985).

[43] J. VandeVondele, F. Mohamed, M. Krack, J. Hutter, M. Sprik, and M. Parrinello, J. Chem. Phys. **122**, 014515 (2004).

[44] M. McGrath, J. Siepmann, I. Kuo, C. Mundy, J. VandeVondele, J. Hutter, F. Mohamed, and M. Krack, J. Phys. Chem. A **110**, 640 (2006).

[45] E. Schwegler, G. Galli, and F. Gygi, Phys. Rev. Lett. **84**, 2429 (2000).

[46] A. D. Becke, Phys. Rev. A **38**, 3098 (1988).

[47] C. Lee, W. Yang, and R. Parr, Phys. Rev. B **37**, 785 (1988).

[48] J. Perdew, K. Burke, and M. Ernzerhof, Phys. Rev. Lett. **77**, 3865 (1996).

[49] S. Grimme, journal of Computational Chemistry **27**, 1787 (2006).

[50] M. Dion, H. Rydberg, E. Schröder, D. C. Langreth, and B. I. Lundqvist, Phys. Rev. Lett. **92**, 246401 (2004).

[51] W. Kohn and L. Sham, Phys. Rev. **140**, A1133 (1965).

[52] P. Hohenberg and W. Kohn, Phys. Rev. **136**, B864 (1964).

[53] B. Hammer, L. B. Hansen and J. K. Norskov, Phys. Rev. B **59**, 7413 (1999).

[54] Y. Zhang and W. Yang, Phys. Rev. Lett. **80**, 890 (1998).

[55] G. Román-Pérez and Soler J. M., Phys. Rev. Lett. **103**, 096102 (2009).

[56] N. Troullier and J. L. Martins, Phys. Rev. B **43**, 1993 (1991).

[57] L. Kleinman and D. M. Bylander, Phys. Rev. Lett. **48**, 1425 (1982).

[58] P. Ordejón, E. Artacho, and J. M. Soler, Phys. Rev. B **53**, 10441 (1996).

[59] J. M. Soler, E. Artacho, J. D. Gale, J. J. A. García, P.Ordejón, and D. Sánchez-Portal, J. Phys. Condens. Matter. **14**, 2745 (2002).

[60] J. Junquera, O. Paz, D. Sánchez-Portal, and E. Artacho, Phys. Rev. B **64**, 235111 (2001).

[61] E. Anglada, J. M. Soler, J. Junquera, and E. Artacho, Phys. Rev. B **66**, 205101 (2002).

[62] See Supplementary Material Document No. for detailed information on the two basis sets used in this study. For information on Supplementary Material, see http://www.aip.org/pubservs/epaps.html.

[63] W. Jorgensen, J. Chandrasekhar, J. Madura, and M. Klein, J. Chem. Phys. **79**, 926 (1983).

[64] H. Berendsen, D. van der Spoel, and R. van Drunen, Comput. Phys. Commun. **91**, 43 (1995).

[65] E. Lindahl, B. Hess, and D. van der Spoel, J. Mol. Model. **7**, 306 (2001).

[66] S. Nose, J. Chem. Phys. **81**, 511 (1984).

[67] W. G. Hoover, Phys. Rev. A **31**, 1695 (1985).

[68] M. Allen and D. Tildesley, *Computer Simulation of Liquids* (Oxford University Press, 1987).

[69] M. V. Fernandez-Serra, G. Ferlat, and E. Artacho, Molecular Simulation **31**, 361 (2005).

[70] T. Kuhne, M. Krack, and M. Parrinello, J. Chem. Theory. Comput. **5**, 235 (2009).

[71] B. Dunweg and K. Kremer, J. Chem. Phys. **99**, 6983 (1993).

[72] B. Dunweg and K. Kremer, J. Chem. Phys. **99**, 6983 (1993).

[73] F. Mallamace, C. Branca, M. Broccio, C. Corsaro, C. Mou, and S. Chen, Proc. Natl. Acad. Sci. **104**, 18387 (2007).

[74] D. Paschek, Phys. Rev. Lett. **94**, 217802 (2005).

[75] G. Hura, D. Russo, R. M. Glaeser, T. Head-Gordon, M. Krack, and M. Parrinello, Physical Chemistry Chemical Physics **5**, 1981 (2003).

[76] A. K. Soper, journal of Physics: Condensed Matter **19**, 335206 (2007).

[77] See Supplementary Material Document No. for a graph of the radial distribution functions as a function of the pressure. For information on Supplementary Material, see http://www.aip.org/pubservs/epaps.html.

[78] D. Ceperley and B. Alder, Phys. Rev. Lett. **45**, 566 (1980).

[79] J. Perdew, Phys. Rev. Lett. **55**, 1665 (1985).

[80] X. Wu, M. Vargas, S. Nayak, V.Lotrich, and G. Scoles, J. Chem. Phys **115**, 8748 (2001).

[81] E. Tsiper, Phys. Rev. Lett. **94**, 013204 (2005).

[82] S. Tsuzuki and H. Lüthi, J. Chem. Phys. **114**, 3949 (2001).

[83] L. I-Chun, A.P. Seitsonen, M. D. Coutinho-Neto, I Tavernelli, and U. Rothlisberger, The journal of Physical Chemistry B **113**, 1127 (2009).

[84] See Supplementary Material Document No. for the O-H and H-H radial distribution functions. For information on Supplementary Material, see http://www.aip.org/pubservs/epaps.html.

[85] N. Giovambattista, F. W. Starr, F. Sciortino, S. V. Buldyrev, and H. E. Stanley, Phys. Rev. E **65**, 041502 (2002).

[86] All the pentamer calculations in this table are performed using the full basis for the 64 molecules within the unit cell, as taken from the snapshot, and therefore are BSSE (basis set superposition error) corrected.

[87] D. C. Langreth, B. I. Lundqvist, S. D. Chakarova-Kack, V. R. Cooper, M. Dion, P. Hyldgaard, A. Kelkkanen, J. Kleis, L. Z. Kong, S. Li, et al., J. Phys.: Condens. Matter **21**, 084203 (2009).

[88] J. Klimes, D. R. Bowler, and A. Michaelides, journal of Physics : Condensed Matter **22**, 022201 (2010).

[89] K. Lee, E. Murray, L. Kong, B. Lundqvist, and D. Langreth, arXiv:1003.5255v1 (2010).

[90] I. M. Svishchev and P. G. Kusalik, J. Chem. Phys. **99**, 3049 (1993).

[91] A. Soper and M. Ricci, Phy. Rev. Lett. **84**, 2881 (2000).

[92] A.Luzar, J. Chem. Phys. **113**, 10663 (2000).

[93] See Supplementary Material Document No. for the RDF decomposition calculated for revPBE and DRSLL. For information on Supplementary Material, see http://www.aip.org/pubservs/epaps.html.

[94] Xiao Shen, Philip B. Allen, Mark S. Hybertsen and James T. Muckerman, "Water Adsorption on the GaN (10$\underline{1}$0) Nonpolar Surface.," J. Phys. Chem. C **113**, 3365 (2009).

[95] Xiao Shen, Yolanda A. Small, Jue Wang, Philip B. Allen, Maria V. Fernandez-Serra, Mark S. Hybertsen and James T. Muckerman, "Photocatalytic Water Oxidation at the GaN (10$\underline{1}$0)-Water Interface.," J. Phys. Chem. C **114**, 13695 (2010).

[96] Jue Wang, G. Roman-Perez, Jose M. Soler, Emilio Artacho and M.-V. Fernandez-Serra, "Density, structure, and dynamics of water: The effect of van der Waals interactions.," J. Chem. Phys. **134**, 024516 (2011).

[97] K. Maeda, K. Teramura, D. Lu, T. Takata, N. Saito, Y. Inoue, and K. Domen, Nature **440**, 295 (2006).

[98] K. Maeda, K. Teramura, N. Saito, N. Saito, Y. Inoue, and K. Domen, Bull. Chem. Soc. Jpn **80**, 1004 (2007).

[99] V. Fiorentini, M. Methfessel, and M. Scheffler, Phy. Rev. B **47**, 13353 (1993).

[100] O. A. V. Lilienfeld and P. A. Schultz, Phy. Rev. B **77**, 115202 (2008).

[101] M. Allen and D. Tildesley, *Computer Simulation of Liquids* (Oxford University Press, 1987).

[102] M. Mahoney and W. Jorgensen, J. Chem. Phys. **112**, 8910 (2000).

[103] D. Marx, M. E. Tuckerman, J. Hutter, and M. Parrinello, Nature **397**, 601 (1999).

[104] S. Y. Venyaminov and F. G. Predergast, Analytical Biochemistry **248**, 234 (1997).

[105] D. S. Eisenberg and W. Kauzmann, *The structure and Properties of Water* (Clarendon, Oxford, 1969).

[106] M. Sharma, R. Resta, and R. Car, Phys. Rev. Lett. **95**, 187401 (2005).

[107] M. Leszczynski, T. Suski, H. Teisseyre, P. Perlin, I. Grzegory, J. Jun, S. Porowski, and T. D. Moustakas, "Thermal expansion of gallium nitride," J. Appl. Phys. **76**, 4909 (1994).

[108] J. Northrup and E. Neugebauer, J. Phys. ReV. B **53**, R10477 (1996).

[109] Noam Agmon, "The Grotthuss mechanism". Chem. Phys. Lett. **244**, 456462 (1995).

[110] B. Meyer, H. Rabaa and D. Marx, Phys. Chem. Chem. Phys., **8**, 1513 (2006).

[111] Li Li, James T. Muckerman, Mark S. Hybertsen, and Philip B. Allen, Phys. Rev. B, **83**, 134202 (2011).

[112] Wei-Qiang Han, Zhenxian Liu, and Hua-Gen Yu, Appl. Phys. Lett., **96**, 183112 (2010).

[113] Kazuhiko Maeda and Kazunari Domen, "Photocatalytic Water Splitting: Recent Progress and Future Challenges," J. Phys. Chem. Lett., **1 (18)**, 2655(2010).

[114] K. Leung, Ida M. B. Nielsen, and Louise J. Criscenti "Elucidating the Bimodal Acid-Base Behavior of the Water–Silica Interface from First Principles," J. Am. Chem. Soc., **1 (131)**, 18358(2009).